Nanolaminate TRIP-TWIP martensitic matrix steels: Design and characterization

Von der Fakultät für Georessourcen und Materialtechnik
der Rheinisch-Westfälischen Technischen Hochschule Aachen

zur Erlangung des akademischen Grades eines
Doktors der Ingenieurwissenschaften

genehmigte Dissertation
vorgelegt von **M.Sc.**

Meimei Wang

aus Shandong, China

Berichter: Professor Dr.-Ing. Dierk Raabe
Univ.-Prof. Dr.-Ing. Wolfgang Bleck

Tag der mündlichen Prüfung: 09. Dezember 2015

Contents

Chapter 1 Introduction

Martensite, as one of the most well-known yet least understood type of microstructure occurring in modern advanced steels, profoundly suffers from its inherent brittleness. Cracks in martensitic steels, once initiated, can propagate easily along martensitic boundaries due to their small mutual misorientation, leading to premature failure of the microstructure [1]. Different approaches have been explored in past decades to improve the ductility and toughness of martensite, including optimizing prior austenite state in terms of chemical composition [1]–[3] and grain size [4], [5], tempering [6], [7], and applying multilayer approach [8]–[11], etc.

This thesis pursues the aim to enhance higher toughness and ductility of this type of martensitic microstructure via introducing nanolaminate microstructures consisting of alternating layers of martensite and austenite. To introduce retained or reverted austenite, two routes are plausible, either starting from the austenite to produce a microstructure consisting of martensite (or supersaturated ferrite) and retained austenite, or starting from the martensite state and partially revert martensite to austenite during annealing.

Two examples following the former route are quenching and partitioning steels (QP steels) and carbide-free bainite steels (CFB steels). QP steels are obtained by quenching from single austenite region or two phase region (austenite and ferrite) to quenching temperature, and subsequent partitioning of carbon at partitioning temperature [12], [13]. Quenching temperature is between martensite start temperature M_s and martensite finish temperature M_f, and thus determines the volume fraction of martensite and austenite. Partitioning temperature is usually higher than quenching temperature. The partitioning process is described by Speer et al. [12] as constraint paraequilibrium process, where only partitioning of carbon between martensite and

retained austenite occurs and the phase interface does not migrate during the partitioning process. Thus, the final carbon content of retained austenite, e.g. the austenite stability, is determined by the volume fraction of martensite and the partitioning process [13]. CFB steels, on the other hand, are obtained by quenching from austenite state to bainitic holding temperature. During isothermal holding process, partition of carbon from supersaturated ferrite to retained austenite takes place and interface migrates simultaneously, as described by paraequilibrium process [14]. In both cases, the partitioning of carbon into austenite can further stabilize austenite after quenching to room temperature.

The latter route, as explained by Raabe et al. [15], involves elemental segregation to boundaries and subsequential phase transformation of decorated boundaries to austenite, as described by local equilibrium occurring at a temperature much lower than the bulk transformation temperature. As a generic rule of alloy design, the selection of solutes should fulfill the following criteria: (i) these solutes should have high tendency to segregate at grain boundaries in a given matrix in order to form large concentration gradients; (ii) their segregation should lower the phase transformation temperature from martensite to austenite (e.g. Mn, Ni, C, N, Co, etc.); and (iii) these solutes should choose to segregate to interfaces rather than forming a third phase inside the matrix [15]. In addition to the high equilibrium segregation of these solutes, two additional components contribute to a low nucleation barrier along lath martensite boundaries or dislocations: (i) the low interface energy due to the Kurdjumov-Sachs (K-S) orientation relationship between martensite and reverted austenite; (ii) the high gain in elastic energy density associated with martensite to austenite transformation therein [15]. Thus, with properly selected alloy elements segregated to lath martensite boundaries, austenite can be formed along these decorated lath martensite boundaries, promoting the formation of nanolaminate martensite-reverted austenite microstructure.

In this work, this latter route, i.e. starting from martensite, is adopted to introduce reverted austenite layers into martensite. During the reversion treatment, the matrix martensite itself is inevitably tempered and loses its high strength due to the large extent of dislocation annihilation. Thus, to partially compensate the strength loss, complementary hardening mechanism in martensite is desired. With proper alloy design concept, one hardening mechanism that can emerge simultaneously during tempering of martensite is precipitation hardening (maraging). In case of coherent interface between martensite and particles, particles can homogeneously nucleate within the martensite matrix, which in turn also restrict the extent of dislocation annihilations in martensite [16]. Thus, matrix martensite can preserve its high dislocation density, and benefits from precipitation hardening effects arising from (i) Kelly-Fine mechanism (for small precipitates) [17]; or (ii) Orowan mechanism (for large precipitates) [18].

In this work, the goal is to improve the toughness and ductility of martensitic steels with preserved strength via introducing reverted austenite and particles. More specifically, this work pursues the aim to trigger austenite reversion and maraging simultaneously via a single heat treatment in martensitic steels, e.g. modifying martensitic steels to TRIP-maraging steels. With proper alloy design concept and thermomechanical treatment, TRIP-maraging steels are expected to benefit from three aspects simultaneously, i.e. the TRIP effect (from reverted austenite), the maraging effect (from the precipitates in martensite) and the classical composite effect (from the morphology of the microstructure). In majority of related works in medium-Mn steels with reverted austenite, the enhanced mechanical properties are mainly attributed to austenite volume fraction and its transformation kinetics, e.g. active TRIP effect throughout the entire deformation process [19]–[21]. While TRIP effect does contribute to the enhancement of mechanical property, the reasoning of ductilizing is not solely ascribed to it. As already underlined by some reports, the collaborative deformation behaviors of microstructure constituents, including the deformation

within microstructure constituents, their interplay with each other and the damage resistance of the microstructure, etc., are believed to also play important roles in controlling ductility [22]–[25]. Thus, the exact nature of the aging induced improvements is not fully understood, yet remains as important for optimizing microstructure and mechanical properties. In this regard, improper chemical composition or an unfavorable thermo-mechanical treatment may lead to introduction of additional damage mechanisms (e.g. due to the strain incompatibility of hard (martensite) and soft (austenite) phase introduced) or ineffective TRIP contribution (e.g. austenite already transformed early in deformation and absent when needed for damage resistance at high-strain levels). Thus, this work aims to provide generalized alloy design guidelines for martensitic-matrix steels with a detailed understanding of the deformation and damage mechanisms. The provided damage mechanism is also beneficial for resistance against hydrogen embrittlement (HE), which is another problem encountering high strength martensitic steels [26], [27]. In addition, reverted austenite and precipitates in martensite can also act as trapping sites for diffusible hydrogen, e.g. responsible for causing HE [28], [29], hence promoting the TRIP-maraging strategy as promising remedy for aiding martensitic steels from HE [30]–[32]. To optimize microstructure for even enhanced mechanical properties, non-autonomic healing concept and cold rolling approach are proposed and validated.

The framework of this thesis is described as follows.

Chapter 1: Introduction.

Chapter 2: Processing and methodologies. In this chapter, the alloy design concept, the metallurgical and the thermo-mechanical processes to produce TRIP-maraging steels, the novel multi-probe methodologies including microstructure characterization and mechanical testing are described in detail.

Chapter 3: Microstructure design and experimental validation. In this chapter, following the guidance of Thermo-Calc and Dictra calculations using thermodynamic database TCFE7 and mobility database MOBFe2, the reversion treatment are carried out and the resultant microstructures are experimentally validated.

Chapter 4: Mechanical properties, deformation and damage micro-mechanisms. In this chapter, the mechanical properties of the designed TRIP-maraging steels are examined. Then the deformation and damage micro-mechanisms are investigated and discussed with respect to the mechanical properties. In the end, a generalized guideline for alloy design is proposed. **The main content of Chapter 4 is based on [33] M.-M. Wang, C. C. Tasan, D. Ponge, A.-C. Dippel, and D. Raabe, "Nanolaminate transformation-induced plasticity–twinning-induced plasticity steel with dynamic strain partitioning and enhanced damage resistance," Acta Mater., vol. 85, pp. 216–228, Feb. 2015.**

Chapter 5: Enhancing resistance of lath martensite to hydrogen embrittlement by introducing nano-films of interlath austenite. In this chapter, the concept of using TRIP-maraging steel as a remedy for aiding martensitic steels from HE is examined. **The main content of Chapter 5 is based on [34] M.-M. Wang, C. Tasan, M. Koyama, D. Ponge, and D. Raabe, "Enhancing hydrogen embrittlement resistance of lath martensite by introducing nano-Films of interlath austenite," Metall. Mater. Trans. A, pp. 0–5, 2015.**

Chapter 6: Restorations of microstructure and mechanical properties via cyclic austenite reversion. In this chapter, the criteria for designing non-autonomic healable steels are proposed. Then the criteria are validated in the current TRIP-maraging steels.

Chapter 7: Smaller is less stable: Size effects on twinning vs. transformation of reverted austenite in TRIP-maraging steels. This chapter is a case study for studying size effect on austenite stability. The underlying reasoning for the observed surprising 'smaller is less stable' effect is systematically investigated and discussed. **The main content of Chapter 7 is based on [35] M.-M. Wang, C. C. Tasan, D. Ponge, A. Kostka, and D. Raabe, "Smaller is less stable: Size effects on twinning vs. transformation of reverted austenite in TRIP-maraging steels," Acta Mater., vol. 79, pp. 268–281, Oct. 2014.**

Chapter 8: Further microstructure and mechanical property optimizations via cold rolling of as-quenched martensite. In this chapter, the microstructure is further optimized for enhanced mechanical properties by modifying the starting martensitic microstructure by cold rolling.

Chapter 9: Conclusions and outlook.

Chapter 2 Processing and Methodologies

In order to stimulate austenite reversion and precipitation in martensite upon modest annealing, a medium-Mn steel with a nominal chemical composition of Fe-9Mn-3Ni-1.4Al-0.01C (mass %) is designed for this work. Mn is chosen over C to thermodynamically stabilize reverted austenite in order to design an initially ductile martensite, e.g. with low C content, and avoid welding problem initiated from C [36], [37]. Based on this effect, it is possible to fine-tune the TRIP effect during the following deformation [23], [38]–[44]. Ni is added to form nano-precipitates together with Al and Mn inside the martensite matrix phase, creating the maraging effect [45]–[48].

The steel ingot was cast in a vacuum induction furnace, solution treated and hot rolled at 1100 °C to thickness of ~5 mm. The real chemical composition of the medium-Mn steel is Fe-8.96Mn-3.03Ni-1.40Al-0.01C (mass %). Due to the negligible difference between nominal and real chemical composition, all compositions in the following will be referred to as nominal chemical composition, unless specially pointed out. Afterwards, the steel plate was homogenized at 1100 °C for 1 h and water quenched to ambient temperature. Then steel plate with microstructure of as-quenched martensite was obtained. To induce partial reversion of as-quenched martensite to austenite, steel plates were further annealed at 600 °C for different periods (1 h, 4 h or 8 h) and subsequently quenched in water [47], [49], [50]. For the purpose of microstructure optimization, the structure of martensite was modified by cold rolling the as-quenched martensite plate to ~1.5 mm (~70% thickness reduction). Partial reversion of cold-rolled martensite was also carried out at 600 °C, but only for shorter time (10 min, 30 min or 1 h). The selection of reversion conditions is based on Thermo-Calc and Dictra calculations using thermodynamic database TCFE7 and mobility database MOBFe2 [51]. Combined with the thermodynamic database package, Thermo-Calc software can formulate the Gibbs energy and second derivative of Gibbs energy of a

multicomponent system based on equations of state, and thermodynamic functions of both pure substances and solution phases [52]. Then Thermo-Calc software can perform equilibrium calculations based on Gibbs energy minimization methods. Thermo-Calc software is capable of all kinds of thermodynamic calculations, e.g. phase equilibrium, phase transformation temperature, driving force, etc., for varied advanced materials in multi-component system over a temperature-pressure-composition ranges [52], [53]. Dictra software uses Thermo-Calc for thermodynamic calculations but further extends to the engaged kinetic problems by solving diffusion equations, using a complete concentration-temperature diffusivity matrix. The diffusivity matrix is calculated from parameters stored in the mobility database. Dictra software is able to simulate kinetics of diffusion-controlled phase transformations in multi-component metallic systems [52], [53]. Therefore, the equilibrium and kinetics of austenite reversion processes during annealing of as-quenched martensite were first calculated by Thermo-Calc and Dictra software.

To examine the influences of reverted austenite on the mechanical properties of martensite under both quasi-static and dynamic loading conditions, two kinds of mechanical tests were carried out, namely uniaxial tensile tests and impact tests. Uniaxial tensile tests were conducted at ambient temperature with an initial strain rate of 10^{-3} s^{-1}. Impact tests covered over a temperature range of -150 °C to 100 °C were also carried out. For the tensile tests, a Kammrath & Weiss stage was used, and the strain was measured by digital image correlation (DIC) using Aramis software (GOM GmbH) [54]. DIC is a full-field image analysis method based on grey value digital images, e.g. digital images of the surface pattern on a tensile specimen captured during tensile test, and can determine the displacement of an object, e.g. particles on the pattern, under load in three dimensions. Then, by applying a correlation algorithm, the local strain distributions along gauge length of the tensile specimens can be obtained [55]. Afterwards, it is possible to investigate the

microstructure evolutions at different local strain values and gain a better understanding of its correlation with the overall mechanical properties. The impact tests were performed on subsize Charpy V-notched samples with dimensions of 3*4*27 mm^3 and with a 60° V-notch in the sample center according to the standard DIN 50 115. The samples were machined with the longitudinal direction along the rolling direction and the 60° V-notch perpendicular to the rolling plane. In addition, *in-situ* SEM tensile and 3-point bending tests were performed.

Due to the complexity and the small length scales of the related microstructures, a further improvement in the understanding also requires application of multiple experimental methodologies. The two most commonly employed techniques, namely X-ray diffraction (XRD) and transmission electron microscopy (TEM), even when used *in-situ* during deformation, provide either good statistics, but no direct microstructural observation capacity (former), or direct microstructural observation capacity, but with limited statistics (latter). High resolution electron backscatter diffraction (HR-EBSD) is a scanning electron microscopy (SEM) based microstructural-crystallographic technique to measure the crystallographic orientation. Due to the small electron beam diameter achieved from a field emission gun (FEG), the spatial resolution can be brought down to as small as 10nm, depending on operation conditions and sample, etc. Thus, when combined with *in-situ* tensile testing, the recently emerging HR-EBSD mapping technique provides an excellent combination of direct and statistical observation of transformation mechanisms with satisfactory spatial resolution [56]. The *in-situ* data are accompanied by corresponding *post-mortem* analysis conducted with SEM based EBSD, electron channeling contrast imaging (ECCI), and secondary electron (SE) imaging methods, as well as transmission electron microscopy (TEM) and synchrotron X-ray diffraction (SXRD) analysis. ECCI is a powerful technique in SEM for observing crystal defects, e.g. dislocations, stacking faults (SFs), etc. [57]. Based on the crystallographic orientations obtained in EBSD and the

simulated channelling patterns, the crystals can be adjusted such that two-beam diffraction conditions are achieved and strong electron channelling contrast can be obtained to image crystal defects [57]. Under the current operation conditions in Zeiss-Crossbeam XB 1540 FIB-SEM and Zeiss-Merlin SEM, e.g. acceleration voltage of 30 KV, working distance of 7 mm and with a 120 μm aperture in high beam current mode, a resolution of 2.9 nm is achieved. Since it is operated within SEM, ECCI is capable of providing fast and large-field-of-view observations of defect structures within microstructure constituents, and hence, is employed in this work. For the SEM analysis JEOL JSM-6500F (for *in-situ* and *post-mortem* EBSD), Zeiss-Crossbeam XB 1540 FIB-SEM (for *in-situ* ECCI and SE) and Zeiss-Merlin (for *post-mortem* ECCI) were employed. In order to simultaneously resolve crystal defects with higher resolution, analyze crystal structures with electron diffraction patterns and measure elemental distribution by energy dispersive X-ray spectroscopy (EDX), TEM analysis were also carried out. TEM observations were performed in a JEOL JEM-2200FS operated at 200kV.

For SEM investigations, samples were prepared by grinding, polishing in diamond suspension and final polishing in colloidal silica suspension. The last preparation step ensures a deformation-free surface. HR-EBSD measurements were carried out using a JEOL JSM-6500F microscope. The patterns were recorded with a high-speed CCD camera and the results were analyzed by the TSL-OIM software. The samples were 70° tilted with respect to the incident electron beam. Measurements were carried out at 15 kV with a step size of 80 nm. In relevant regions, EDX measurements were also carried out to investigate the elemental distributions of the microstructure. For *in-situ* EBSD measurements, the same area on tensile sample surface was measured after each deformation step. In the case of *post-mortem* EBSD measurements, samples deformed to different strain levels were re-prepared following conventional sample preparation procedures and then probed by EBSD, i.e. probed from bulk. Specimens for TEM analysis were

prepared from tensile samples deformed to different strain values. The discs with diameter of 3 mm were mechanically ground to ~100 μm thickness and then thinned using double-jet electro polishing system Tenupol 5 (electrolyte: 10% perchloric acid and 90% methanol; temperature -32 °C and a voltage of 16 V).

Synchrotron X-ray diffraction (SXRD) was also applied in this work. The SXRD measurements were carried out at the high resolution powder diffraction beamline P02.1 at PETRA III (DESY Hamburg, Germany) using a wavelength of λ=0.20727 Å. The dimension of the incident beam was 200×200 μm^2. After penetrating through a ~1 mm thick tensile sample, the generated two-dimensional XRD patterns were collected using a fast image plate detector Perkin Elmer 1621 (2048×2048 pixels, 200×200 μm^2 pixel size, intensity resolution of 16 bit), which was placed at a distance of 800 mm away from the sample. XRD patterns were integrated into the 2θ-space using the software FIT2D [58], and then analyzed by the Rietveld method in MAUD [59].

Chapter 3 Microstructure design and experimental validation

To select the proper reversion treatment conditions, the thermodynamics and kinetics of austenite reversion processes in Fe-9Mn-3Ni-1.4Al-0.01C (mass %) were calculated by Thermo-Calc and Dictra software using thermodynamic database TCFE7 and mobility database MOBFE2. Since martensite is not equilibrium phase but possess similar thermodynamic parameters as ferrite, martensite is thermodynamically treated as ferrite. The kinetic parameters of martensite, however, are expected to deviate from ferrite, due to its higher content of dislocations and other crystal defects. Thus, martensite is thermodynamically treated as ferrite but with modified diffusivity here [47]. Nano-precipitates were not included in the calculation due to lack of thermodynamic data in the database. Since the aim of Thermo-Calc and Dictra calculations lies in providing a guide for the reversion treatment, these influences are expected to be trivial. Based on Thermo-Calc and Dictra calculations, two criteria were used as guidelines: (i) to maintain high strength, martensite should be kept as major phase, i.e. with volume fraction higher than 50%; (ii) austenite should possess a high volume fraction and considerable stability to assure significant benefits from the TRIP effect.

The equilibrium phase fraction and chemical composition of austenite as a function of annealing temperature are calculated by Thermo-Calc software using TCFE7 database, as shown in Figure 3.1 and Figure 3.2, respectively. With increasing annealing temperature, the equilibrium fraction of austenite continues to increase (Figure 3.1), but the concentrations of austenite stabilizing elements, e.g. Mn and Ni, simultaneously decrease in austenite (Figure 3.2). When the thermal stability decreases to a certain level, unstable reverted austenite is expected to transform to martensite during quenching, i.e. athermal martensite will be developed during quenching.

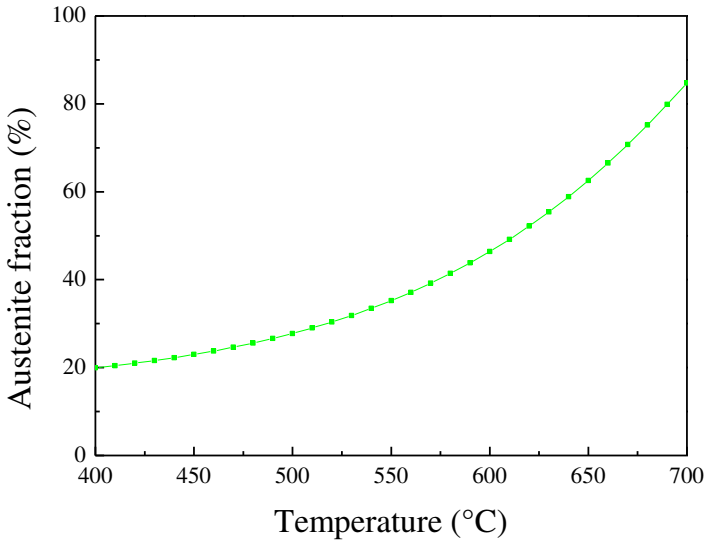

Figure 3.1: Predicted equilibrium austenite fraction as a function of annealing temperature. Calculation performed using Thermo-Calc with thermodynamic database TCFE7.

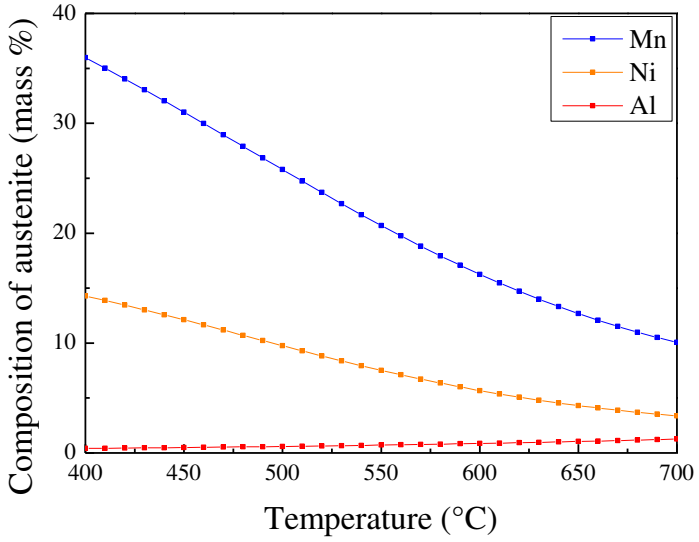

Figure 3.2: Predicted chemical composition of reverted austenite as a function of temperature. Calculation performed using Thermo-Calc with thermodynamic database TCFE7.

The fraction of athermal martensite formed during quenching is predicted by the model proposed by De Moor et al. [44], which is based on the Koistinen and Marburger equation [60]:

$$f_{\alpha'} = 1 - \exp\left[-0.011 \times (M_s - T)\right] \quad (1)$$

Where, $f_{\alpha'}$ is the fraction of athermal martensite formed upon quenching; M_s is martensite start temperature and T is the lowest temperature reached upon quenching.

The M_s is estimated by the empirical equation proposed by Andrews [61]:

$$M_s = 539 - 432x_C - 30.4x_{Mn} - 17.7x_{Ni} - 12.1x_{Cr} + 30x_{Al} \quad (2)$$

Where, $x_i (i = C, Mn, Ni, Cr, Al)$ is content of each alloy element is in mass percent.

Based on the equilibrium chemical composition of reverted austenite calculated by Thermo-Calc, the corresponding M_s (in equation (2)) of austenite formed at each annealing temperature was obtained. Then by substituting M_s in equation (1), the fraction of reverted austenite at ambient temperature can be predicted (Figure 3.3).

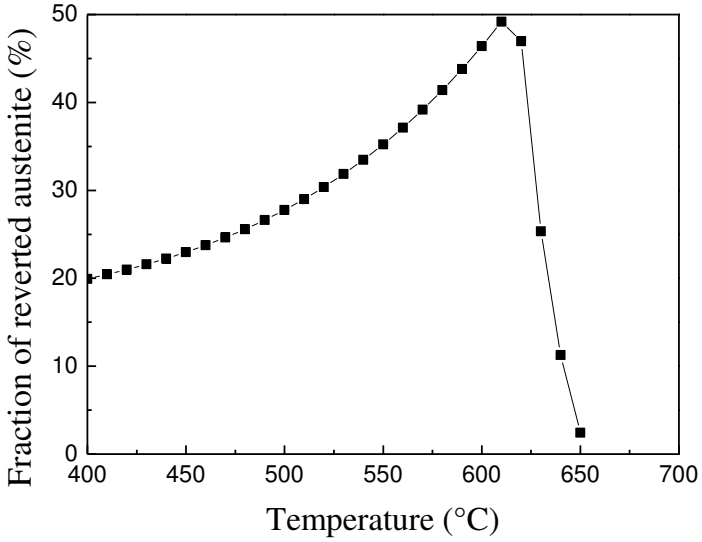

Figure 3.3: Reverted austenite fraction as a function of temperature, as predicted by the model developed by De Moor [44].

The predicted fraction of reverted austenite as a function of temperature exhibits a maximum at 610 °C (~49% phase fraction). As suggested by Lee et al. [19] in medium-Mn steels, the optimal annealing temperature should be slightly lower than the temperature with maximum austenite content (T_m), to avoid the formation of athermal martensite in the microstructure. Thus, to satisfy the two criteria proposed at the beginning of Chapter 3, i.e. keep the martensite fraction higher than 50% and guarantee sufficient thermal stability for reverted austenite during quenching, the annealing temperature to introduce reverted austenite should be lower than 610 °C.

Then the growth kinetics of reverted austenite from as-quenched martensite is calculated by Dictra software with thermodynamic database TCFE7 and mobility database MOBFE2 for three selected annealing temperature below T_m (610 °C), e.g. 550 °C, 575 °C and 600 °C. A 2 μm cell size martensite phase (α' martensite) is used as the starting microstructure. As boundary condition an initially inactive austenite layer (γ) with a planar interface was attached to the left side of martensite. An "inactive phase" does not participate in the simulation until it becomes stable. As the starting microstructure is single martensite phase and austenite will be formed as a new phase during reversion, it is treated here initially as inactive phase. For each temperature, the reversion was calculated up to 100000s. The positions of γ/α' martensite interface for these three annealing temperature as a function of time are exhibited in Figure 3.4. Comparing with 550 °C and 575 °C, reverted austenite grows considerably faster at 600 °C, e.g. by comparing the position of phase interface after the same annealing time (Figure 3.4).

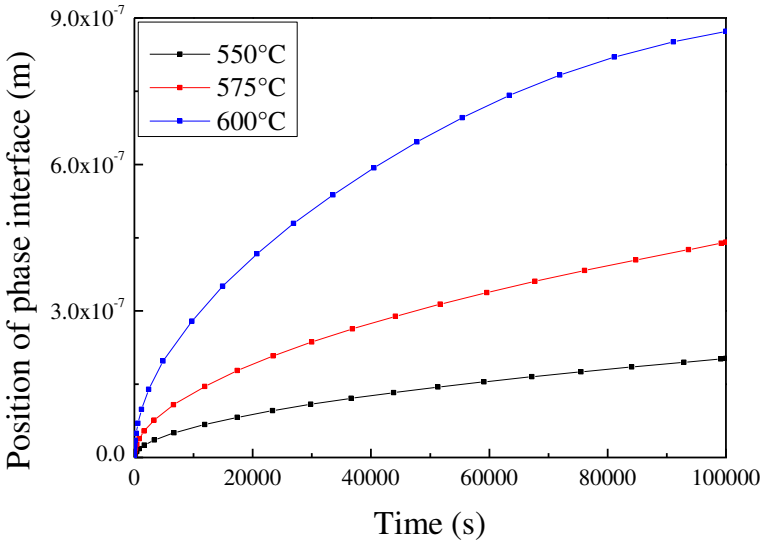

Figure 3.4: Evolution of position of γ/α' martensite interface with time during annealing at 550 °C, 575 °C and 600 °C, as calculated by Dictra software with thermodynamic database TCFE7 and mobility database MOBFE2.

Base on the overall considerations of phase fraction requirement, thermal stability and growth kinetics of γ, 600 °C is selected as the annealing temperature in this work to introduce γ to α' martensite. Eventually, two annealing time, i.e. 1 h and 8 h at 600 °C, are chosen to partially revert as-quenched α' martensite to γ. As-quenched α' martensite and after annealing at 600 °C for 1 h or 8 h, are referred to as S_{aq}, S_{1h} and S_{8h}, respectively.

Then the predicted microstructures are experimentally validated. The microstructures are revealed by SE imaging, EBSD phase map and inverse pole figure (IPF) map (Figure 3.5). Prior to reversion treatment, the microstructure consists of single α' martensite phase, as shown by the SE imaging of the etched sample surface (Figure 3.5a_1) and confirmed by the EBSD phase map (Figure 3.5a_2). No retained γ is detected within the resolution limit of the high resolution EBSD measurements carried out here, i.e. with a step size of 80 nm (Figure 3.5a_2). The EBSD IPF map demonstrates that the α' martensite laths within one martensite block exhibit nearly the same crystallographic orientation (within 1°) (Figure 3.5a_3).

After 1 h annealing at 600 °C, a new phase with thin film morphology is formed inside the α' martensite matrix (Figure 3.5b_1) and it is indexed as austenite phase (γ) by EBSD (Figure 3.5b_2). All the nano-films of reverted γ grains (γ_{RN}) inside one α' martensite block again have similar crystallographic orientations (within 1°) (Figure 3.5b_3).

With further annealing to 8 h at 600 °C, γ_{RN} grains grow further into the α' martensite matrix (Figure 3.5c_1-c_3), causing the formation of a duplex phase nano-laminate morphology α' martensite-γ_{RN} microstructure. In addition, a small amount of ε martensite phase (less than 4 vol. %) is also observed in the microstructure after the reversion treatment.

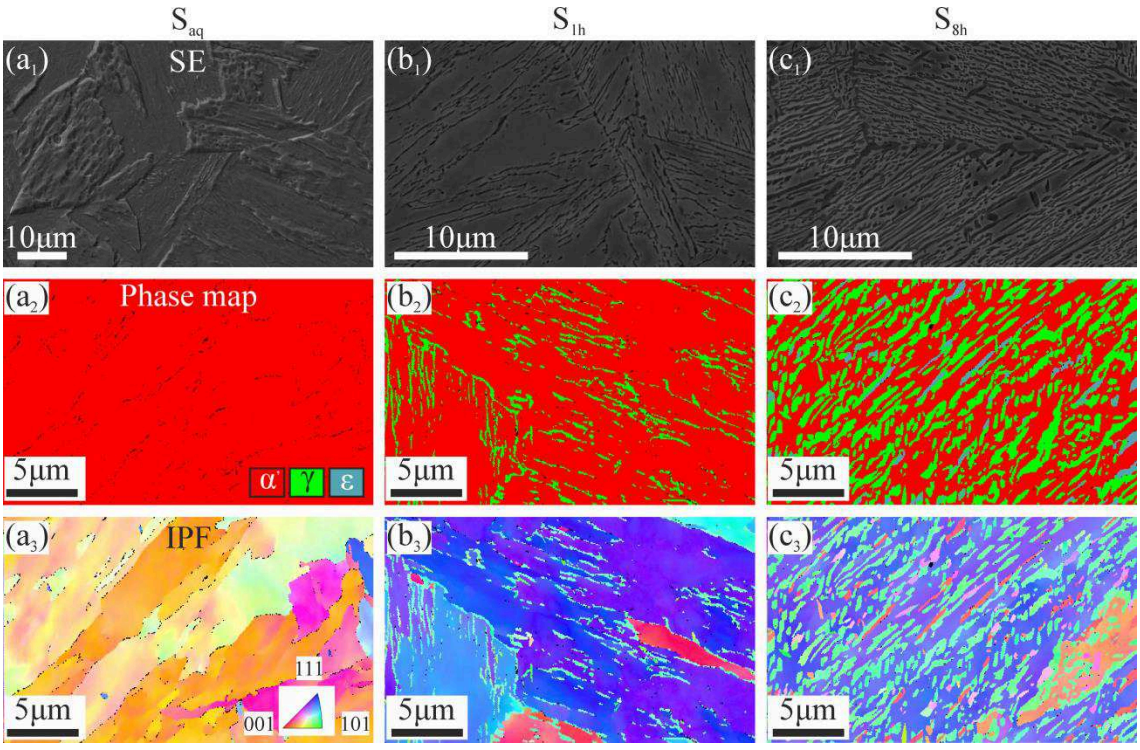

Figure 3.5: Aging induced microstructure evolution from (a) S_{aq} to (b) S_{1h} to (c) S_{8h} shown by SE imaging (1), EBSD phase map (2) and inverse pole figure (IPF) map (3). S_{aq}: as-quenched sample; S_{1h}: 1-hour heat treated sample; S_{8h}: the 8-hour heat treated sample. Source: Image from [33], Courtesy of Elsevier.

The microstructure of the 8 h heat treated sample S_{8h} are characterized by a low magnification EBSD phase map in Figure 3.6a. The detailed structures of each phase are further analyzed by TEM in Figure 3.6b-d. The STEM image (Figure 3.6b) provides a higher resolution image of the duplex phase nano-laminate morphology microstructure, where γ_{RN} grains are finely distributed in the α' martensite matrix. Details of the α' martensite and γ_{RN} phases are further revealed by high magnification STEM images in Figure 3.6c and Figure 3.6d, as highlighted by the red and green rectangles, respectively. The α' martensite matrix is characterized by finely dispersed nano-precipitates and a high density of dislocations (Figure 3.6c). The γ_{RN} grains, in contrast, do not contain particles and dislocations. The chemical compositions of α' martensite matrix and γ_{RN} grain are measured by EDX in TEM, as shown by inset in Figure 3.6d. Compared to the initially uniform elemental distributions in the as-quenched martensite (sample S_{aq}), the reversion process at 600 °C leads to partitioning of Mn and Ni into the γ_{RN} grains, and simultaneous partitioning of Al and Fe into the α' martensite matrix in the 8 h annealed sample S_{8h}.

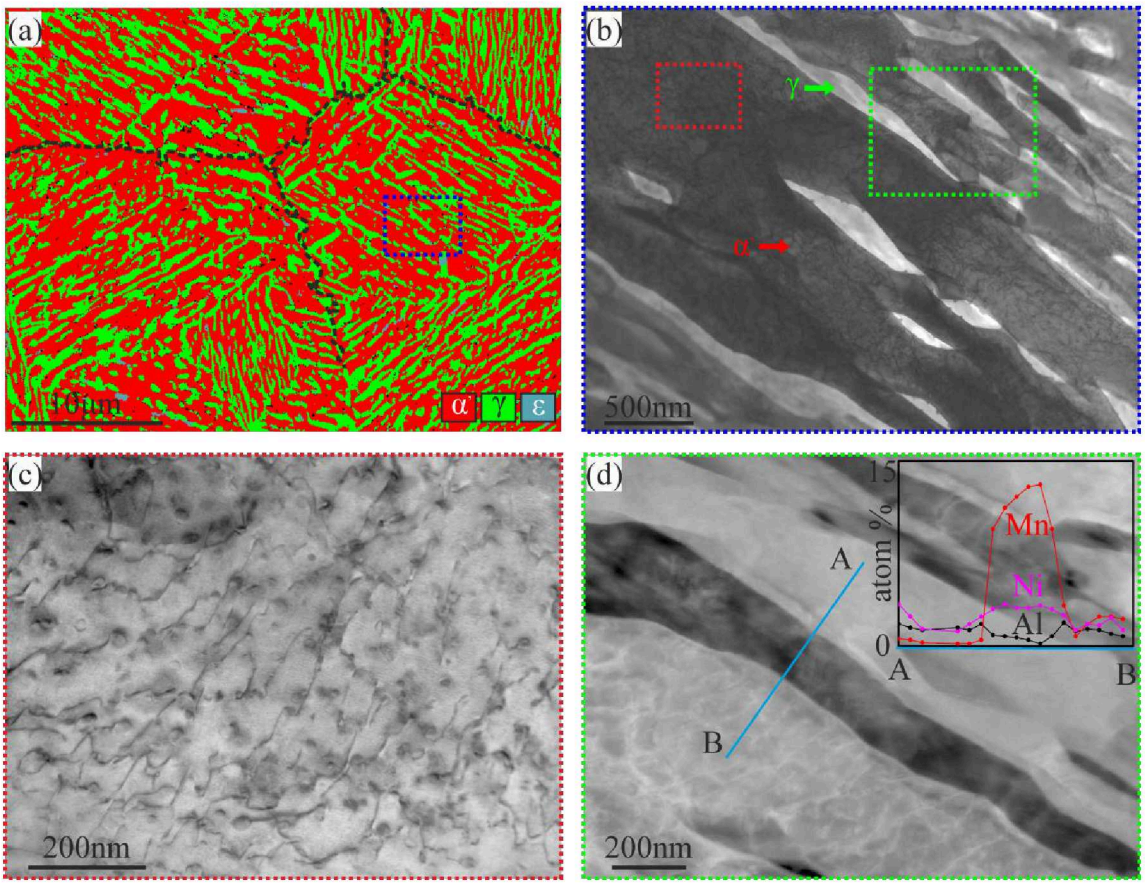

Figure 3.6: Microstructure characterization of S_{8h}: (a) EBSD phase map; (b) STEM bright field image; (c) high magnification micrograph showing nano-precipitates and high density dislocations in α' martensite; and (d) high magnification micrograph of the γ_{RN}. The three rectangles only serve to indicate the scale transition, and do not represent the exact area from which the higher magnification image has been obtained. Prior austenite grain boundaries are indicated by black dashed line in Figure 3.6a. Chemical composition of α' martensite matrix and γ_{RN} grain along the blue line A-B are shown as inset in Figure 3.6d. S_{8h}: the 8-hour heat treated sample. Source: Image from [33], Courtesy of Elsevier.

Chapter 4 Mechanical properties, deformation and damage micro-mechanisms of the nano-laminate microstructure [1]

4.1 Influence of aging on the mechanical properties

The influence of γ_{RN} on the mechanical properties of martensitic steels is examined by uniaxial tensile tests at ambient temperature and Charpy impact tests over a temperature range from -150 °C to 100 °C for martensite samples S_{aq}, and martensite-reverted austenite samplesS_{1h} and S_{8h} (Figure 4.1). The engineering stress strain curves are presented in Figure 4.1a. It is clear that after 600 °C reversion treatment, the formation of γ_{RN} phase in α' martensite leads to a pronounced improvement in uniform elongation, namely, from 2.4% for sample S_{aq} to 9.9% for sample S_{1h}, and further to 17.1% for sample S_{8h}. The improvement in ductility is not achieved at the expense of losing strength, e.g., the ultimate tensile strength (UTS) decreases from 925 MPa only to 920 MPa and then to 900 MPa. The decrease in UTS only corresponds to less than 0.6% decrease from sample S_{aq} to sample S_{1h}, and less than 2.8% decrease from sample S_{aq} to sample S_{8h}.

The local strain distributions along gauge section of tensile sample S_{aq}, S_{1h} and S_{8h}, based on DIC measurements, are plotted in Figure 4.1b. In these plots, the corresponding strain distributions of two stages, namely the stage when strain localization occurs and the final stage before fracture takes place, as shown by dashed lines and solid lines, respectively. Comparing the strain profiles of the three samples at the stage of strain localization, it is clear that the introduction of γ_{RN} into α' martensite matrix leads to a delay of onset of strain localization. The comparison of the strain

[1] The main content of Chapter 4 is based on [33] M.-M. Wang, C. C. Tasan, D. Ponge, A.-C. Dippel, and D. Raabe, "Nanolaminate transformation-induced plasticity–twinning-induced plasticity steel with dynamic strain partitioning and enhanced damage resistance," Acta Mater., vol. 85, pp. 216–228, Feb. 2015.

profiles between the stage of strain localization and the stage prior to fracture reveals the local strain accumulation during the post-necking deformation process. Apparently, in addition to the increase in uniform elongation, the presence of γ_{RN} also causes an increase in post-necking elongation, corresponding to ~30% increase from sample S_{aq} to sample S_{1h}, and 41% from sample S_{aq} to sample S_{8h}.

Besides uniaxial tensile tests, the toughness of the three materials was also assessed by impact tests (Figure 4.1c). Compared to martensite sample S_{aq}, both reversion-treated samples S_{1h} and S_{8h} exhibit enhanced toughness properties, e.g. the upper shelf energy value is increased and the ductile-to-brittle transition temperature (DBTT) is decreased (i.e. from 9 °C in S_{aq} to -49 °C in S_{1h} to -76 °C in S_{8h}, respectively). Here DBTT is defined as the temperature corresponding to half of the upper shelf energy in the impact test.

The overall mechanical properties are summarized in Figure 4.1d. It can be concluded that the introduction of the γ_{RN} grains into the α' martensite successfully leads to a consistent improvement in both ductility and toughness, with only trivial decrease in yield stress or UTS.

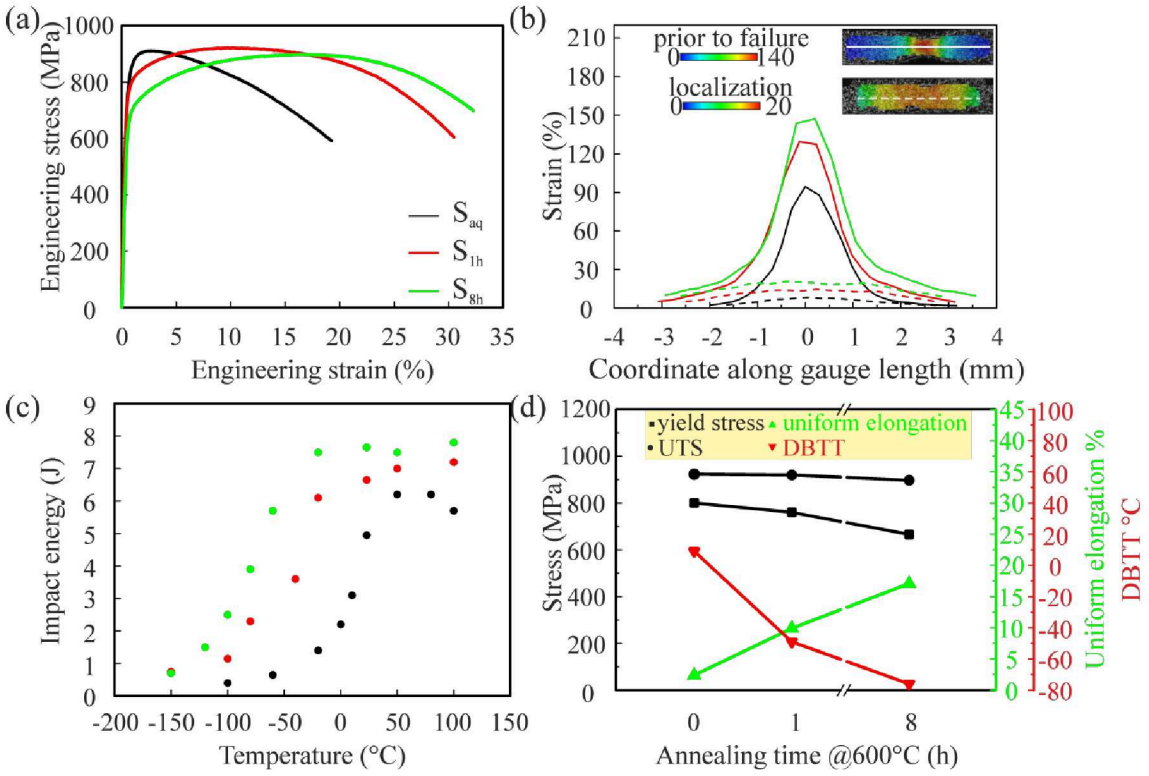

Figure 4.1: For S_{aq}, S_{1h} and S_{8h}: (a) the mechanical behavior under uniaxial tensile loading; (b) the DIC strain profiles along the gauge lengths of tensile samples at onset of necking (dashed line) and the last stage prior to failure (solid line); (c) the toughness properties obtained by impact tests carried out between -150 °C to 100 °C. Yield stress is defined as $\sigma_{0.2}$. DBTT is ductile-to-brittle transition temperature. The trends in the mechanical properties obtained from these experiments are summarized in (d). S_{aq}: as-quenched sample; S_{1h}: 1-hour heat treated sample; S_{8h}: the 8-hour heat treated sample. Source: Image from [33], Courtesy of Elsevier.

The strain hardening behaviors, the true stress strain curves and the γ_{RN} phase fraction evolution as a function of deformation are exhibited in Figure 4.2. The γ_{RN} fraction is obtained by HR-EBSD measurements on representatively large area. When comparing martensite sample S_{aq} with the 600 °C heat treated samples S_{1h} and S_{8h}, the sample with the highest initial γ_{RN} fraction, i.e. S_{8h}, exhibits the highest strain hardening rate. For the two 600 °C heat treated samples S_{1h} and S_{8h}, the γ_{RN} fraction decreases continuously during uniform deformation process (Figure 4.2).

To unravel the underlying micro-mechanisms associated with these improvements in mechanical properties, a detailed analysis of deformation and damage mechanisms are provided in the following parts of this chapter. Since the improvements in mechanical properties are most clearly

observed for sample S_{8h}, the analysis of micro-mechanisms are mainly focused on the 8-hour heat treated sample S_{8h}. Based on the strain hardening curve, the deformation process of S_{8h} is classified into three regimes: (i) early uniform deformation regime ($\varepsilon<0.05$); (ii) late uniform deformation regime ($0.05<\varepsilon<0.15$); (iii) strain localization and failure ($0.15<\varepsilon<0.20$) (Figure 4.2).

Given the differences in the microstructure constitutes, a variety of deformation mechanisms are expected to be active individually. On one hand, γ_{RN} grains are expected to accommodate strain by motion of partial dislocations, mechanical twinning and phase transformation into martensite. On the other hand, α' martensite matrix can only be deformed by dislocation slip. These differences can lead to strong strain and stress partitioning between α' martensite and γ_{RN} grains. Thus, the following analysis will focus on the strain partitioning process between the γ_{RN} and the α' martensite phases during the first two uniform deformation regimes (i-ii); and on the damage and failure mechanisms, which occur predominantly during stage (iii).

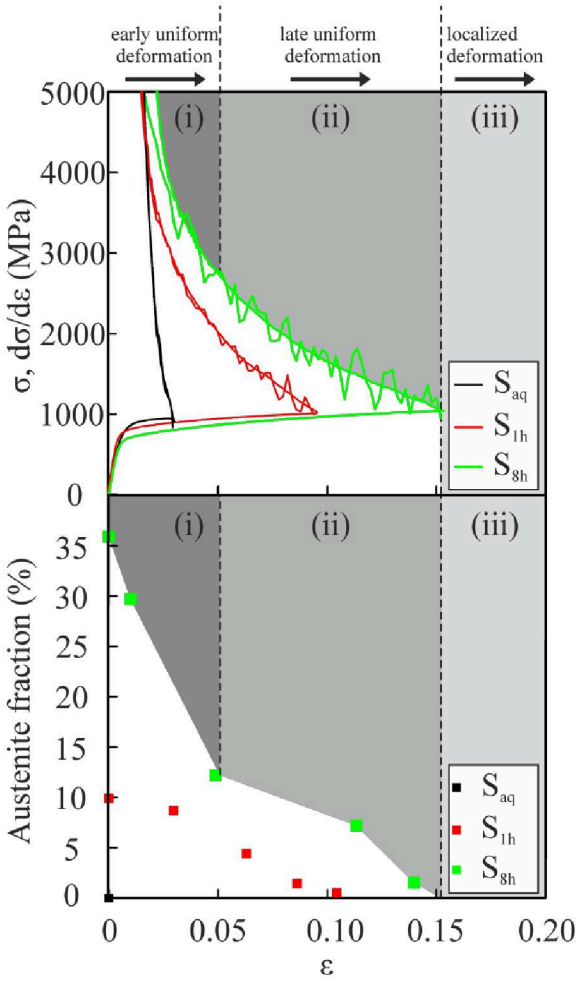

Figure 4.2: The true stress strain curve, the strain hardening (dσ/dε) curve and the evolution of γ_{RN} fraction during uniaxial tensile tests for S_{aq}, S_{1h}, and S_{8h}. Three different deformation regimes are highlighted for S_{8h}. S_{aq}: as-quenched sample; S_{1h}: 1-hour heat treated sample; S_{8h}: the 8-hour heat treated sample. Source: Image from [33], Courtesy of Elsevier.

4.2 Deformation micro-mechanisms

The strain partitioning process between α' martensite and γ_{RN} during uniform deformation regimes (i) and (ii) is investigated by employing a multi-probe mechanical testing and microstructure characterizing approach combining *in-situ* 3-point bending tests in SEM (Figure 4.3a-c), *in-situ* tensile tests with EBSD (Figure 4.3d-e, Figure 4.7), *post-mortem* TEM (Figure 4.4b_1-b_2), SXRD (Figure 4.4c) and SEM (Figure 4.4a_1-a_4, Figure 4.5, Figure 4.6) based observations.

The analysis starts with *in-situ* 3-point bending tests, which reveal heterogeneous deformation behavior within the microstructure (Figure 4.3a-c). In order to correlate the results to the strain partitioning process under uniaxial tensile testing, the tensile side of the 3-point bending sample was investigated by SE and BSE imaging. At undeformed state, the polished sample surface is flat (Figure 4.3a). After the 1st step of bending, e.g. with local strain of ~4.5%, the sample surface roughens to different levels in different areas (Figure 4.3b). The level of roughness in a specific area depends on its crystallographic orientation, e.g. by comparing different prior γ grains highlighted by white dashed outlines in Figure 4.3a. At this deformation stage, slip steps are only observed in few regions, e.g. as indicated by yellow arrows in Figure 4.3b. Since the α' martensite can only be deformed *via* slip of dislocation, which will lead to formation of slip steps on surface, the fact that surface steps are absent in most regions imply that the α' martensite accommodates plasticity only in these few regions. Mine et al. [62] also reported that plastic deformation in martensite is influenced by crystallographic orientation, e.g. plasticity of grains with highest Schmid factors are preferentially activated under external loading. Apparently, only a limited fraction of the deformation is accommodated by the α' martensite matrix at the early uniform deformation regime. However, an overall strain level of ~4.5% clearly indicates that the microstructure is plastically deformed (Figure 4.3b). To unravel the plastic deformation process within those regions where pronounced slip steps are absent, high magnification BSE images prior to and after 1st step of bending are shown in Figure 4.3b$_1$-b$_2$. Comparing these images, two distinct processes are observed in γ_{RN} grains. On the one hand, some smaller γ_{RN} grains exhibit contrast changes in BSE images, e.g. a fraction of the γ_{RN} grains lose contrast with the surrounding martensite after 1st step of bending, as highlighted by yellow arrows in Figure 4.3b$_1$. These changes in contrast, as will be shown later by the HR-EBSD phase map in Figure 4.3e, are due to occurrence of phase transformation. On the other hand, straight boundaries with dark

contrast corresponding to mechanical nano-twins are developed within some γ_{RN} grains with relatively larger size, as indicated by red arrows in Figure 4.3b_2. TEM based observation and confirmation of the occurrence of mechanical nano-twinning, and the size-dependent competition between phase transformation and mechanical twinning processes are described in details in Chapter 7. Both of these mechanisms are observed to be initiated already from the early uniform deformation regime (i) and are capable of maintaining their activity until the end of the late uniform deformation regime (ii), as was already shown for TRIP effect in Figure 4.3b. The transformation behavior of γ_{RN} grains is also crystallographic orientation dependent, where more details are described in Chapter 7. At the later steps of bending, e.g. with tensile strain of ~17.3%, slip steps are observed to be present in more regions across the sample surface (as indicated by additional yellow arrows in Figure 4.3c). As presented in the high magnification BSE image in Figure 4.3c_1, these slip traces, as highlighted by the red dashed lines, now also pass through the (transformed) γ_{RN} regions. This indicates that during this later stage of deformation a larger portion of martensite is rendered as plastic. Additional in-depth understanding of the evolution of the strain partitioning process between γ_{RN} phase and α' martensite is obtained by *in-situ* HR-EBSD measurements conducted during tensile tests (Figure 4.3d-e).

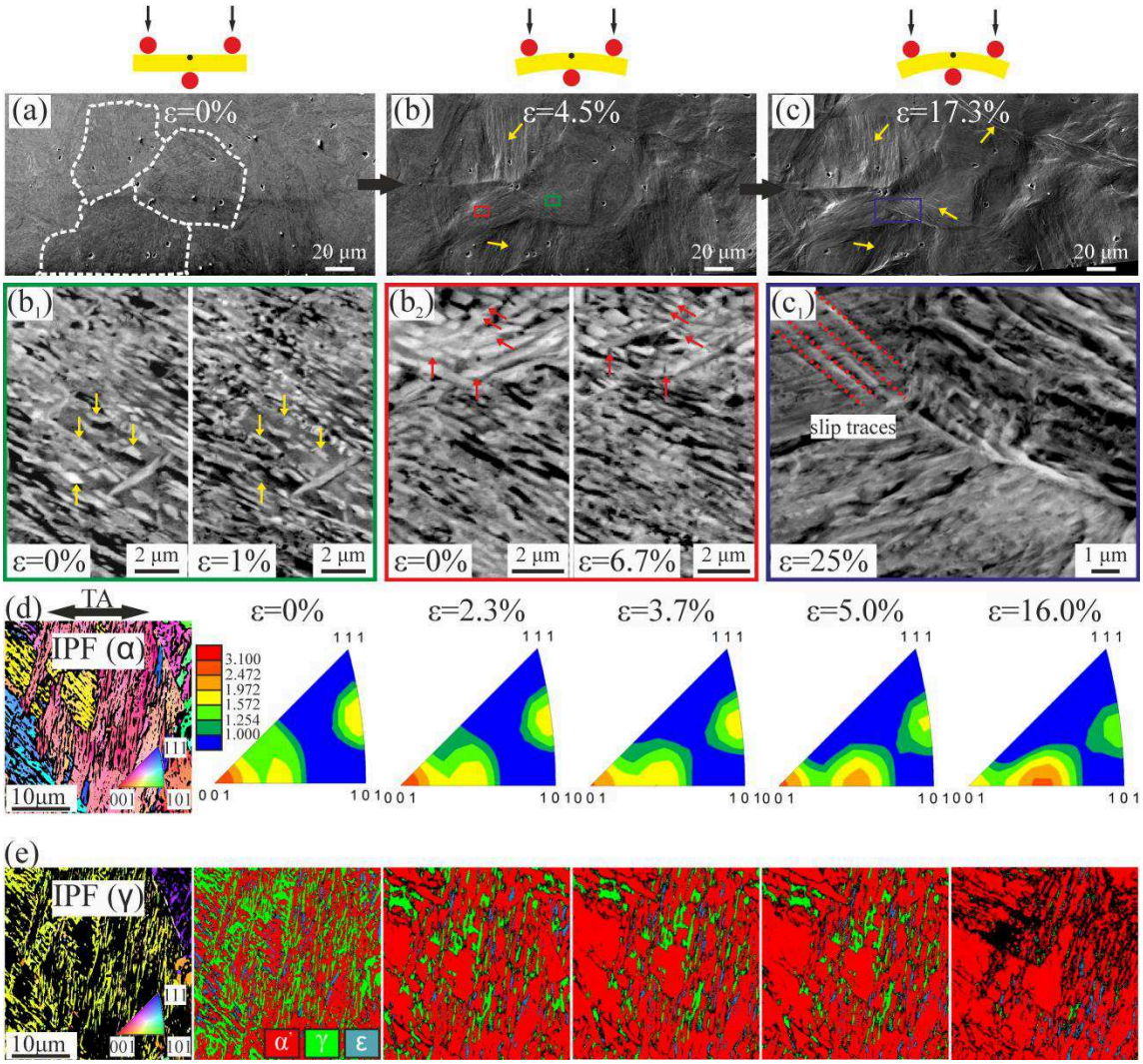

Figure 4.3: Evolution of surface topography of S_{8h} on the tension side during *in-situ* 3-point bending test in high resolution SEM: (a) undeformed state; (b) after 4.5% local deformation; (c) after 17.2% local deformation. The white dashed lines in (a) illustrate the prior γ grain boundaries. Three zoom-in BSE images show local microstructure at different levels of local strain. EBSD maps obtained during *in-situ* SEM tensile test of S_{8h}, revealing (d) IPF map of α' martensite prior to deformation, and the evolution of crystallographic orientation during deformation; (e) IPF map of γ_{RN} prior to deformation, and evolution of phase maps with straining. S_{8h}: the 8-hour heat treated sample. Source: Image from [33], Courtesy of Elsevier.

Here, the evolutions of texture in α' martensite (with respect to tensile axis) and γ_{RN} phase during *in-situ* tensile test are demonstrated for sample S_{8h}. To exhibit the initial crystallographic orientations of the α' martensite matrix and the γ_{RN} phase at undeformed state, IPF maps with respect to the tensile axis (TA) are shown on the left side of Figure 4.3d and Figure 4.3e,

respectively[2]. As shown in Figure 4.3d, up to 3.7% strain, no significant evolution of the texture component in α' martensite is present. With increasing deformation to 5.0% strain and further to 16.0% strain, a clear evolution of α' martensite texture takes place. Two plausible factors can contribute to the texture changes in the α' martensite matrix: (i) crystal rotation due to dislocation slip-mediated plasticity; (ii) formation of deformation-induced martensite. In the current 8 h treated sample S_{8h}, the γ_{RN} phase and α' martensite phase exhibit a K-S orientation relationship at undeformed state (not shown here). Thus, after phase transformation takes place under mechanical loading, the deformation-induced martensite exhibits similar orientation as the neighboring tempered α' martensite (within ~1° misorientation). Therefore, the observed texture change is ascribed to dislocation slip resulted crystal rotation in the α' martensite matrix. The fact that obvious evolution of texture takes place mainly above 3.7% global strain reveals that α' martensite mainly enters plasticity regime during the later uniform deformation regime (ii).

From the *in-situ* HR-EBSD phase maps it is observed that the γ_{RN} phase transformation rate is faster at the small strain levels, e.g. between 0% and 2.3% strain, and then it slows down during the late uniform deformation regime, e.g. from 2.3% to 5.0% strain and further to 16% strain. The trend of the γ_{RN} transformation rate is also validated by the *post-mortem* HR-EBSD measurements, where the bulk of deformed samples are measured (ruling out surface effects) (Chapter 7). Thus, it can be concluded that besides mechanical twinning, γ_{RN} phase also accommodates strain via deformation induced phase transformation. The activation of both mechanisms, i.e. TWIP and TRIP, at low strain levels indicates the stronger role of the γ_{RN} phase in the overall strain accommodation process, especially at low strain levels.

[2] Due to the difficulty of distinguishing between tempered α' martensite and deformation-induced martensite by EBSD measurements, all α' martensite in the microstructure is treated as α' martensite matrix.

The details of plastic deformation and phase transformation processes in the α' martensite and γ_{RN} grains are investigated by *post-mortem* ECCI (Figure 4.4a_1-a_4) and TEM observations (Figure 4.4b_1-b_2). At undeformed state, the microstructure of sample S_{8h} consists of α' martensite and dispersed γ_{RN} grains (Figure 4.4a_1). As shown by the high magnification ECCI image as inset in Figure 4.4a_1, α' martensite contains nano-precipitates and dislocations. After deforming to 3% strain, no significant increase in dislocation density is observed in α' martensite (Figure 4.4a_2), confirming that α' martensite is not rendered as plastic yet. However, pronounced multiplications of dislocations and interactions between dislocations and nano-precipitates in α' martensite are observed after 8% strain (Figure 4.4a_3), indicating α' martensite enters plasticity regime at this stage of deformation. With further straining to 33% strain, massive multiplication of dislocations in α' martensite occurs (Figure 4.4a_4). γ_{RN} grains, in contrast, are observed to exhibit continuous increase of stacking faults (SFs) and build-up of twin boundaries (see red arrows in Figure 4.4) from the beginning of deformation, indicating that they accommodate strain from the beginning of deformation (Figure 4.4a_1 to Figure 4.4a_3). The ECCI observations of internal structure of microstructural constitute are also validated by detailed TEM analysis (Figure 4.4b_1-b_2).

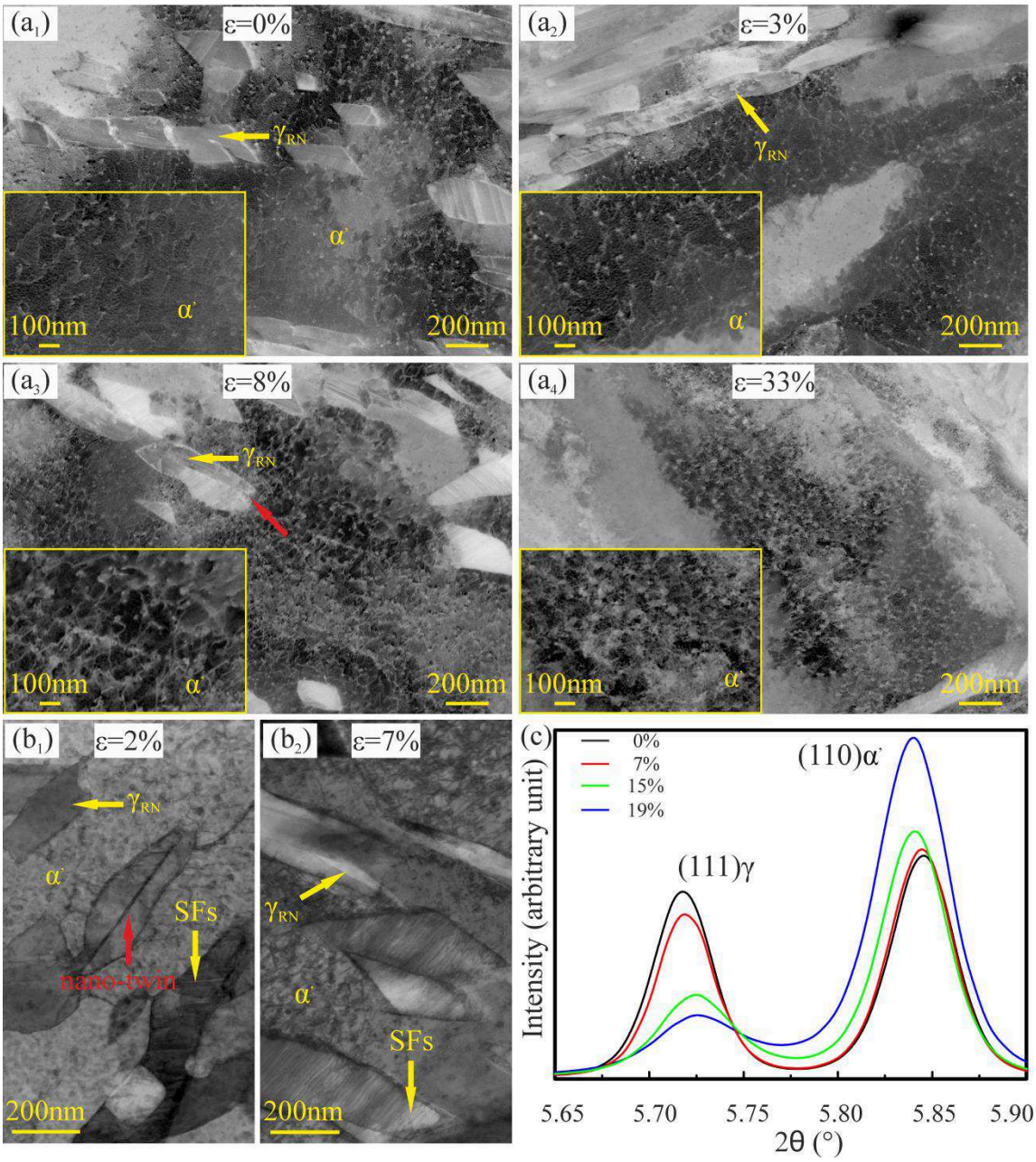

Figure 4.4: Microstructure overview for S_{8h} by *post-mortem* ECCI analysis at different strain levels: (a_1) undeformed; (a_2) 3%; (a_3) 8%; (a_4) 33%; and STEM analysis at strain of (b_1) 2%; (b_2) 7%. (c) Synchrotron X-ray diffraction profiles for (111) γ_{RN} and (110) α' martensite peaks. S_{8h}: the 8-hour heat treated sample. Source: Image from [33], Courtesy of Elsevier.

The strain partitioning process between γ_{RN} and α' martensite is further confirmed by the *post-mortem* SXRD measurements. SXRD measurements were carried out at locations of fractured tensile samples with known local strain values from DIC measurements, as shown in Figure 4.4c. Here, diffraction profiles including (111) γ_{RN} and (110) α' martensite peaks for sample S_{8h}

deformed to different strain values are shown. Since diffraction peaks of deformation-induced martensite coincide with those of tempered α' martensite, all α' martensite phase present in the microstructure is treated as α' martensite matrix. As shown in Figure 4.4c, the peak intensity of (111) γ_{RN} gradually decreases with deformation while that of the (110) α' martensite simultaneously increases (from black, to red, to green and to blue curves), indicating occurrence of phase transformation. This transformation behavior observed by SXRD is consistent with the observation from previous HR-EBSD measurements (Figure 4.2, Figure 4.3e). Meanwhile, it is observed that the profile of (111) γ_{RN} peak exhibits an asymmetric peak broadening and overall shifting to higher 2θ values with increasing strain. However, the (110) peak of α' martensite broadens symmetrically, especially after 7% macroscopic strain, and is moved to lower 2θ values with deformation. An asymmetric peak broadening and shifting to higher 2θ values of the γ_{RN} peaks indicate formation of SFs and twins [63]. Symmetric broadening and moving to lower 2θ values in martensite imply increased dislocation density with increasing deformation [64].

Based on the overall analysis conducted by *in-situ* 3-point bending measurements (Figure 4.3a-c), ECCI (Figure 4.4a_1-a_4) and TEM analysis (Figure 4.4b_1-b_2), SXRD measurements (Figure 4.4c), *in-situ* EBSD (Figure 4.3d-e) and *post-mortem* EBSD measurements (Figure 4.2), it is able to hypothesize the following structure evolution sequence. At the early uniform deformation regime, the plastic strain is preferentially partitioned into γ_{RN} phase by motion of partial dislocations, formation of SFs, mechanical twinning, and then phase transformation into martensite. Apart from few martensite regions with favored orientation, the majority of the α' martensitic matrix is rendered as plastic during the late uniform deformation stage. Thus, in this second deformation regime, plasticity is accommodated both by the α' martensite and remaining γ_{RN} phase, while the (high defect density) deformation-induced α' martensite regions (previous γ_{RN} grains) do not

exhibit indications of plasticity. Only at very high deformation levels, e.g. within the localized neck, plastic deformation of the deformation-induced α' martensite is observed.

4.3 Damage and failure micro-mechanisms

The third regime defined in the hardening curve (Figure 4.2) is analyzed next by characterizing the damage evolution process, i.e. nucleation, growth and coalescence of micro-cracks. The damage micro-mechanisms are unraveled by *post-mortem* SEM analysis on locations of tensile fractured samples with well-defined local strain values from DIC measurements (Figure 4.5, Figure 4.6) and *in-situ* SEM analysis (Figure 4.7).

The damage evolution process along cross section of fractured tensile sample (Figure 4.5a_1-a_4) and the fracture surface topography (Figure 4.5b_1-b_4) of the martensite sample S_{aq} and the martensite-reverted austenite sample S_{8h} are compared first. For both samples, only a limited number of damage incidents are observed before necking takes place. In sample S_{aq}, after necking takes place, damage process occurs via nucleation of micro-cracks of several micrometers size, as shown by the high magnification inset in Figure 4.5a_1. These cracks are heterogeneously distributed in the martensite microstructure. With further straining, e.g. 100% strain towards fracture, higher density of damage incidents can be observed. At the same time, the size of the cracks also increases (see inset in Figure 4.5a_2). Tensile test sample S_{aq} exhibits a ductile fracture surface with dimples at ambient temperature (Figure 4.5a_3). The impact test sample fractured at -196 °C, however, exhibits a cleavage fracture surface (Figure 4.5a_4). The cleavage fracture surface is in accordance with the low impact energy of S_{aq} at -196 °C (Figure 4.1).

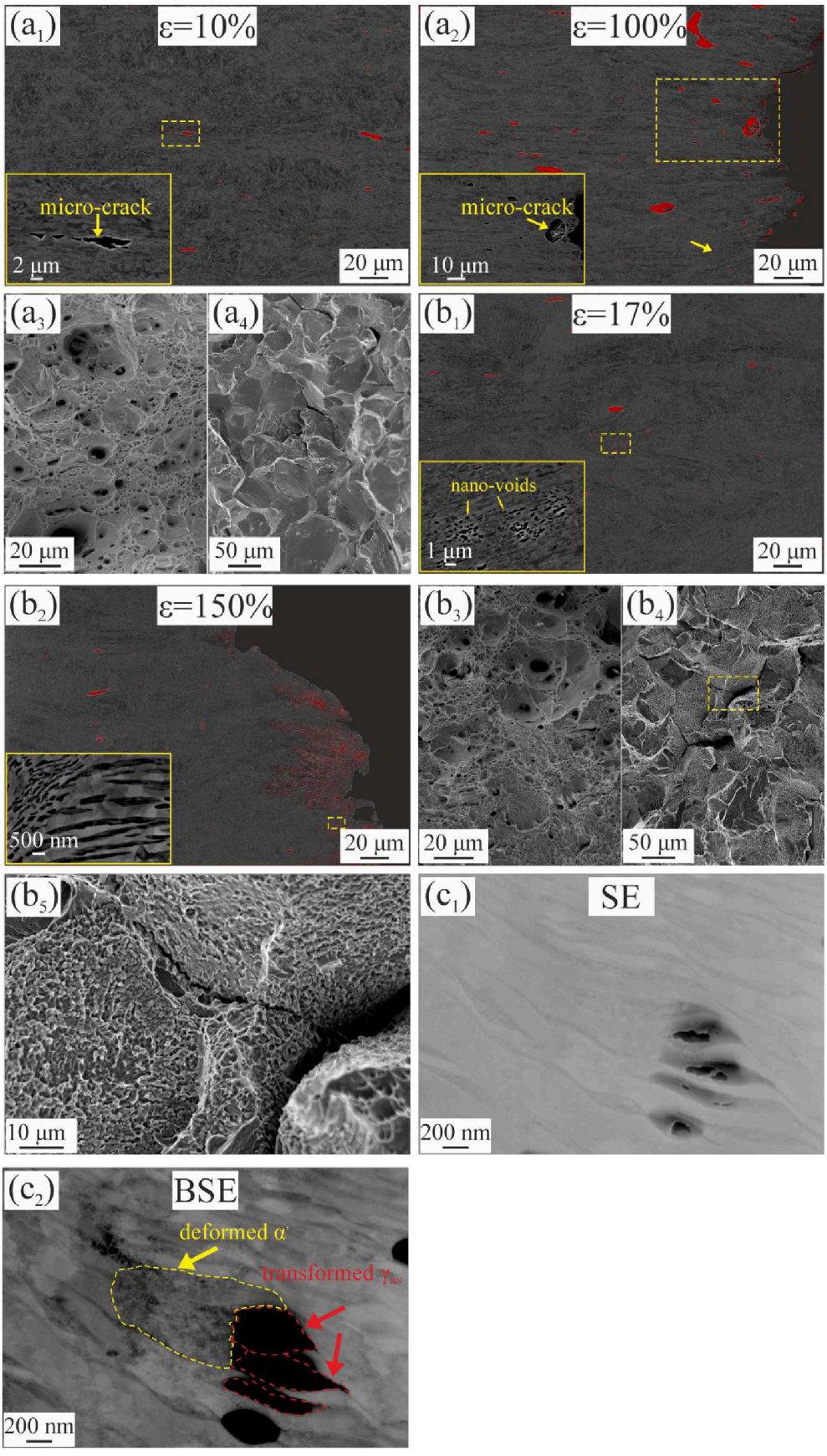
(a1)
ε=10%
micro-crack
2 μm
20 μm
(a2)
ε=100%
micro-crack
10 μm
20 μm
(a3)
20 μm
(a4)
50 μm
(b1)
ε=17%
nano-voids
1 μm
20 μm
(b2)
ε=150%
500 nm
20 μm
(b3)
20 μm
(b4)
50 μm
(b5)
10 μm
(c1)
SE
200 nm
(c2)
BSE
deformed α
transformed γ
200 nm

Figure 4.5: Damage evolution process for S_{aq}: (a_1) BSE image of necking area; (a_2) BSE image of area close to fracture surface; (a_3) fracture surface of sample tensile tested at room temperature; (a_4) fracture surface of sample impact tested at -196 °C. For S_{8h}: (b_1) BSE image of necking area; (b_2) BSE image of area close to fracture surface; (b_3) fracture surface of sample tensile tested at room temperature; (b_4) fracture surface of sample impact tested at impact test at -196 °C and (b_5) high magnification image of the fracture surface in b_4. High magnification BSE images are shown as inset for corresponding images. (c_1, c_2) High resolution SE and BSE images of micro-cracks in S_{8h}. S_{aq}: as-quenched sample; S_{8h}: the 8-hour heat treated sample. Source: Image from [33], Courtesy of Elsevier.

A surprisingly different damage evolution process is observed in the martensite-reverted austenite sample S_{8h}. After necking, damage takes place by nucleation of numerous nano-voids in the microstructure, as demonstrated by the high magnification inset in Figure 4.5b_1. In contrast to the formation of micro-cracks as in the martensite sample S_{aq}, these nano-voids are well confined by the nano-laminated morphology of the microstructure in sample S_{8h}. The tips of the majority of these nano-voids are round, implying pronounced plastic deformation process at these crack tips. Further deformation to fracture is accommodated by massive nucleation of such nano-voids. Interestingly, in many cases growth into larger cracks via nano-voids coalescence is delayed, even when the spacing between these nano-voids is decreased to below ~100 nm. As revealed by the high magnification SE and BSE images in Figure 4.5c_1-c_2, these nano-cracks are nucleated at the interface between deformation-induced martensite and deformed matrix martensite regions (with high dislocation density). Further deformation leads to the full delamination of the individual grains at the interface, which leave behind a shallow cavity in the SE image in Figure 4.5c_1 with respect to the surrounding flat cross-section. However, these cracks are successfully arrested by the nano-laminated morphology of the microstructure, as shown in Figure 4.5b_2. A high magnification view of an interfacial crack demonstrates that this crack is arrested by the deformation of the neighboring α' martensite, as highlighted by the yellow arrow in Figure 4.5c_2. As a result of this process, the martensite-reverted austenite sample S_{8h} exhibits dimpled ductile fracture behavior at ambient temperature (Figure 4.5b_3). Similar to the behavior of the impact sample S_{aq}, impact sample S_{8h} exhibits a brittle failure upon -196 °C impact testing. However, in

contrast to martensite sample S_{aq}, the impact fracture sample S_{8h} exhibits fibrous surface features, which is a footprint of the plastic deformation of the duplex phase nano-laminate morphology martensite-reverted austenite microstructure (Figure 4.5b_4 and high magnification image in Figure 4.5b_5).

To further understand the distinct damage evolution process in different microstructure shown in Figure 4.5, the damage incidents therein are quantified and shown in Figure 4.6. For different locations with DIC-based local strain values, high resolution SE images with optimized contrast for imaging cracks are obtained. Then these images are analyzed using the Image J software [65], [66] to determine the evolution of the density (Figure 4.6a) and area fraction (Figure 4.6b) of the damage incidents with respect to the local plastic strain. Using the two data sets, the evolution of the average damage incident size is calculated and plotted in Figure 4.6c.

In Figure 4.6, the strain for localized necking is indicated by dashed lines. Within the uniform deformation regime, both martensite sample S_{aq} and martensite-reverted austenite samples S_{1h} and S_{8h} contain only small area fraction of micro-cracks (~0.01%). After necking, the density of damage incidents increases almost monotonously with local plastic strain for both samples S_{aq} and S_{1h} (Figure 4.6a). For sample S_{8h}, however, the increase in density of damage incidents maintains at a small level up to very high strain levels, e.g. local strain of ~150% when approaching fracture surface. A similar trend is observed for the damage area fraction evolution, where sample S_{aq} shows a drastic early increase and samples S_{1h} and S_{8h} exhibit a respectively moderate and late increase as a function of local plastic strain (Figure 4.6b). Compared to samples S_{aq} and S_{1h}, sample S_{8h} exhibits the smallest crack size at the same strain level (Figure 4.6c), demonstrating the existence of effective damage arresting mechanisms. To unravel the damage arresting mechanism in microstructure of sample S_{8h} in more details, deformation

process of microstructure with nucleated cracks is investigated. For this purpose, a 15% pre-strained S_{8h} sample is re-polished and the evolution of the microstructure is further examined by *in-situ* tension in SEM (Figure 4.7). The EBSD phase map and SE image of the 15% pre-strained and re-polished sample surface are shown in Figure 4.7a_1 and Figure 4.7a_2, respectively. The SE image shows the existence of two inclusions (outlined by red in Figure 4.7a_2) in the microstructure. Due to the deformation incompatibility along boundary of inclusion and the surrounding microstructure, stress concentration arises at the interfaces during deformation, causing inclusions inevitably to act as damage sites. The essential point to highlight here is that even when damage is nucleated due to the presence of inclusions, the damage is successfully arrested by the microstructure. As highlighted by yellow outlines in Figure 4.7b and Figure 4.7c, the damage proceeds via coalescence of nano-voids and further deformation is accommodated by the surrounding α' martensite matrix via formation of slip steps (as indicated by green arrows in Figure 4.7c).

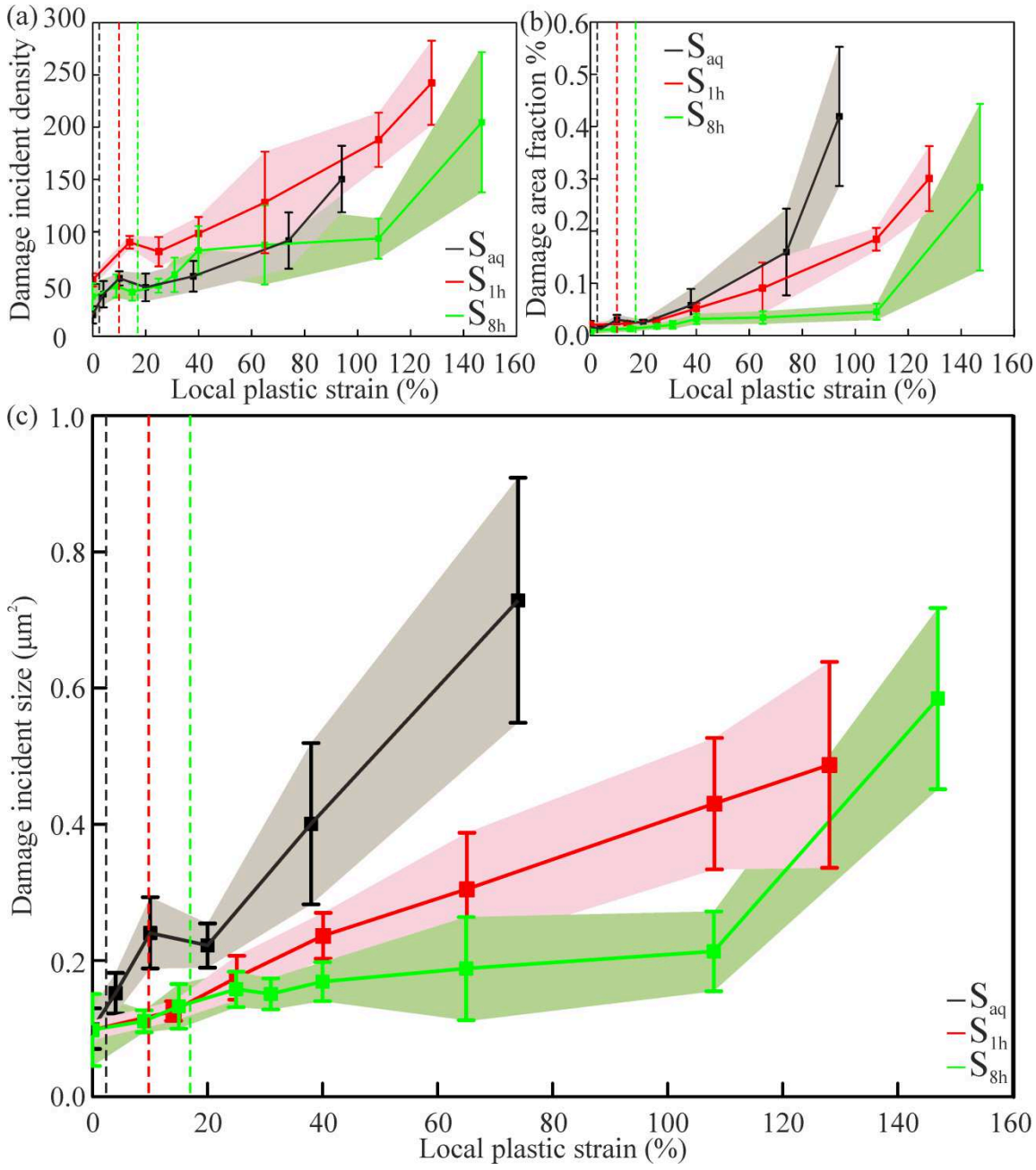

Figure 4.6: Quantification of damage mechanisms in S_{aq}, S_{1h} and S_{8h} as a function of deformation: (a) damage incident density; (b) damage area fraction; (c) damage incident size. Dash line indicates the necking strain for each sample. S_{aq}: as-quenched sample; S_{1h}: 1-hour heat treated sample; S_{8h}: the 8-hour heat treated sample. Source: Image from [33], Courtesy of Elsevier.

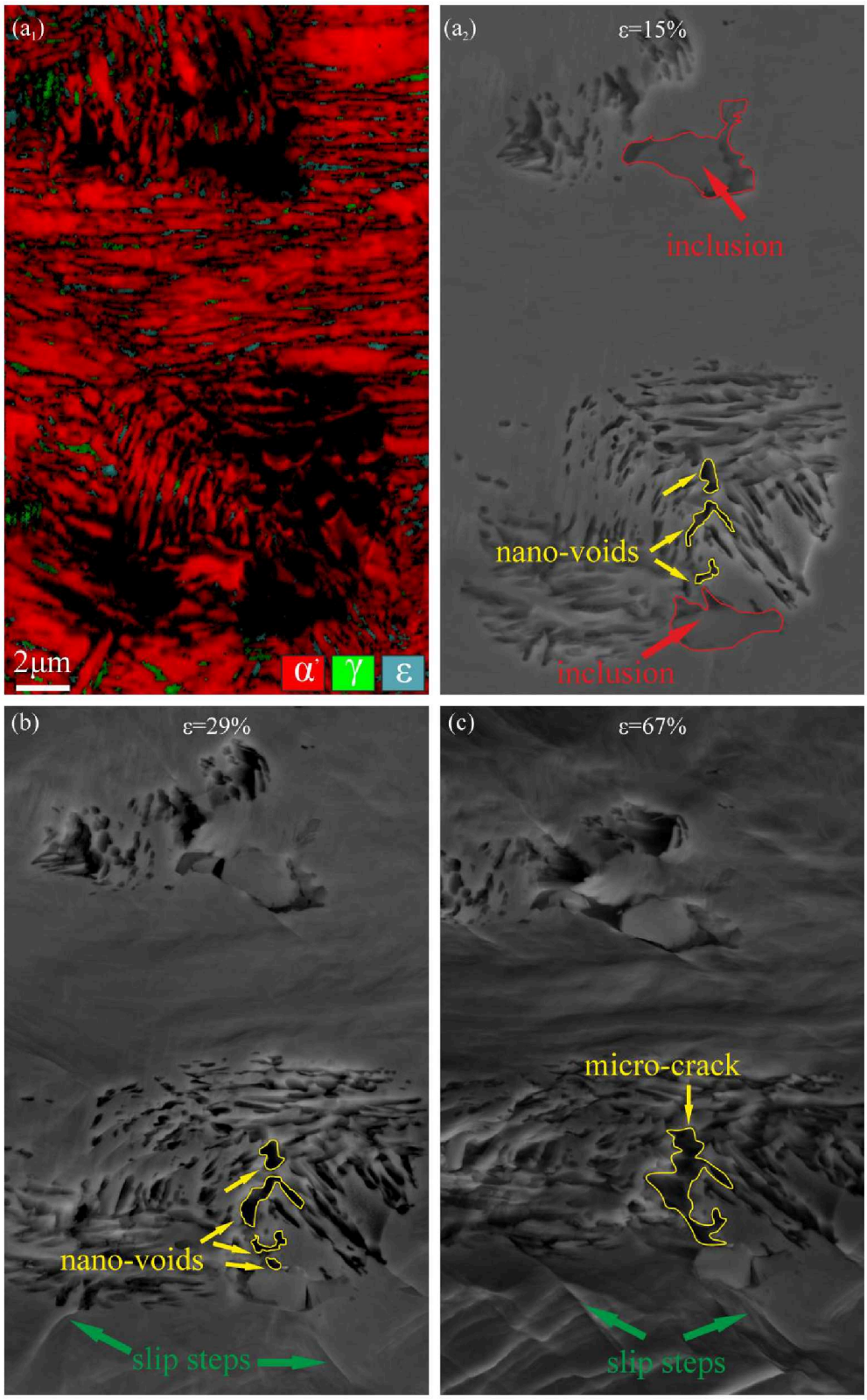

Figure 4.7: Interactions of micro-cracks with the surrounding phases in S_{8h} revealed by *in-situ* tensile test, as characterized by (a_1) EBSD phase map; (a_2) SE imaging of area in a_1; (b, c) SE imaging of this area after

further straining to 29% and 67%, respectively. S_{8h}: the 8-hour heat treated sample. Source: Image from [33], Courtesy of Elsevier.

4.4 Discussion

4.4.1 Overview of deformation micro-mechanisms

Based on the observations above, a schematical sketch of the deformation, damage and failure micro-mechanisms is provided for the 8-hour reversion treated sample S_{8h} (Figure 4.8).

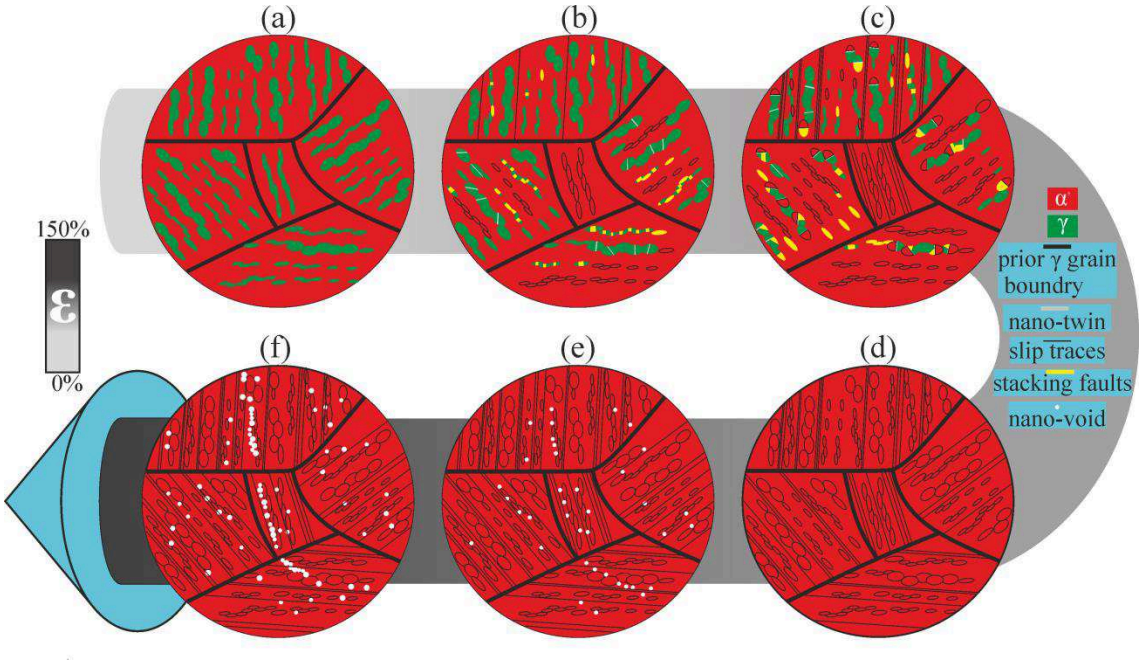

Figure 4.8: Schematical sketch of the deformation, damage and failure micro-mechanisms in the 8-hour reversion heat treated sample S_{8h}. Source: Image from [33], Courtesy of Elsevier.

At undeformed state, the microstructure of sample S_{8h} consists of the α' martensite phase (phase in red) and the γ_{RN} phase (phase in green) (Figure 4.8a). At early stage of deformation, strain is preferentially partitioned into the γ_{RN} phase *via* multiple deformation mechanisms, i.e. formation of SFs (area in yellow), mechanical twins (area in grey), and phase transformation into martensite. At these small strain levels, only certain α' martensitic regions with favored crystallographic

orientations enter plastic region, as documented by the formation of slip traces (black lines) (Figure 4.8b). With gradually increasing strain, more martensitic regions are rendered as plastic and a strain accommodation process by both the α' martensite phase and the γ_{RN} phase is observed (Figure 4.8c). During the later uniform deformation regime, the martensitic phase transformation is completed and the whole microstructure is plastically deformed (Figure 4.8d). Although the whole microstructure is martensite now, the two types of martensite, i.e. deformed matrix martensite and deformation-induced martensite, can still be distinguished from each other. They exhibit different defect densities and chemical compositions, and the microstructure still maintains the nano-laminate morphology. Hence, even when both of them are indexed as "martensite", a composite-like deformation behavior of the nano-laminate morphology microstructure is still expected with further straining. In the post-necking deformation regime (Figure 4.8e-f), the damage process takes place via nucleation, growth and coalescence of nano-voids, and most damage incidents are well confined by the inherited nano-laminate morphology of the microstructure. This is in accordance with the sandwich effect reported by other works [8]–[11].

The analysis provided here underlines that due to the deformation-induced martensitic transformation and the resulted defect density evolution within the microstructure, the strain partitioning process is actively modified during deformation. This phenomenon is referred to as *dynamic strain partitioning*.

4.4.2 Relationship between mechanical properties and deformation micro-mechanisms

As systematically demonstrated above, aging-induced modifications in the martensite microstructure influence the overall mechanical properties significantly, especially in regard to the strength, the strain hardening behavior and the overall ductility of martensitic steels. In the

following discussion of the relationship between the enhanced mechanical properties and the deformation micro-mechanisms, special focus is placed on the analysis of the strain hardening behavior and damage resistance, which play the critical roles in these improvements. However, it should be kept in mind that these enhanced properties are intrinsically linked with each other, and usually there are resulted from operation of multiple micro-mechanisms. For example, the decrease in yield strength $\sigma_{0.2}$ is associated with (i) the annihilations of dislocations in the α' martensite during annealing; (ii) less effective precipitation hardening due to the coarsening of the nano-precipitates during prolonged annealing at 600 °C; and (iii) partial replacement of 'hard' α' martensite regions with 'soft' γ_{RN} grains [67], [68]. Another example is regarding the preserved UTS after the reversion treatment. Here precipitation hardening mechanism (i.e. the maraging effect) definitely plays an important role, however the factors contributing to improve the strain hardening rate or limit the damage-induced softening (both of which will be discussed next) also play an indirect but important role.

The enhanced strain hardening rate can be attributed to the activation of multiple deformation mechanisms within microstructural constitutes and the resulting dynamic strain partitioning process. In the early uniform deformation regime ($0<\varepsilon<0.05$), the 'softer' γ_{RN} phase dominates the deformation process through activating its intrinsic multiple deformation mechanisms, i.e. motion of partial dislocations, formation of SFs (Figure 4.4), mechanical twinning (TWIP) (Figure 4.3b_2), and martensitic phase transformation (TRIP) (Figure 4.2, Figure 4.3e, Figure 4.4c). However, due to a wide variation in the mechanical stability of the γ_{RN} grains, e.g. resulted from a size-dependent competition between twinning and phase transformation processes (Chapter 7), the associated phase transformation exists over the entire uniform deformation regime (Figure 4.2). Similar mechanical benefits from adjusting variations in austenite stability can also be introduced through varying the C content, the crystallographic orientation and properties of neighboring

phase, as reported by Jacques et al. [24]. The α' martensite is rendered plastic in the late uniform deformation regime (ε>0.05), which is confirmed by the formation of slip steps during *in-situ* 3-point bending (Figure 4.3c$_1$), evolution of the typical BCC deformation texture during *in-situ* tension [69], [70] (Figure 4.3d) and an increased dislocation density during *post-mortem* ECCI and SXRD measurements (Figure 4.4a$_1$-a$_4$, Figure 4.4c). Thus, the significance of the presence of the well-dispersed TRIP-TWIP behaviors in γ_{RN} grains lies in enabling the strain hardening capacity of the α' martensite matrix to be consumed in more conservative manner. As the annealing process triggers precipitation of nano-particles [45], [47] and decrease in dislocation density in the α' martensite, the occurrence of dislocation multiplications and their interaction with nano-particles during plastic deformation, e.g. via the Orowan mechanism, lead to improved α' martensite strain hardening capacity [18], [71]–[76]. The importance of these beneficial effects is underlined upon comparison to the martensite sample S_{aq}, where the limited strain hardening capacity of α' martensite become quickly exhausted and the sample exhibits earlier necking. In summary, the presented observations here also underline that microstructures composed of an (initially softer) metastable phase with a wide dispersed mechanical stability, and an (initially harder) phase but still occupies further strain hardening capacity, exhibit ideal overall strain hardening behavior upon deformation. Similar indications are also reported in other works, e.g., study of the strain/stress partitioning behaviors among microstructural constitutes in multiphase TRIP-assisted steels. Tomota et al [22] underlined the importance of optimizing the critical stress for activating ferrite plasticity and martensite phase transformation, to achieve improved mechanical properties.

Given the additional reserved deformation capacity created by replacing the less ductile martensite by ductile austenite, and the aforementioned optimized strain hardening behavior, it is not surprising to observe the increased uniform ductility in TRIP-maraging steels. However,

since almost all the γ_{RN} grains are transformed into martensite prior to necking (Figure 4.2), the enhanced post-necking deformation behavior in S_{8h} is unexpected. This improvement is ascribed to the crack arresting ability of the nano-laminate morphology of the microstructure. In the martensite sample S_{aq}, after the onset of strain localization, damages proceed via formation of micro-cracks which nucleate continuously and exhibit monotonic growth with ongoing deformation (Figure 4.5a_1-a_4). In low carbon martensitic steels, martensite laths within one martensite block mutually exhibit low angle misorientations [77]. Thus, the cleavage planes {001} planes in neighboring martensite blocks are not much misaligned. This means that once a crack is initiated during deformation, it can easily propagate along cleavage planes through the microstructure without experiencing much obstacles [78]. In the reversion-treated sample $S_{8h,}$ in contrast, nano-voids are nucleated along interfaces in the microstructure, which later coalescence into nano-cracks along full interface. However, the nano-laminate morphology created by neighboring deformed matrix martensite and deformation-induced martensite regions successfully inhibit further growth of these nano-cracks with increasing strain (Figure 4.5b_1-b_5, Figure 4.5c_1-c_2). To be more specific, the specific morphology and the high density of the interface provide the microstructure with a high damage arresting ability [49]. Even in the extreme case where inclusions are present, the nucleated cracks due to deformation incompatibility are observed to be successfully arrested and well-confined by the nano-laminate morphology of the microstructure. Consequently, the associated high localized stress with the crack can be re-distributed in the microstructure, and catastrophic failure is avoided (Figure 4.7). Note that this mechanism of stress-delocalization also enables further deformation of the surrounding microstructure, where larger fractions of the microstructure can continue to contribute to strain hardening.

The observed consistence in improved toughness can also be explained in connection with the enhanced crack arresting ability of this nano-laminate morphology of the microstructure. As reported in the literature, the influence of metastable austenite on toughness depends on the balance between the energy dissipated at the crack tip during phase transformation and the fracture properties of the deformation-induced martensite [79]–[81]. In this regard, a propagating crack in the current nano-laminate morphology microstructure encounters a high density of interfaces ahead, and the deformation-induced martensite (with negligible carbon content) exhibits higher toughness compared to those (with higher carbon contents) in other TRIP steels.

4.4.3 Reflections on microstructure design

In TRIP-assisted steels (e.g. quenching and partitioning and/or tempering steels (Q-P-T steels)), the majority of the research efforts has so far focused on correlating the austenite phase stability and volume fraction with the overall strength and ductility [23], [38]–[41], [82]–[85]. Only a few relevant works have addressed the underlying deformation mechanism within each microstructural constitute [86], [87] and the interplay [88], [89]. The results demonstrated here on the deformation, damage and failure micro-mechanisms, however, underline the importance of these interactions, and enable a more general discussion of the targeted microstructure design. The obtained understanding is more crystal-clear upon comparison to other traditional alloys and the associated deformation micro-mechanisms. In dual phase steels (DP steels) with a microstructure consisting of soft ferrite matrix and hard martensite islands [90]–[94], for example, the strain is mainly accommodated by the former phase while the stress is mainly accommodated by the latter phase. The strain/stress partitioning behavior is maintained from the beginning of deformation onwards [94]. The mechanical properties of the microstructural constitutes, their individual chemical composition, orientation, the volume fraction, size, morphology and distribution of martensite are observed to significantly influence the strain/stress partitioning

process and play an important role in the failure mechanisms [92]–[95]. However, in almost all DP microstructures (except for TRIP-assisted UFG-DP [42], [96], [97]), the strain partitioning process is effectively static (at least up to the point of strain localization), and only a certain portion of the entire strain hardening capacity of the microstructure is consumed. In conventional TRIP-assisted multiphase steels, due to the presence of metastable retained austenite in the microstructure, a dynamic strain partitioning process does exist [22]. However, as a result of large grain size of the ferrite matrix grains (usually above several μm), a heterogeneous strain partitioning within different ferrite grains dominates the deformation process, e.g. some ferrite grains may not contribute to strain partitioning at all [24]. TRIP-maraging steels, however, effectively benefit from these effects as the TRIP effect is introduced in a nano-laminate morphology microstructure. The combination of transformation induced plasticity and a confined size promotes that a larger portion of the microstructure contributes to the strain hardening capacity upon deformation. This is in accordance with other works on steels with nano-laminate morphology microstructures with extraordinary properties, e.g. nanostructured bainitic steels [98], [99] or pearlite [100], [101].

Chapter 5 Enhancing resistance of lath martensite to hydrogen embrittlement by introducing nano-films of interlath austenite[3]

5.1 Introduction

A fundamental understanding of hydrogen-assisted embrittlement mechanisms is critical for development of future hydrogen-energy based industry applications. The susceptibility of structural steels to hydrogen embrittlement (HE) usually increases with increasing strength [27], [102]. Deterioration of ductility caused by HE, place infrastructures made of high strength steels under high risk of exhibiting unexpected catastrophic failure during service. Martensite, the major microstructure constituent that delivers high strength in structural steels, suffers from HE most severely. Thus, a deep understanding of HE mechanisms is essential for rescuing the corresponding infrastructures from unexpected catastrophic failure during service. Three main HE mechanisms, namely, hydrogen enhanced localized plasticity (HELP), hydrogen enhanced decohesion (HEDE) and hydrogen enhanced strain induced vacancy (HESIV), are described here. The HELP mechanism suggests that mobile hydrogen decreases barriers to dislocation motion, thereby increasing dislocation mobility and slip planarity, leading to heterogeneous localized deformation and formation of subcritical crack [103]. The HEDE mechanism suggests that atomic bonding is weakened due to the presence of hydrogen, resulting in easy decohesion of boundaries/interfaces [104]. The HESIV mechanism proposes that the primary function of hydrogen in degradation is to enhance the strain induced vacancy formation and agglomeration, thus promoting fracture process [105]. All mechanisms essentially point out that it is the diffusible hydrogen within the microstructure that causes the HE.

[3] The main content of Chapter 5 is based on [34] M.-M. Wang, C. Tasan, M. Koyama, D. Ponge, and D. Raabe, "Enhancing hydrogen embrittlement resistance of lath martensite by introducing nano-Films of interlath austenite," Metall. Mater. Trans. A, pp. 0–5, 2015.

In order to aid structural steels from HE, especially those steels with high strength, it is essential to reduce diffusible hydrogen content in the microstructure. Thus, over past decades, numerous investigations focus on utilizing microstructure features as effective hydrogen traps and studying their effectiveness on trapping hydrogen [30], [106], [107]. Depending on the activation energy Q, hydrogen traps can be classified into two types, namely, reversible traps (Q<50 kJ/mol) and irreversible traps (Q>50 kJ/mol) [108]. Reversible hydrogen traps can immobilize hydrogen and release hydrogen at low temperatures. Irreversible hydrogen traps can continuously absorb hydrogen until become saturated, and either release hydrogen at higher temperature or prevent it from escaping. Reversible hydrogen traps include grain boundaries, dislocations, coherent/semi-coherent particles and micro-voids, etc. [107]. Irreversible hydrogen traps consist of incoherent particles and retained austenite, etc. [107]. Majorities of these works have successfully shown the effectiveness of decreasing diffusible hydrogen content via introducing hydrogen traps. Tsuchiyama et al., for example, have shown that via introducing stable austenite layers, the permeation of hydrogen into the interior of cold rolled plates (with martensitic microstructure) can be inhibited within a certain charging time period, thus significantly improving resistance of the steels to HE [30]. Fielding et al., for example, have examined the role of percolating austenite in hindering hydrogen passage into the steel during charging [106].

Within these enormous amounts of work on characterizing the capacity of different microstructural features as hydrogen traps, the influence of hydrogen on mechanical properties is mainly assessed via tensile testing and thereafter a hypothesized HE mechanism via examination of fracture surfaces. However, these limits further in-depth understanding of HE mechanisms for two main reasons. First, tensile testing only examines the global reaction of the sample under external loading in the presence of hydrogen, thus fails to provide information in microstructure scale. Second, the examination of the fracture surface, i.e. the product of the final fracture, is

insufficient to describe the hydrogen initiated damage nucleation and evolution process. Thus, to assess the resistance of a certain microstructure to HE and understand the HE mechanism, a mechanical testing capable of examining local response of the microstructure under external loading incorporated with local microstructure characterization are demanded.

In this context, the nano-laminate martensite-reverted austenite microstructure delivers itself as a promising candidate with high resistance to HE for two reasons. First, the microstructure exhibits high damage resistance without the presence of hydrogen (Chapter 4). Second, reverted austenite and precipitates in matrix act as additional hydrogen traps, thus being able to decrease diffusible hydrogen content.

In this chapter, the introduction of nano-films of reverted austenite into martensite as a remedy for aiding martensitic steels from HE is examined. Meanwhile systematic investigations of local microstructure evolutions are carried out to unravel the damage nucleation, growth and coalescence processes.

5.2 Experimental procedure

To introduce nano-films of austenite into lath martensite, reversion-treatments of as-quenched martensite were performed at 600 °C for 1 h and 8 h, yielding reverted austenite nano-films (γ_{RN}) with thickness of ~200 nm and ~500 nm, respectively. Since what is critical here in Chapter 5 are the γ_{RN} thicknesses in martensite, the obtained microstructures are referred in this chapter based on the γ_{RN} thickness: i.e. *M* (no γ_{RN}), MA_{200nm} and MA_{500nm}.

To test the susceptibility of the material to HE, tensile samples were first pre-charged with hydrogen and then they were tensile tested at ambient temperature. Hydrogen charging was carried out in 5% H_2SO_4 aqueous solution containing 3g/l NH_4SCN as hydrogen recombination poison. The cathodic current density was 5 A/m^2. A platinum foil was used as the counter

electrode. Based on the effective diffusion coefficient (D) of hydrogen in low alloy martensitic steel (3.70×10^{-11} m^2s^{-1}) at ambient temperature [109] and calculated diffusion distance ($\sim\sqrt{Dt}$), it was estimated that hydrogen can diffuse through sample thickness (~0.5mm) after 25 min charging in martensitic sample *M*. For control experiments, the same charging condition was applied to martensite-reverted austenite samples MA_{200nm} and MA_{500nm}. Samples after hydrogen pre-charging are referred to as $(M)_H$, $(MA_{200nm})_H$ and $(MA_{500nmm})_H$. Since for all three samples martensitic matrix forms a continuous network in the microstructure and it acts as channels for hydrogen to diffuse through sample thickness, it is expected that no hydrogen concentration gradient from surface towards the center of the specimen exists.

The hydrogen desorption rate was measured by thermal desorption spectroscopy (TDS). Disks with diameter of 9.0 mm and 0.5 mm thickness were used for TDS measurements. Diffusible hydrogen is defined as the hydrogen that diffuses at ambient temperature. After hydrogen pre-charging under the aforementioned conditions, samples were inserted into a TDS chamber within ~5 min. TDS measurements were performed for samples $(M)_H$ and $(MA_{500nm})_H$. For martensite sample $(M)_H$, the evacuation time to achieve required vacuum condition was ~20 min. Due to the high diffusible hydrogen content in martensite-reverted austenite sample $(MA_{500nm})_H$, it took ~1 h evacuation time to reach required vacuum condition. Due to the existence of high density martensite/γ_{RN} interfaces which act as irreversible hydrogen traps, the influence of 1 h evacuation is considered not to be critical. For the TDS measurements, each sample was heated from 298 K (25 °C) to 873 K (600 °C) at a heating rate of 0.433 K/s. The diffusible hydrogen content was determined by measuring the cumulative hydrogen detected between 298 K (25 °C) and ~573 K (300 °C).

To assess the resistance of these microstructures to HE, samples were first charged with hydrogen and then tensile tested within 15min after pre-charging. The gauge dimensions of tensile samples are 4.0 mm length × 2.0 mm width × 0.5 mm thickness. Tensile tests were carried out with an initial strain rate of 10^{-3} s^{-1} with local strain measured by digital image correlation (DIC) analysis. The microstructures were characterized by SE imaging, EBSD and ECCI measurements at locations with known strain values from DIC measurements [110], [111].

5.3 Results and Discussion

For an explicit understanding, EBSD phase maps of as-quenched martensite sample *M*, and martensite-reverted austenite samples MA_{200nm} and MA_{500nm} are shown again in Figure 5.1a-c. Prior to reversion treatment, the microstructure of sample *M* consists of single martensite phase (Figure 5.1a). After 600 °C 1 h annealing, γ_{RN} grains with ~10% volume fraction and thickness of ~200 nm are formed along martensite boundaries in sample MA_{200nm} (Figure 5.1b). After 8 h annealing at 600 °C, volume fraction of γ_{RN} grains increase to ~34% and γ_{RN} grains grow to ~500 nm thick in sample MA_{500nm} (Figure 5.1c). For both samples MA_{200nm} and MA_{500nm}, less than 4% volume fraction ε martensite are present in the microstructure. The following analysis in Chapter 5 are mainly focused on samples *M* and MA_{500nm}. The hydrogen desorption rate measured by TDS is presented in Figure 5.1d. It can be seen that the hydrogen desorption peak is shifted from 378K (105 °C) for $(M)_H$ to 445K (172 °C) for $(MA_{500nm})_H$. Meanwhile the cumulative diffusible hydrogen content in $(MA_{500nm})_H$, e.g. 1.87 weight ppm, is significantly higher than that of $(M)_H$, e.g. 0.35 weight ppm.

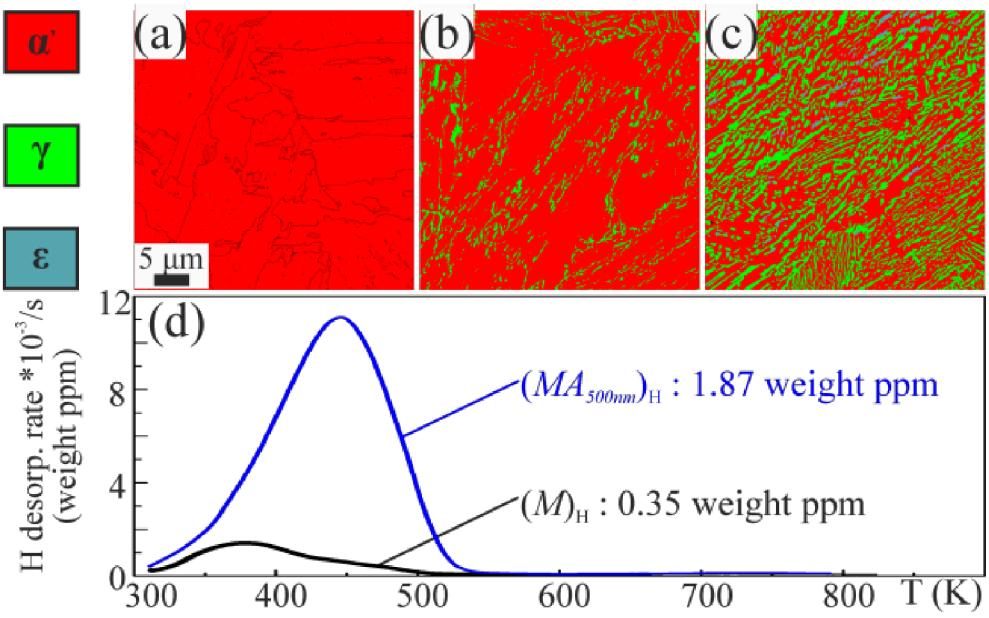

Figure 5.1: (a-c) Microstructure revealed by EBSD phase map for *M*, MA_{200nm} and MA_{500nm}. (d) Hydrogen desorption rates measured by TDS for $(M)_H$ and $(MA_{500nm})_H$. The martensitic microstructures with different γ_{RN} thicknesses are referred to as *M* (no γ_{RN}), MA_{200nm} (~200nm) and MA_{500nm} (~500nm). Corresponding microstructures with hydrogen are referred to as $(M)_H$, $(MA_{200nm})_H$ and $(MA_{500nm})_H$. Source: Image from [34], Courtesy of Springer.

The mechanical properties of samples with and without hydrogen pre-charging are presented in Figure 5.2a. First of all, the influence of the presence of hydrogen on martensite sample *M* is discussed.

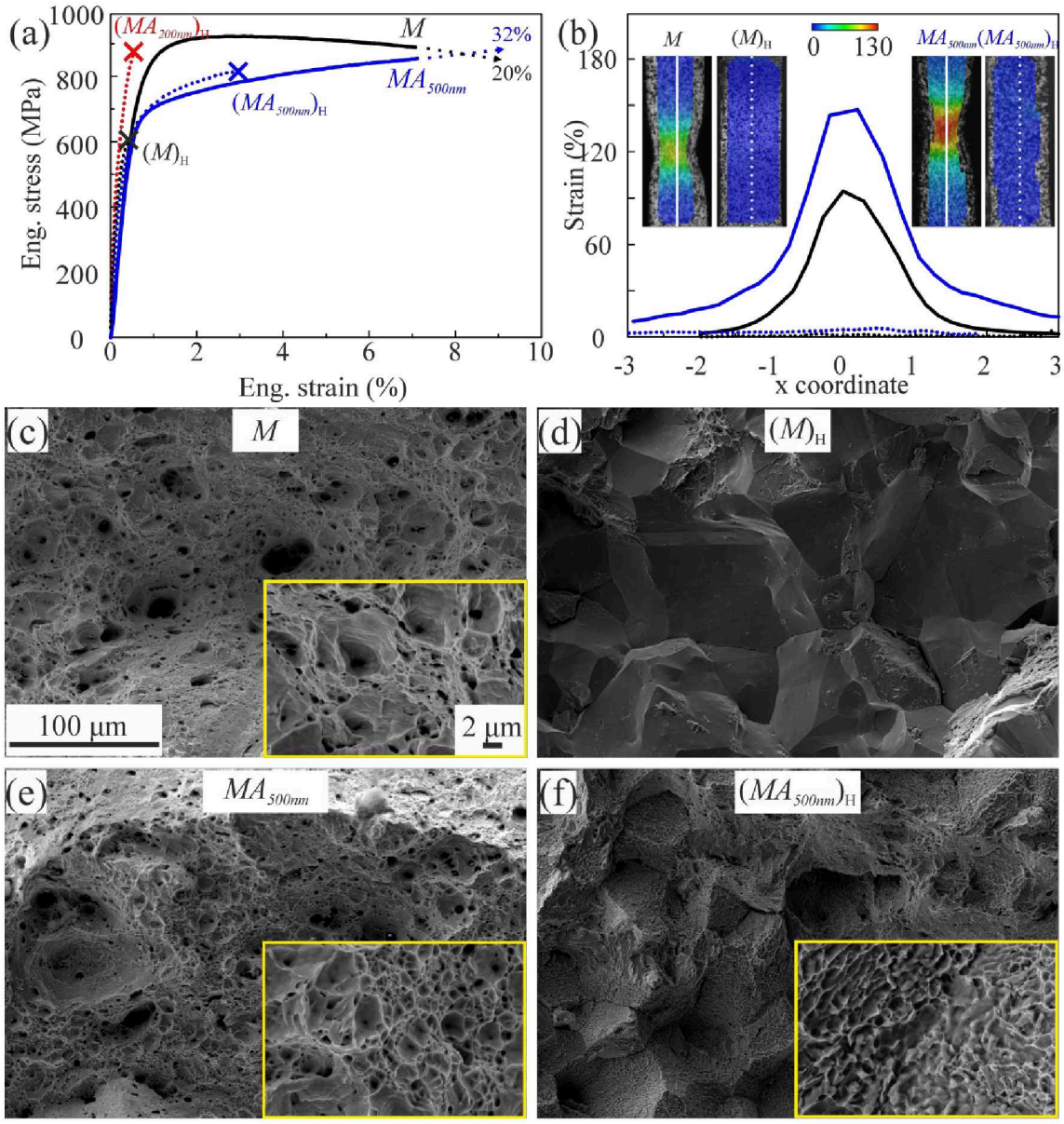

Figure 5.2: (a) Stress strain curves and (b) DIC-based local strain distributions. (c-f) Fracture surface topography for *M*, $(M)_H$, MA_{500nm} and $(MA_{500nm})_H$. Cross markers in (a) indicate the point of fracture. For *M* and MA_{500nm}, dashed arrows point to fracture elongation of 20% and 32%, respectively. The martensitic microstructures with different γ_{RN} thicknesses are referred to as *M* (no γ_{RN}), MA_{200nm} (~200nm) and MA_{500nm} (~500nm). Corresponding microstructures with hydrogen are referred to as $(M)_H$, $(MA_{200nm})_H$ and $(MA_{500nm})_H$. Source: Image from [34], Courtesy of Springer.

Without the presence of hydrogen, martensite sample *M* exhibits a yield strength $\sigma_{0.2}$ of 800 MPa, UTS of 925 MPa and uniform elongation of 2.4%, as demonstrated by the black full curve in Figure 5.2a. After hydrogen pre-charging, martensite sample $(M)_H$ fails within the elastic deformation region, as shown by the black dashed curve in Figure 5.2a. The catastrophic HE for

$(M)_H$ is confirmed by two phenomena: (i) the presence of hydrogen transits the local strain distributions at failure from black full curve to black dashed curve in Figure 5.2b; and (ii) the fracture surface changes from dimpled ductile morphology in Figure 5.2c to fully brittle morphology in Figure 5.2d. As shown by BSE images and EBSD IPF maps of the cross section of fractured $(M)_H$, the hydrogen-induced macroscopic cracks consist of both intergranular sections along prior austenite grain boundaries and transgranular sections across martensite boundaries (Figure 5.3a_1-a_3).

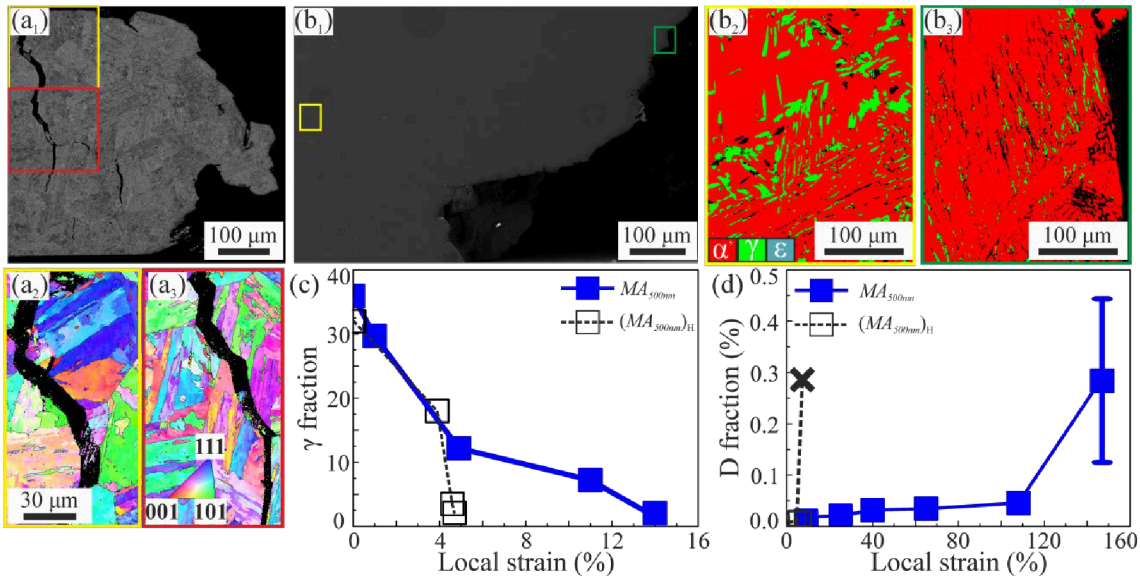

Figure 5.3: Cross section of fractured $(M)_H$ revealed by (a_1) BSE imaging; (a_2, a_3) EBSD inverse pole figure map (IPF). Cross section of fractured $(MA_{500nm})_H$ shown by (b_1) SE imaging; (b_2, b_3) EBSD phase map. (c) Austenite fraction and (d) damage evolution during deformation in MA_{500nm} and $(MA_{500nm})_H$. The invisible error bars in Figure 5.3d are smaller than the size of the data points. The martensitic microstructures with different γ_{RN} thicknesses are referred to as M (no γ_{RN}) and MA_{500nm} (~500nm). Corresponding microstructures with hydrogen are referred to as $(M)_H$ and $(MA_{500nm})_H$. Source: Image from [34], Courtesy of Springer.

Next, the influence of introducing γ_{RN} nano-films on the resistance of martensite sample $(M)_H$ to HE is examined. Similar to martensite sample $(M)_H$, martensite-reverted austenite sample $(MA_{200nm})_H$ exhibits a premature failure within the elastic deformation region, as shown by the red dashed line in Figure 5.2a. Another martensite-reverted austenite sample $(MA_{500nm})_H$, however,

fails with a strain to failure of 3.8% (blue dashed line in Figure 5.2a), which corresponds to a 4-fold increase comparing with martensite sample $(M)_H$. The enhanced resistance of sample $(MA_{500nm})_H$ to HE is consistent with the global intergranular fracture surface with in-grain fine scale ductile features, indicating plastic deformation of the microstructure prior to fracture (Figure 5.2f). Since the susceptibility of high strength steels to HE is sensitively strength-dependent, it might be argued that the increased resistance of $(MA_{500nm})_H$ to HE is a result of decreased yield strength [111]. However, two additional aspects should be considered here: (i) martensite sample $(M)_H$ fails within elastic region, where the maximum achieved stress is lower than the yield stress of sample $(MA_{500nm})_H$; (ii) in multiphase steels, e.g., TRIP-assisted multiphase steels, the stress partitioned to constitutive phase should be considered. More specific, a lower global yield stress $\sigma_{0.2}$ in $(MA_{500nm})_H$ doesn't necessarily mean that the stress partitioned to martensite in sample $(MA_{500nm})_H$, i.e. the 'hard' phase, is significantly lower than that of martensite in sample $(M)_H$. In this context, as a result of the existence of 'soft' phase γ_{RN}, the stress partitioned to martensite in sample $(MA_{500nm})_H$ is comparable to that of martensite in sample $(M)_H$ during the whole deformation process. Therefore, the effect of lower yield stress on the enhanced resistance of sample $(MA_{500nm})_H$ to HE is considered to be trivial. Thus, it can be concluded that the introduction of γ_{RN} to martensite steels has a positive effect on enhancing resistance to HE.

Despite the observed enhancement in resistance to HE, control experiments of sample MA_{500nm} without presence of hydrogen exhibit a uniform elongation of 17.2% (Figure 5.2a), considerable post-necking deformation behavior (Figure 5.2b) and a ductile fracture surface with dimples (Figure 5.2e). Thus, under the presence of hydrogen only a limited fraction of the deformation capacity is explored in sample $(MA_{500nm})_H$ (Figure 5.2a). As shown in Chapter 4, sample MA_{500nm} (referred to as sample S_{8h} in Chapter 4) demonstrates a high damage resistance due to two γ_{RN}-

related phenomena, i.e., (i) the transformation of γ_{RN} upon deformation and (ii) the extensive deflection of cracks arising from high interface density of the nanolaminate martensite-austenite morphology (Figure 5.1c). In this context, the degradation of ductility in the presence of hydrogen in sample $(MA_{500nm})_H$, e.g. 1.87 weight ppm, demonstrates significant room for further improvement. To unravel the underlying hydrogen effects, the deformed microstructure of sample $(MA_{500nm})_H$ is characterized by SE imaging and EBSD in Figure 5.3b_1-b_3.

For sample $(MA_{500nm})_H$, no macroscopic cracks can be found in the neighboring region of fracture surface, which is in contrast to sample $(M)_H$ (Figure 5.3a_1). With deforming to ~4% local strain, e.g. in the area highlighted by yellow, no micro-size damage incidents are observed and ~18% γ_{RN} grains are still present in the microstructure (Figure 5.3b_1, b_2). In fact, damage incidents and accelerated transformation of γ_{RN} (with only ~2% γ_{RN} remaining in the microstructure) can only be observed in area close to the fracture zone, e.g. as highlighted by green (Figure 5.3b_1, b_3). This strongly localized failure process in sample $(MA_{500nm})_H$ is significantly different from that of sample MA_{500nm} without presence of hydrogen. Sample MA_{500nm} demonstrates gradual phase transformation and damage evolution behaviors with straining, as discussed in detail in Chapter 4 and quantitatively plotted again for comparison (Figure 5.3c and d). Thus, although the introduction of γ_{RN} in the martensite microstructure leads to enhanced resistance to HE, a fully de-localization process by activating effective hardening and/or damage arresting micro-mechanisms in the martensite-austenite microstructure is hindered. To obtain in-depth understanding of the underlying damage evolution processes, the longitudinal cross section of fractured sample $(MA_{500nm})_H$ is examined by ECCI and EBSD (Figure 5.4).

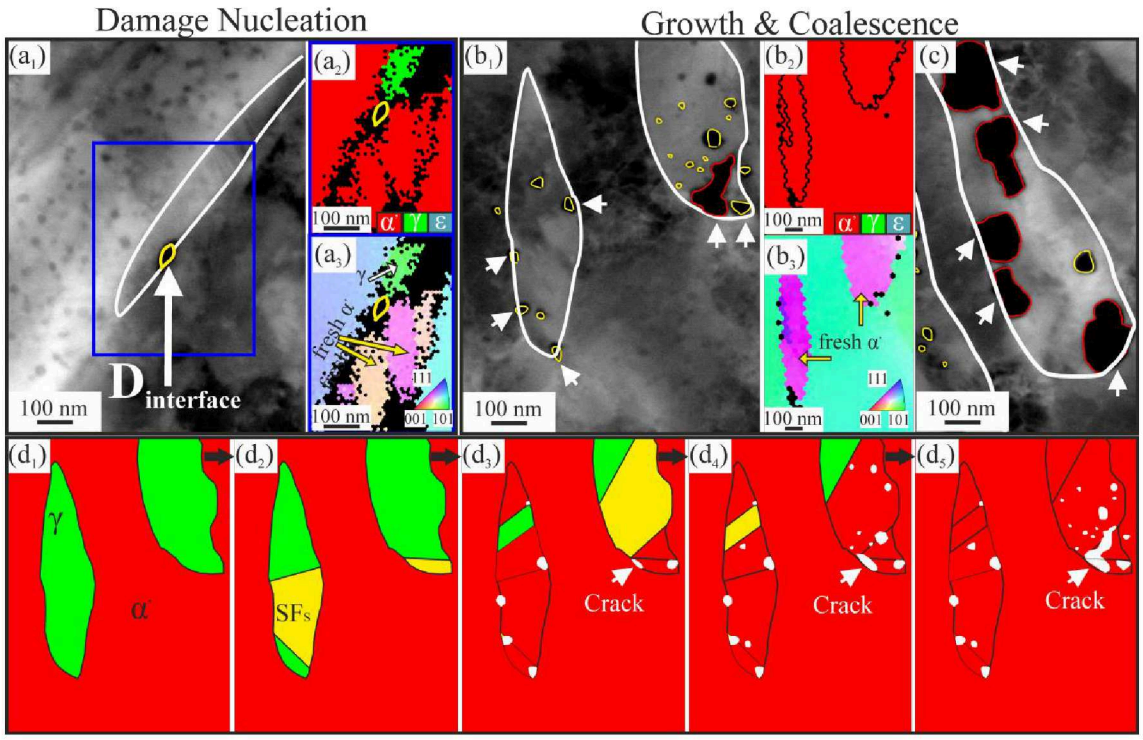

Figure 5.4:(a_1-a_3, b_1-b_3, c) Damage nucleation, growth and coalescence process in $(MA_{500nm})_H$, as unraveled by ECCI and EBSD measurements. (d_1-d_5) Schematical sketch of this process. After hydrogen pre-charging, the martensitic microstructure with γ_{RN} thicknesses of ~500nm is referred to as $(MA_{500nm})_H$. Source: Image from [34], Courtesy of Springer.

In the ECCI images in Figure 5.4, α' martensite matrix is characterized by formation of particles and γ_{RN} grains (highlighted by white outlines) are free of precipitates. As discussed in Chapter 4 and Chapter 7, γ_{RN} accommodates deformation by activating multiple mechanisms, including formation of SFs, mechanical twinning and phase transformation in absence of hydrogen. In the presence of diffusible hydrogen, two kinds of damage nucleation sites were observed, which are located (i) within the bulk of deformation-induced martensite and (ii) along interface of deformation-induced martensite and matrix martensite (referred to as $D_{interface}$ in Figure 5.4a_1). The EBSD phase map demonstrates the nucleation of an interfacial crack along martensite boundaries (Figure 5.4a_2). The two α' martensite islands on the right side of the interfacial crack (highlighted by yellow arrows in Figure 5.4a_3) were observed to exhibit different crystallographic

orientations from the matrix martensite. Combing the morphology of the grains and their different crystallographic orientations, these two α' martensite islands are deformation-induced martensite. Thus, the interfacial crack is located along interface of matrix martensite and deformation-induced martensite.

With increasing strain, it is observed that the damage area fraction increases rapidly (Figure 5.4b_1). The EBSD phase map of this area demonstrates that the microstructure is composed of only α' martensite phase (Figure 5.4b_2). And the different crystallographic orientations and the morphology of the two highlighted grains indicate that they are deformation-induced martensite (Figure 5.4b_3). To clearly distinguish from damages within bulk of deformation-induced martensite, damages along deformation-induced martensite/matrix martensite interface are marked with white arrows, as shown in Figure 5.4b_1 and Figure 5.4c. To further clarify the damages dominating the growth and coalescence processes, the damage incidents larger than average damage sizes are highlighted by red outlines in Figure 5.4b_1 and Figure 5.4c. Although both damage nucleation sites are observed to be active, a distinct growth process is observed. While cracks along interfaces grow significantly larger in size, voids within bulk of deformation-induced martensite are smaller in size and stay isolated from each other (Figure 5.4). Thus, it can be concluded that interfacial damages dominate the growth and coalescence processes.

Based on these observations, it is possible to conceive a physical description of the damage process in martensite-reverted austenite sample $(MA_{500nm})_H$. A schematical sketch of the damage nucleation, growth and coalescence process in $(MA_{500nm})_H$, as reconstructed from the region in Figure 5.4b_1, is presented in Figure 5.4d_1-d_5.This schematical sketch will be referred to in the following discussion.

In martensite sample $(M)_H$, the presence of hydrogen promotes both intergranular fracture, e.g. crack propagation along prior austenite grain boundaries, and transgranular fracture, e.g. crack propagation along martensite boundaries (Figure 5.3a_1-a_3, Figure 5.2d) [112], [113]. In sample $(MA_{500nm})_H$, plastic strain is preferentially accommodated by γ_{RN} phase (Figure 5.4d_1), via initially formation of SFs (Figure 5.4d_2), and then transformation into martensite (Figure 5.4d_3). Despite of the martensitic matrix and the higher overall diffusible hydrogen content[4], $(MA_{500nm})_H$ can be plastically deformed with a strain to failure of 3.8% through the activation of these mechanisms, rather than undergoing brittle failure as sample $(M)_H$ (Figure 5.2a). However, as a result of the early micro-crack nucleation within deformation-induced martensite and along the interface of matrix martensite and deformation-induced martensite, further ductilizing benefit from the introduction of γ_{RN} phase is hampered (Figure 5.4d_3). In sample $(MA_{500nm})_H$, it is expected that a heterogeneous distribution of hydrogen exists in microstructural constitutes due to the difference in diffusivity and solubility of hydrogen in α' martensite (bcc structure, high diffusivity and low solubility) and γ_{RN} (fcc structure, low diffusivity and high solubility). Despite tempering at 600 °C for 8 h, a significant amount of dislocations can still be observed in the martensitic matrix in sample MA_{500nm} (Figure 3.6c) due to the fact that particles can be uniformly precipitated in the matrix and restrict the degree of dislocation annihilations [16]. In addition to dislocations inside the martensite, the existence of additional trapping sites by precipitates further increase the amount of trapped hydrogen in sample $(MA_{500nm})_H$ [114], [115]. For short time hydrogen pre-charging scenarios, Chan et al. reported that α' martensite /γ phase interfaces act as preferential hydrogen trapping sites [116]. Szost et al. also reported that in carbide-free nanostructured bainite, coherent ferrite/γ interfaces act as reversible hydrogen trapping sites [107]. Bearing these in mind,

[4] Under the same charging condition, more diffusible hydrogen (1.87 weight ppm) is trapped in $(MA_{500nm})_H$ (Figure 5.1d).

it is proposed that both (i) within bulk of deformation-induced martensite, e.g. by considering the inherited heterogeneity of hydrogen distribution and the accumulated defect density in the microstructure upon martensitic transformation [27], [109], [117], and (ii) the interfaces between matrix martensite and deformation-induced martensite, i.e. main hydrogen trapping sites, act as damage nucleation sites. The latter damage site, as a result of its significant amount of trapped hydrogen, becomes significantly susceptible to further growth and coalescence process. With increasing straining, the developing stress field in the neighborhood promotes further phase transformations of the nearby γ_{RN} grains (Figure 5.4d_4). Through the repetition of this mechanism new cracks are continuously initiated, as the initial cracks simultaneously grow (Figure 5.4d_5) and all eventually coalesce along the interfaces. This whole process is most clearly represented for the cracks indicated by white arrows (Figure 5.4d_3-d_5). In the end, fracture takes place by the decohesion of the phase interface, which is further confirmed by revisiting the fracture surface in Figure 5.2f. Here the concave and convex features are not typical cup-cone dimples, but rather demonstrate the morphology of delaminated matrix martensite and deformation-induced martensite. This cyclic sequence of phase transformation and crack nucleation takes place in an uncontrolled manner, leading to the eventual premature macroscopic failure.

In summary, the influence of introducing γ_{RN} in increasing resistance of the martensitic microstructures to HE is investigated in Chapter 5. This strategy is proven to be effective, leading to improvements in strain to failure corresponding to 4-fold increase. However, further strain delocalization benefit from γ_{RN} is hampered due to the early micro-crack nucleation, growth and coalescence at the interface of matrix martensite and deformation-induced martensite. And the resulting stress field in the neighborhood subsequently promotes phase transformation of neighboring γ_{RN} grains. Thus, when all γ_{RN} grains exhibit similar mechanical stability, the resulting avalanche of deformation-induced martensitic transformations can cause a chain HE

process through further initiating more cracks, as the initial cracks simultaneously grow. This is also confirmed by the observation that sample $(MA_{200nm})_{H}$, with its reduced γ_{RN} stability (Chapter 7), exhibits lower ductility than $(MA_{500nm})_{H}$ when pre-charged with hydrogen under the same charging condition. Thus, one possible strategy for further improving the resistance of lath martensitic steels to HE lies in designing γ_{RN} grains with widely-dispersed mechanical stability, e.g. via adjusting austenite grain size, chemical composition or orientations.

Chapter 6 Restorations of microstructure and mechanical properties via cyclic austenite reversion

6.1 Introduction

Metallic materials lose their plastic deformation capacity rapidly as they are deformed, even under stresses below their yield stress, due to the accumulation of microstructural defects. In industrial practice, non-destructive testing techniques are typically employed to determine when the density of accumulated defects surpasses a critical threshold, and when the component is required to be replaced to avoid catastrophic failure.

This costly process could in principle be delayed by autonomic healing of the accumulated defect density, i.e. assuming that intrinsic self-healing mechanisms could be introduced during microstructure design. However, despite significant research efforts, the emerging field of self-healing materials is still dominated by polymers [118]–[120] and ceramics [121]–[125]. For metallic materials, which suffer from the relative sluggishness of chemical processes at ambient temperatures, only partial success specific to surface defects has been demonstrated [126], [127]. Recent theoretical analysis suggest that mobile interfaces of idealized character can sweep close bulk nano-cracks as well, although there is yet no experimental verification of this mechanism [128]. Thus, both of these examples clarify the challenging demand to design very specific microstructures capable of autonomic healing. Even in cases of success, application regimes of successful crack closure is unknown and overall property improvements compared to non-healing state-of-the-art alternative alloys, is not clear.

An alternative strategy to "rewind" (rather than extend) the component lifetime, would be the application of a post-deformation annealing treatment to recover the original defect density. Present few examples following this non-autonomic healing approach successfully demonstrate the decrease of pore density by preferential precipitation during aging in specifically designed

model microstructures [129]–[131], although restoration of mechanical properties is not yet confirmed.

Here in Chapter 6, it is proposed that such non-autonomic healing approaches can be extended to a wide variety of multi-phase steels, if certain microstructure design criteria are to be employed. The steels that fulfill these criteria are referred to as "healable steels". In what follows, to clarify these points, the criteria for healable microstructure design are proposed first. To achieve this, it is essential to understand the annealing behavior of backbone phases in structural steels after deformation, e.g. ferrite, martensite and austenite. Each phase will be addressed individually in the following.

As a ‘soft’ phase, ferrite loses its deformability during deformation as a result of accumulated dislocation density. Elimination of dislocation density in ferrite can be achieved via recovery and recrystallization during annealing at ferritic or intercritical (ferrite+austenite) or austenitic region, depending on degree of deformation and annealing conditions, etc. [132]–[135].

As a ‘hard’ phase, martensite softens due to annihilation of dislocations during tempering [136], [137], unless in maraging steels [138]–[140]. Maraging steels exhibit hardness increase due to precipitation hardening during early stage of aging and then reach maximum hardness with increasing annealing time [48], [141]. Even in case of overaging, the hardness of martensite decreases, but usually is still higher than that of the initial martensite [48], [141].

As a ‘soft and ductile’ phase, metastable austenite can transform into hard martensite in the deformation process, depending on their mechanical stability [142], [143]. During subsequent annealing, deformation-induced martensite can be reverted to austenite without assistance of long range diffusion, e.g. in metastable austenitic stainless steel [143]–[145]. As a matter of fact, phase reversion of heavily deformed metastable austenite is a recently proposed novel approach to produce nano-grained/ultrafine-grained metastable austenitic stainless steels [145]. This approach

can be realized with short time duration at temperature higher than austenite start temperature (A_s) when the transformation of deformation-induced martensite to austenite proceeds via a shear/diffusionless mechanism [145], [146]. In the case of austenite reversion in martensitic steels, e.g. medium Mn martensitic steels, austenite formation without assistance of long range diffusion can also be realized with high heating rate [147]. In this case, however, the reverted austenite might possess insufficient thermal stability due to inadequate partitioning of austenite stabilizing elements into austenite, e.g. Mn or C, e.g. if the isothermal holding time is too short [147].

Bearing the post-deformation annealing behaviors of these three backbone phases in mind, criteria (i-iii) for realizing non-autonomic healing are proposed.

(i) Controlling (and healing) critical defects: In majority of high strength steels with multi-phase microstructures, it is mainly the consumption of the strain hardening capacity, rather than crack evolution, which leads to localization and failure [89], [90], [148]. This suggests that the ideal microstructure should restore its deformation ability upon the heating treatment rather than initiating mechanisms to 'repair' initiated cracks. This perspective leads to a concept against earlier investigations on self-healing mechanism in metallic materials, which focuses on physically closing or filling nucleated cracks [129], [131]. *More specifically, this means that the accumulated dislocation density in the soft phases (e.g. ferrite, austenite), i.e. phases dominantly partition strain during deformation, should be easily recovered by low/moderate temperature annealing.*

(ii) Applying feasible treatments: In principle, even severely and heterogeneously deformed microstructures can be restored upon application of an aggressive thermal [149] or thermo-

mechanical treatment[5] [150], [151]. However, such costly approaches are clearly not practical, and the ideal non-autonomic healing microstructure should have the capability to be restored *via* a feasible (short-duration and low temperature) treatment. *More specifically, this requires that the involved recovery/recrystallization, phase transformations or precipitation reactions should take place without assistance of long-range diffusion by low/moderate temperature annealing.*

(iii) Recovering mechanical properties: While low temperature annealing treatments do lead to the recovery of strain hardening capacity of the soft phase in conventional high strength steels, hard phases are also simultaneously softened. In a simple dual phase steel (DP steel), for example, softening of martensite (α') due to tempering would be expected (Figure 6.1a). In a conventional TRIP-assisted steel, accompanying the recovery of deformed ferrite (α) many competing processes are conceivable, e.g. martensite (α') to austenite (γ) phase transformation and precipitation of carbides (c) in austenite (Figure 6.1b). The depletion of carbon from austenite due to carbide formation can lead to inadequate austenite thermal stability and also decreased austenite fraction (Figure 6.1b). *In the ideal microstructure, possible strength loss of the harder phase (e.g. α' martensite) during annealing should be compensated by strengthening from fine distributed intermetallic particles (P) and avoid undesired phases* (Figure 6.1c).

[5] In the extreme case, casting porosities of the engineering scale are also 'healed' upon simple forging or rolling treatments.

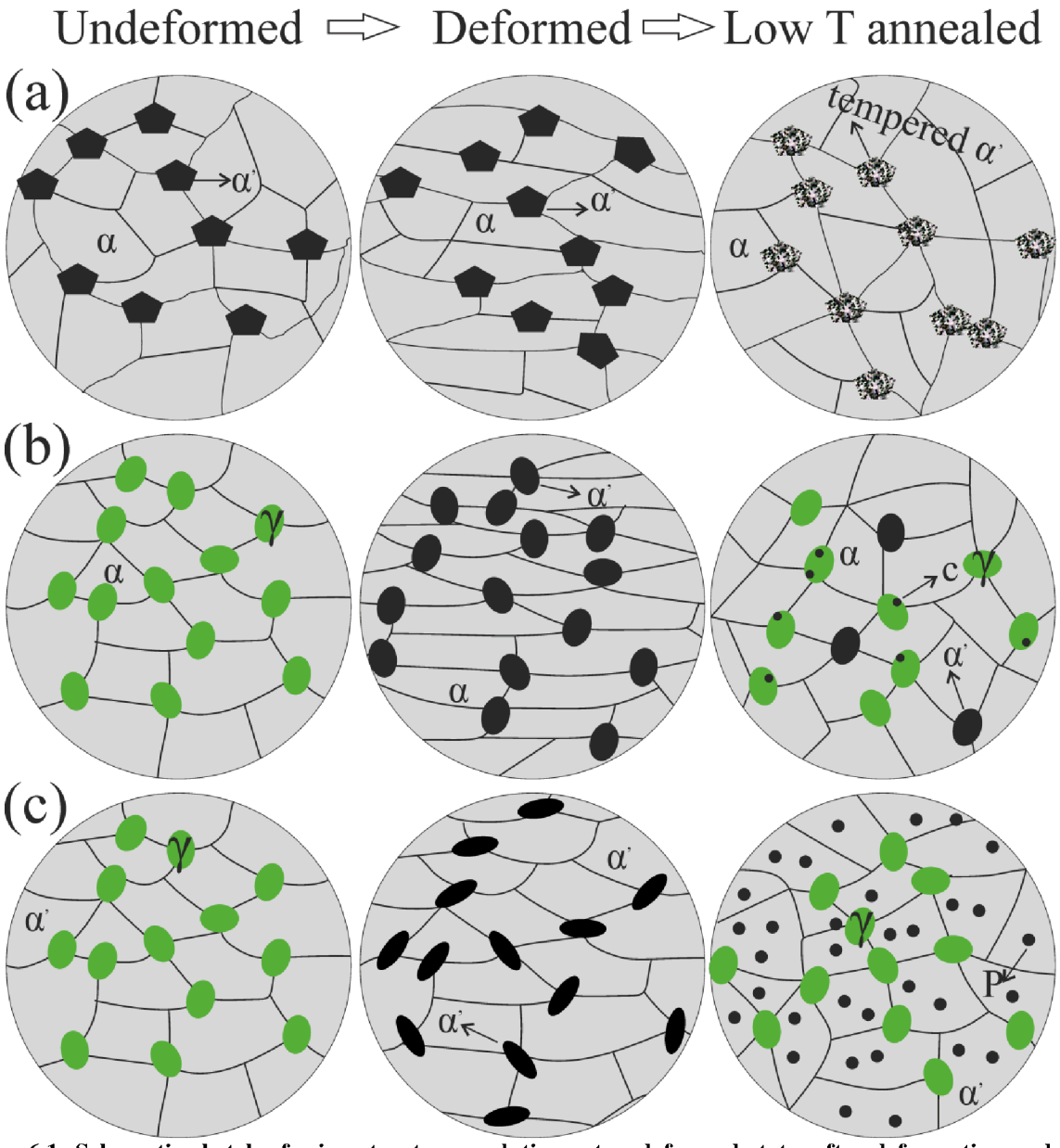

Figure 6.1: Schematic sketch of microstructure evolutions at undeformed state, after deformation and after post-deformation low temperature annealing for (a) DP steels; (b) TRIP-assisted multiphase steels; (c) an ideal steel. Interpretation of symbols: α: ferrite; α': martensite; γ: austenite; c: carbides; p: intermetallic particles.

In this context, the duplex nano-laminate reverted austenite-martensite steel is expected to fulfill the non-autonomic healing criteria. On one hand, strength loss of 'hard' phase martensite during post-deformation annealing can be avoided or compensated due to the precipitation hardening. On the other hand, deformation-induced martensite will inherit the chemical composition of the

reverted austenite during deformation. Thus, if reversion of deformation-induced martensite to austenite can be triggered during post-deformation annealing, no additional elemental partitioning between matrix martensite and reverted austenite is required.

Therefore, in this chapter, to validate the proposed criteria, the possibility of simultaneous restorations of microstructure and mechanical properties by post-deformation annealing of the current TRIP-maraging steel is examined. First, the detailed structures of microstructure constitutes at three states, namely prior to deformation, after well-defined deformation level and after post-deformation annealing are characterized. Then the mechanical properties of original and healed state are tested and compared. The results successfully demonstrate retrieve of both microstructure and mechanical properties with a post-deformation annealing treatment, thus the current TRIP-maraging steel delivers itself as non-autonomic healable steel.

6.2 Experimental procedure

After reversion treatment (8 h, 600 °C) of the current TRIP-maraging steel, cylinder tensile samples were cut along rolling direction of steel plate. Samples at this state are named as virgin samples (S_V). To avoid initiation of cracks, e.g. following defined critical defects by criterion (i), samples were tensile tested and interrupted before necking took place. To apply non-autonomic healing (criterion (ii)), these deformed samples were annealed at 600 °C for 8 h. Samples after post-deformation annealing are referred to as healed samples (S_H). Healed samples were subjected to tensile testing again. Here, 1st time, and 2nd time healed samples are named as S_{H1} and S_{H2}, respectively. Microstructures of S_V and S_H were characterized by SEM-based EBSD, EDX and ECCI, and XRD.

6.3 Results and Discussion

Prior to deformation, the microstructure of virgin sample S_V consists of α' martensite (phase in red), nanoscale reverted austenite γ_{RN} (phase in green) and a small fraction (~3%) of ε martensite (phase in blue) (Figure 6.2a_1). As revealed by the SEM-EDX map, γ_{RN} grains are enriched with Mn and depleted with Al. No obvious partition of Ni between α' martensite and γ_{RN} is detected by SEM-EDX.

The complete stress strain curve of cylinder virgin sample S_V is shown in Figure 6.3a, which exhibits yield stress $\sigma_{0.2}$ of 785 MPa, UTS of 920 MPa and uniform elongation of 9.6% (blue curve). Thus, according to criterion (i), tensile testing should be interrupted before straining to 9.6%, i.e. to avoid necking and strain localization. Then another virgin sample S_V was tensile tested and interrupted at strain of 9.5% (red curve in Figure 6.3a). As measured by EBSD, only ~5% γ_{RN} grains are still present in 9.5% deformed S_V, implying the transformation of ~30% γ_{RN} grains to α' martensite during the uniform deformation regime (Figure 6.2a_1). The same transformation behavior is also measured by XRD, e.g. probed from bulk volume, as demonstrated by the nearly diminishment of γ_{RN} peaks and increased peak intensity of α' martensite of S_V during deformation (transition from red to green curve in Figure 6.2b). Meanwhile, peak width of α' martensite broadens with deformation, indicating simultaneous increasing of dislocation density in α' martensite [64]. The increasing of dislocation density in α' martensite during deformation of sample S_V is quantified according to the method described by Gutierrez et al. [152], as based on optimized ECCI images (Figure 6.4a_1-a_2). The dislocation density ρ in α' martensite increases from $17.06\pm3.69\times10^{15}$ m^{-2} in S_V to $24.46\pm8.91\times10^{15}$ m^{-2} after 9.5% straining of sample S_V.

Then 9.5% deformed S_V was annealed at 600 °C for 8 h, i.e. by duplicating the annealing treatment of as-quenched martensite to obtain virgin sample S_V. The microstructure of 1st healed sample S_{H1} is shown in Figure 6.2a$_3$. Surprisingly, the microstructure of sample S_{H1} is almost identical to virgin sample S_V in terms of morphology and distribution of all phases, phase fraction (~36% γ_{RN} in S_{H1}) and elemental distribution. The restoration of the microstructure is also confirmed by XRD measurement (comparing blue curve for S_{H1} with red curve for S_V in Figure 6.2b). The dislocation density ρ of α' martensite in sample S_{H1} is calculated as $17.44\pm3.55\times10^{15}$ m^{-2}, based on ECCI images (Figure 6.4b$_1$). Meanwhile particles in α' martensite coarsen only slightly, e.g. from 356±117 nm^2 in S_V to 430±187 nm^2 in S_{H1}. To summarize, after post-deformation annealing, healed sample S_{H1} restores original microstructure as in virgin sample S_V.

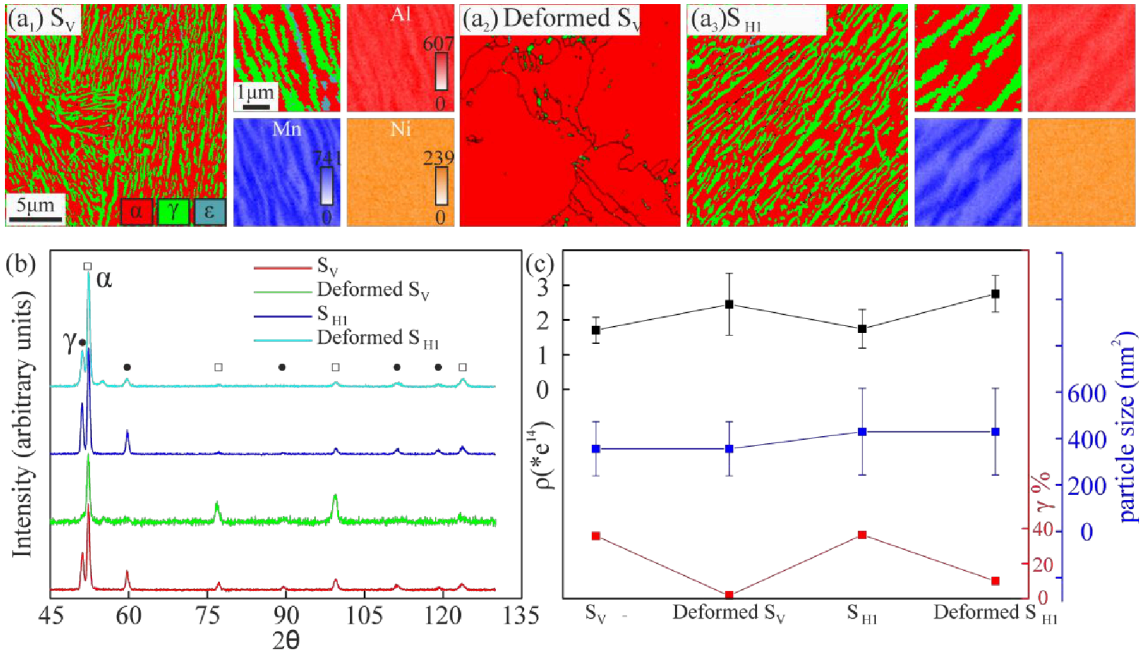

Figure 6.2: Microstructure of (a_1) virgin sample S_V; (a_2) 9.5% deformed S_V; (a_3) 1st healed sample S_{H1}, as characterization by EBSD and EDX. (b) XRD measurements for S_V, 9.5% deformed S_V, S_{H1} and 9.5% deformed S_{H1}. (c) Comparision of dislocation density ρ in α' martensite, γ_{RN} fractions and sizes of precipites in S_V, 9.5% deformed S_V, S_{H1} and 9.5% deformed S_{H1}.

Then the mechanical property of healed sample S_{H1} is assessed by tensile test up to 9.5% strain, i.e. to avoid necking and strain localization. Surprisingly, the stress strain curve of healed sample S_{H1} almost overlaps with the virgin sample S_V (comparing black with red curves in Figure 6.3a). The sample S_{H1} exhibits a yield stress $\sigma_{0.2}$ of 780 MPa and UTS of 930 MPa, i.e. retrieving 97% of yield stress and 100% of UTS in S_V. Thus, healed sample S_{H1} retrieves both the microstructure and mechanical property after the post-deformation annealing, i.e. non-autonomic healing is successfully achieved.

To validate the feasibility of further non-autonomic healing process, post-deformation annealing of deformed S_{H1} was conducted and then 2^{nd} time healed sample S_{H2} was tensile tested to fracture (green curve in Figure 6.3a). The sample S_{H2} exhibits a yield stress of 775 MPa and UTS of 940 MPa, i.e. retrieving 96% of yield stress and 100% of UTS in S_V. The true stress strain curves and strain hardening curves for all samples are shown in Figure 6.3b. The mechanical properties in terms of yield stress $\sigma_{0.2}$, UTS and uniform elongation for virgin sample S_V, 1^{st} time healed sample S_{H1}, 2nd time healed sample S_{H1} and another virgin sample S_{8h} are summarized in Figure 6.3c.

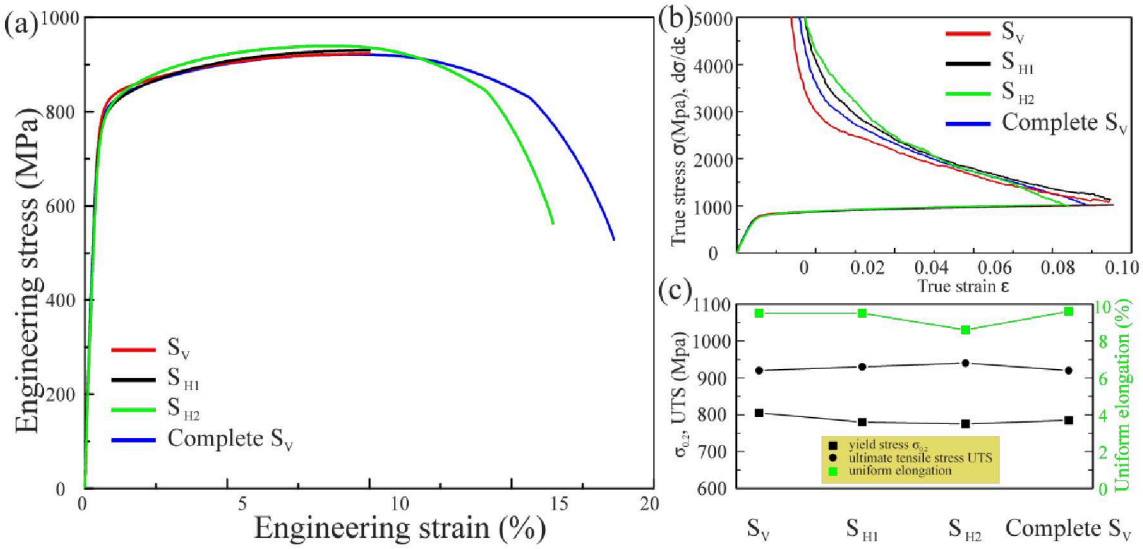

Figure 6.3: (a) Engineering stress-strain curves; (b) true stress strain curves and strain hardening curves; (c) mechanical property summary for virgin sample S_V, 1st time healed sample S_{H1}, 2nd time healed sample S_{H2} and another virgin sample S_V.

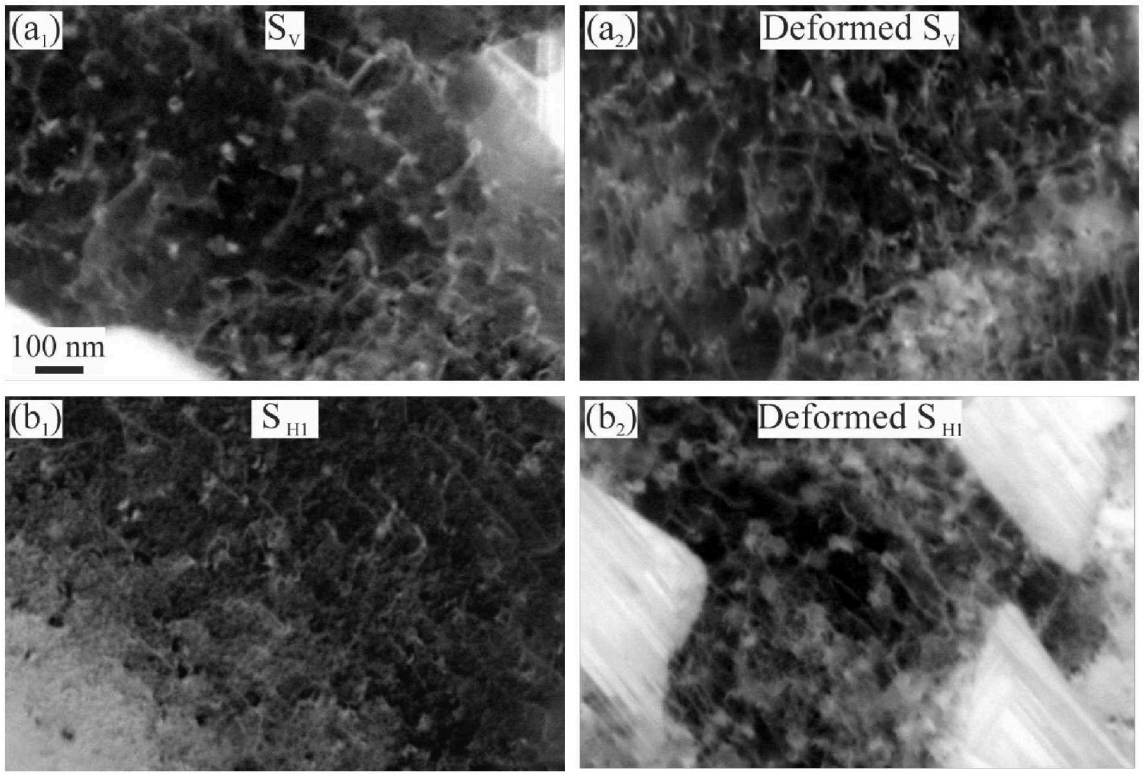

Figure 6.4: Evolution of detailed structures in α' martensite for virgin sample S_V at (a_1) undeformed state; (a_2) after uniform deformation; 1st time healed sample S_{H1} at (b_1) undeformed state; (b_2) after uniform deformation, as characterized by ECCI.

Thus, the current TRIP-maraging steel demonstrates itself as a successful case study of non-autonomic healing steel. This steel is capable of retrieving its original microstructure and mechanical property with the assistance of a post-deformation annealing treatment.

The microstructure of virgin sample S_V consists of α' martensite, γ_{RN} and ε martensite phases (Figure 6.1a). γ_{RN} exhibits enrichment of Mn and depletion of Al, e.g. in accordance with the elemental partitioning behavior during partial reversion of as-quenched martensite (Figure 7.1). The deformation in S_V is proceeded in γ_{RN} via formation of SFs, mechanical twinning (Chapter 4) and phase transformation (Figure 6.1), and in α' martensite through multiplication of dislocations (Figure 6.4). Due to the diffusionless character of mechanical induced phase transformation, the deformation-induced α' martensite also inherits the chemical composition of γ_{RN}. Since the post-deformation annealing temperature is also 600 °C, the γ_{RN} will also assume the same chemical composition in S_{H1} as in S_V (Figure 7.1, Figure 6.2a_3). Thus, the inherited chemical composition in deformation-induced martensite in deformed S_V would thermodynamically favor the formation of γ_{RN} in S_{H1} without assistance of long-range diffusion, e.g. γ_{RN} will be formed in the area possessed by deformation-induced martensite (Figure 6.2a_3). At the same time, the increased dislocation density ρ of α' martensite in 9.5% deformed S_V ($24.46\pm8.91\times10^{15}$ m^{-2}) is effectively decreased to $17.44\pm3.55\times10^{15}$ m^{-2} in S_{H1}, indicating a well retrieved defect structure in α' martensite by non-autonomic healing. Meanwhile, although the particles coarsen from 356±117 nm^2 in S_V to 430±187 nm^2 in S_{H1}, 97% of yield stress $\sigma_{0.2}$ is successfully retrieved (Figure 6.3).

Thus, following the proposed three criteria, first tensile test without initiating strain localization was applied (criterion (i)), then a feasible post-deformation heat treatment was conducted (600 °C 8 h) (criterion (ii)), and the individual constitute restores its initial defect structure (criterion (iii)). With the restored microstructure, the mechanical property is eventually retrieved, rendering the

current TRIP-maraging steel as the first case study of non-autonomic healing steel. When this kind of non-autonomic healing steels is subjected to other loading conditions, e.g. rolling, fatigue test, retrieving original microstructure and mechanical property after appropriate post-deformation annealing is also expected, thus promoting prolonged (or even infinite) service time.

Chapter 7 Smaller is less stable: Size effects on twinning vs. transformation of reverted austenite in TRIP-maraging steels [6]

7.1 Introduction

Besides a few works [153]–[155], the majority of the reports on the mechanical stability of metastable austenite focus on grains size regimes larger than nanoscale, e.g. >~200 nm in previous works [42], [148], [156]–[159]. However, a micro-mechanical understanding of the transformation size effects within nanoscale sizes, e.g. the one present in the TRIP-maraging steels, is critical for all steels containing nanoscale austenite grains, especially in providing generalized guidelines to fine-tune microstructures such that phase transformation can be activated over the entire deformation regime [160], [161].

Understanding the related microstructural factors and correspondingly control the austenite stability has remained as a key issue in the literature for designing TRIP-assisted alloys. Previous reports underline that the complexity arises due to the existence of various microstructural parameters, e.g. crystallographic orientation [162], [163], grain size [164]–[167] and chemical composition, etc. [165], [168], [169]. Additional micro-mechanical complexity of the problem is introduced due to possible strong stress shielding and strain partitioning effects due to the presence of surrounding hard phases [158], [170] which are intrinsically present in conventional multi-phase TRIP steels. The study of size effects on phase transformation of γ_{RN} grains in TRIP-maraging steels, however, overcomes these microstructural and micro-mechanical complexities.

[6] The main content of Chapter 7 is based on [35] M.-M. Wang, C. C. Tasan, D. Ponge, A. Kostka, and D. Raabe, "Smaller is less stable: Size effects on twinning vs. transformation of reverted austenite in TRIP-maraging steels," Acta Mater., vol. 79, pp. 268–281, Oct. 2014.

As will be demonstrated in detail later, this TRIP-maraging microstructure renders itself as a model microstructure for studying purely size effects independent of the aforementioned microstructural factors, and simultaneously reduces the aforementioned complex micro-mechanical problem.

In this chapter, first the design strategy of the model TRIP-maraging steel microstructure is presented. Then, the results of the *in-situ* and *post-mortem* deformation and microstructure analysis are shown, discussed, and finally the conclusions are presented.

7.2 Results

7.2.1 Model microstructure design

First, the reverse transformation of α' martensite back into γ_{RN} in the current TRIP-maraging steel (Fe-9Mn-3Ni-1.4Al-0.01C, mass %) is calculated by Dictra software using TCFE7 and MOBFe2 databases (Figure 7.1). Here, the growth of γ_{RN} and the accompanying elemental partitioning of Mn/Ni/Al/Fe between α' martensite and γ_{RN} after 1 h and 8 h annealing at 600 °C are presented. After 1 h annealing at 600 °C, γ_{RN} grows to roughly 100 nm thick and exhibits uniform chemical composition. With increasing annealing time to 8 h, γ_{RN} grains grow further without changing the chemical composition. Thus, as a guide for alloy design, to produce γ_{RN} grains with uniform composition and with size scales measureable by EBSD measurements, reversion treatments should be carried out for times longer than 1 h at 600 °C.

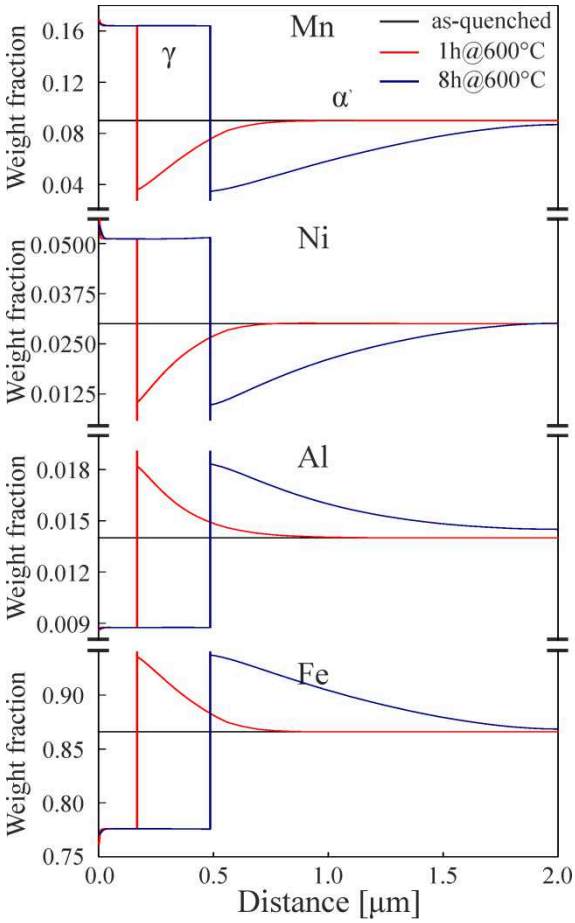

Figure 7.1: Predicted reversion of α' martensite back into γ_{RN} in the current Fe-9Mn-3Ni-1.4Al-0.01C (mass %) TRIP-maraging steel at 600 °C for 1 h and 8 h, and the corresponding elemental partition of Mn/Ni/Al/Fe, simulated by Dictra using thermodynamic database TCFE7 and mobility database MOBFE2. Source: Image from [35], Courtesy of Elsevier.

Next, the determined 600 °C annealing treatment is applied to the Fe-9Mn-3Ni-1.4Al-0.01C (mass %) alloy. Prior to the reversion treatment, the microstructure consists of a single α' martensite phase and all elements, e.g. Mn, Ni, Al, and Fe, are homogeneously distributed in the microstructure (Figure 7.2a). No retained γ phase or micro-segregation was detected within the resolution limits of HR-EBSD and EDX in SEM. After 1 h annealing at 600 °C, thin layers of γ_{RN} grains were observed along the prior γ grain boundaries and α' martensite packet/block boundaries (Figure 7.2b). After 8 h annealing, all lath martensite boundaries are also observed to be covered by γ_{RN} grains (Figure 7.2c). Comparing the resulting microstructures in Figure 7.2b and Figure 7.2c, which represent the 2D sections of the microstructures, it can be seen that the

annealing time has a direct influence on the continuity of the γ_{RN} grain network and thus also on the 3D morphology of γ_{RN} grains. The extended annealing treatment at 600 °C, e.g. after 8 h, leads to the formation of a quasi-continuous γ_{RN} network along all martensitic boundaries, leaving behind only limited gaps. In 3D, the austenite grains are nano-films that follow the complex 3D network of lath martensite boundaries [171]. The predicted uniform chemical composition of γ_{RN} grains by Dictra calculations is also experimentally confirmed, e.g. shown by SEM-EDX analysis in Figure 7.2c and TEM-EDX analysis shown as inset in Figure 7.2c_1. SEM-EDX measurements did not reveal obvious partition of Ni between α' martensite and γ_{RN} phase.

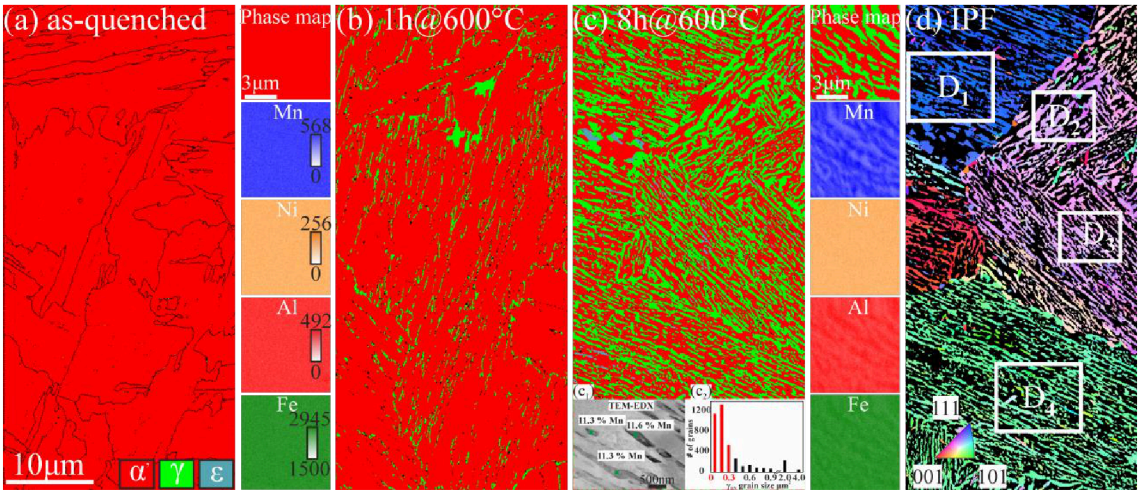

Figure 7.2: .Microstructure evolution due to the reversion treatment characterized by HR-EBSD and EDX: (a) at as-quenched state; (b) 600 °C 1 h sample; (c) 600 °C 8 h sample; (d) inverse pole figure map (IPF) of γ_{RN} grains in the same area as (c). Each EDX map is color coded by the count frequency of corresponding X-ray signal received by EDX detector. EDX measurements of γ_{RN} grains from TEM are shown as inset in Figure 7.2c_1. The area distribution of γ_{RN} grains is shown as inset in in Figure 7.2c_2. This area distribution of the undeformed state is compared in Figure 7.6a to that of different deformed states. Source: Image from [35], Courtesy of Elsevier.

Thus, the predicted microstructures consisting of martensite and γ_{RN} grains with homogeneous chemical composition are experimentally confirmed by EBSD and EDX. This point is essential in order to clearly distinguish purely size effects (such as targeted here) from otherwise composition dependent phenomena, i.e. with a situation where different austenite grains assume

heterogeneous chemical composition. As shown by the inverse pole figure (IPF) in Figure 7.2d, all γ_{RN} grains formed within one α' martensite block, e.g. highlighted regions D_1, D_2 and D_4, exhibit the same crystallographic orientation (~1° misorientations). Hence, through the application of a simple heat treatment (600 ^{o}C, 8 h), a model microstructure for studying size effects on mechanical stability, independent of crystallographic orientation, chemical composition, geometric orientation, and influence of second phase is achieved[7]. Thus, all the following mechanical tests in this chapter were carried out on 600 °C 8h sample with the optimized γ_{RN} grain size.

7.2.2 Deformation-induced microstructure evolution

Figure 7.3 shows the phase fraction evolution of γ_{RN} (green data points) and ε-martensite (blue data points) during the tensile tests as measured by *in-situ* (square) and *post-mortem* (triangle) EBSD measurements. The EBSD phase maps obtained from these measurements are exhibited in Figure 7.4. As schematically shown in the inset, the *in-situ* measurements are carried out on the surface of a deforming sample, while the *post-mortem* measurements are conducted within the bulk of a deformed sample. The EBSD measurements exhibits good correspondence with the XRD measurements, as carried out both at the undeformed state (XRD, green cross data point) and at the severely deformed state (SXRD, green plus data point). Both independent data sets obtained from *in-situ* (i.e. surface) and *post-mortem* (i.e. bulk) EBSD analysis reveal that a continuous decrease in γ_{RN} fraction exists over the whole deformation process. To be more specific, a drastic decrease is observed at the early stage of deformation (up to around ε=3%) and then it slows down during the later stage of deformation. The phase fraction of ε-martensite

[7] This microstructure also allows study of crystallographic or geometric effects, e.g. D_1 vs. D_4 or D_2 vs. D_3, respectively. Geometric orientation means the geometric alignment of grains with respect to the loading direction.

maintains almost constant over the whole deformation regime. Comparison of the *in-situ* and *post-mortem* data sets (i.e. surface vs. bulk) demonstrates that possible surface effects during *in-situ* measurements, e.g. roughed surface and different stress state, do not exert a significant influence on the overall trend that is observed.

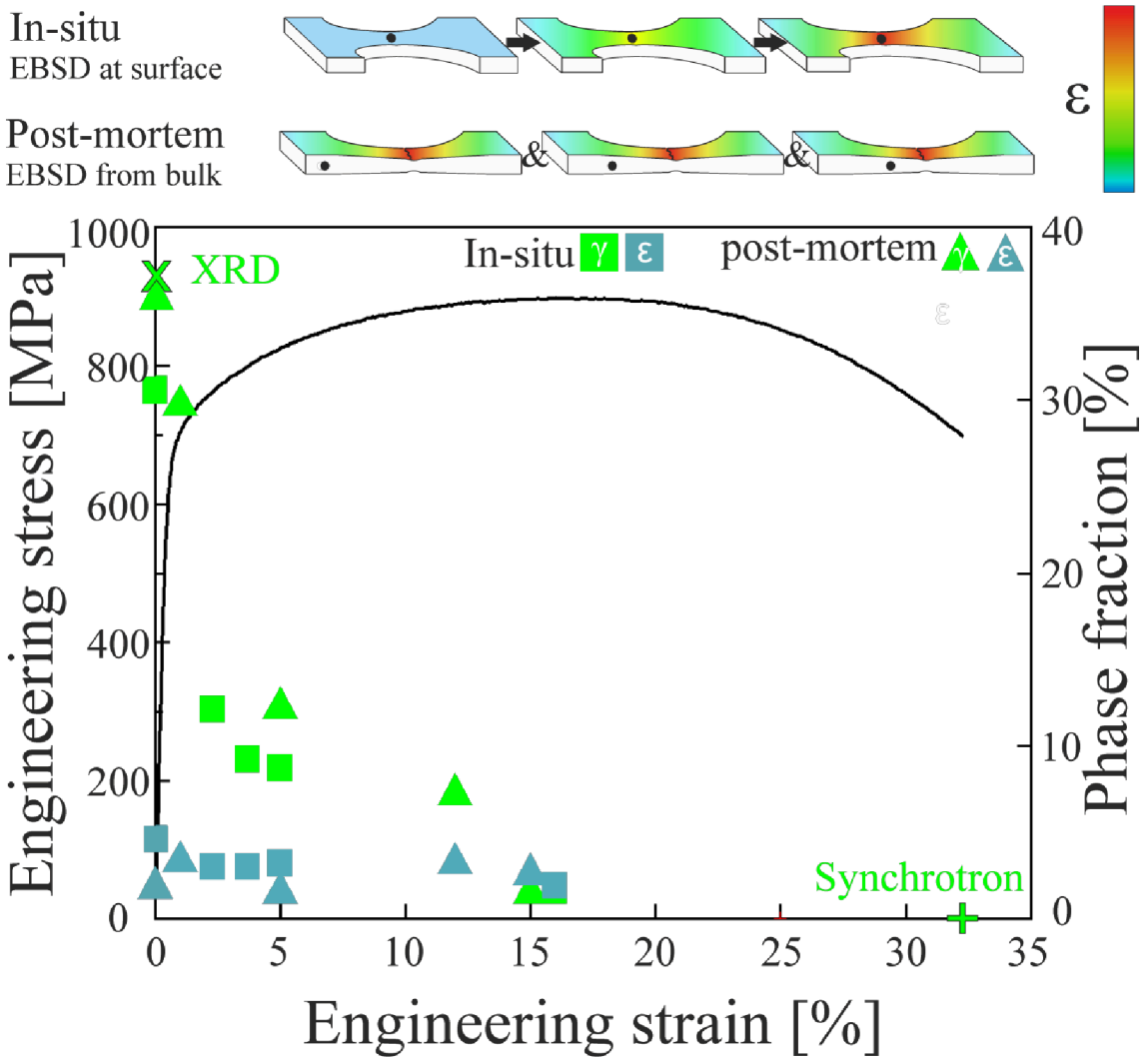

Figure 7.3: Evolution of phase fraction (γ_{RN} in green, ε-martensite in blue) in 600 °C 8 h sample during *in-situ* (square data points) and *post-mortem* (triangle data points) tensile tests measured by HR-EBSD. Green cross and plus data points represent the γ_{RN} fraction measured by XRD in the undeformed state and synchrotron X-ray diffraction measurements obtained at the deformed state, respectively. All other data points were taken by EBSD. Source: Image from [35], Courtesy of Elsevier.

The trends and characteristics of the γ_{RN} phase transformation can be analyzed from the EBSD phase maps from *in-situ* and *post-mortem* measurements, as shown in Figure 7.4a and Figure 7.4b, respectively. Here, each map is an overlay of the γ_{RN} phase map (in green) and the corresponding EBSD image quality map (in gray-scale). For the *post-mortem* measurements (probing different areas with different strain levels), a magnified image was shown as inset for a more detailed illustration of size effects on γ_{RN} stability.

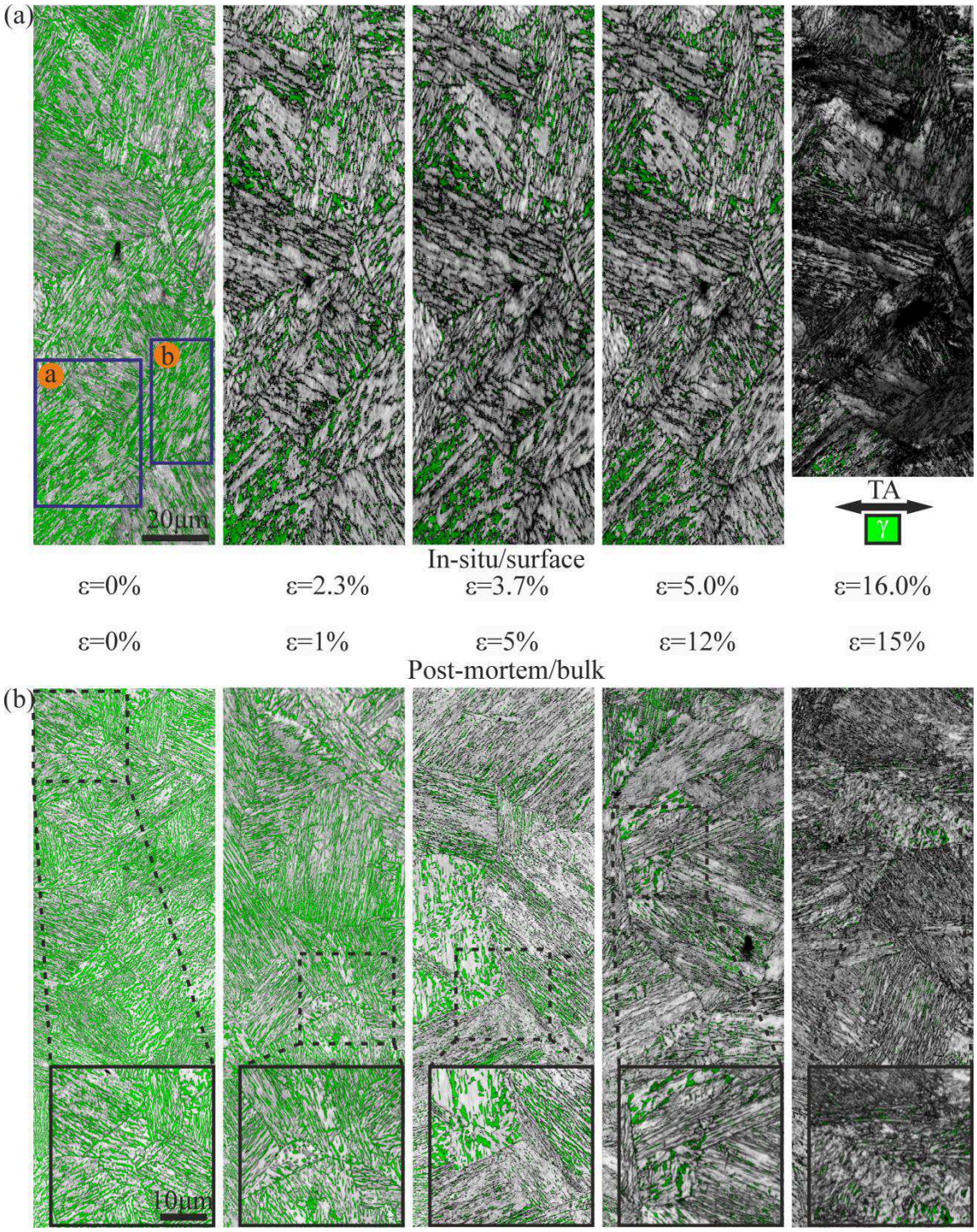

Figure 7.4: Evolution of γ_{RN} phase during (a) *in-situ* (surface data probed) and (b) *post-mortem* (bulk data probed) tensile tests. For the *in-situ* data set, two areas a-b are outlined and will be further analyzed in Figure 7.5. For the *post-mortem* data set, a magnified image is inserted for each map (TA: tensile axis). Source: Image from [35], Courtesy of Elsevier.

The γ_{RN} grains exhibit a heterogeneous size distribution at the undeformed state (Figure 7.4), as is already shown in the phase maps in Figure 7.2c. According to the γ_{RN} grain size distribution shown in Figure 7.2c$_2$, more than 72% number fraction of the γ_{RN} grains are from 0.1 to 0.3 μm^2, and ~28% number fraction of the γ_{RN} grains are from 0.3 to 4.0 μm^2. These grain size dimensions are also confirmed by HR EBSD measurements which were carried out at step size of 30nm, imaging analysis from SEM-BSE and TEM-bright field imaging (not shown here). Hence, according to their grain size, γ_{RN} grains are classified into two groups, i.e. group I (0.1-0.3 μm^2) and group II (0.3-4 μm^2). After straining to ε=2.3%, ~58% of group I γ_{RN} grains (as will be shown later in Figure 7.6), i.e. small γ_{RN} grains, already transform into α' martensite; while ~63% of the γ_{RN} grains in group II (as will be shown later in Figure 7.6), i.e. larger γ_{RN} grains, are not yet transformed. These larger γ_{RN} grains (group II) exhibit higher resistance against transformation into α' martensite and remain untransformed in the microstructure even straining to ε=5.0%. With increasing deformation to ε=16.0%, the evolving surface roughness deteriorates the image quality and leads to difficulty in the EBSD measurements. Even then, 6% of the larger γ_{RN} grains originally belonging to group II still remain untransformed in the microstructure, implying unexpected higher mechanical stability against deformation-stimulated transformation. These observations on the transformation size effect, namely, larger γ_{RN} grains (group II: 0.3-4 μm^2) exhibit higher resistance against deformation-stimulated transformation than smaller γ_{RN} grains (group I: 0.1-0.3 μm^2), are consistent within the behavior of each γ_{RN} colonies in Figure 7.4. Moreover, different γ_{RN} colonies (i.e. within different α' martensite blocks) exhibit relatively different transformation rates, underling the effects of crystallographic orientation on the mechanical stability.

This unexpected 'inverse' transformation size effect, i.e. a smaller γ_{RN} grain does not exhibit higher mechanical stability against deformation-driven transformation, is also observed by *post-*

mortem measurements. In order to exclude the influence of evolved surface roughness on EBSD measurements during *in-situ* tests, *post-mortem* EBSD measurements are carried out. These EBSD measurements are conducted on samples pre-deformed to different strain levels and then re-polished after tensile deformation, i.e. probed from the bulk of the deformed samples. Comparing the magnified insets taken for each strain level in Figure 7.4, it is clear that the majority of the γ_{RN} grains remains untransformed up to high strain levels are larger γ_{RN} grains (group II: 0.3-4 μm^2). Again, an influence of crystallographic orientation on stability of γ_{RN} grains is also observed.

To unravel the reasoning for this unexpected 'inverse' transformation size effect, i.e. ‘smaller is less stable’, two highlighted areas in the *in-situ* data set, areas a-b, are analyzed in more detail. To be more specific, the aim is to understand the microstructural features that control the mechanical stability of γ_{RN} (Figure 7.5). As shown by the IPF map, the γ_{RN} grains in these two areas exhibit different crystallographic orientations. For area-a, besides EBSD phase map, the corresponding image quality map (IQ) and kernel average misorientation (KAM) maps of γ_{RN} grains are also exhibited (Figure 7.5a). KAM is calculated as the average local misorientation of all neighboring points (here to the 2^{nd} nearest pixel) to a given kernel. This accumulated lattice curvature value serves as an index to indirectly represent the local defect density in the γ_{RN} grains [172], [173]. In order to eliminate the undesired contributions of pixels that stem either from the neighboring α’ martensite phase or from the abutting α’ martensite/γ_{RN} phase boundaries, misorientations higher than 2° are excluded from the calculation. This means that the KAM measure is used here only for the purpose of quantifying the generic defect density stored inside the γ_{RN} grains. In addition

to the α' martensite and the γ_{RN} phases, thermally-induced ε-martensite is also observed prior to deformation[8].

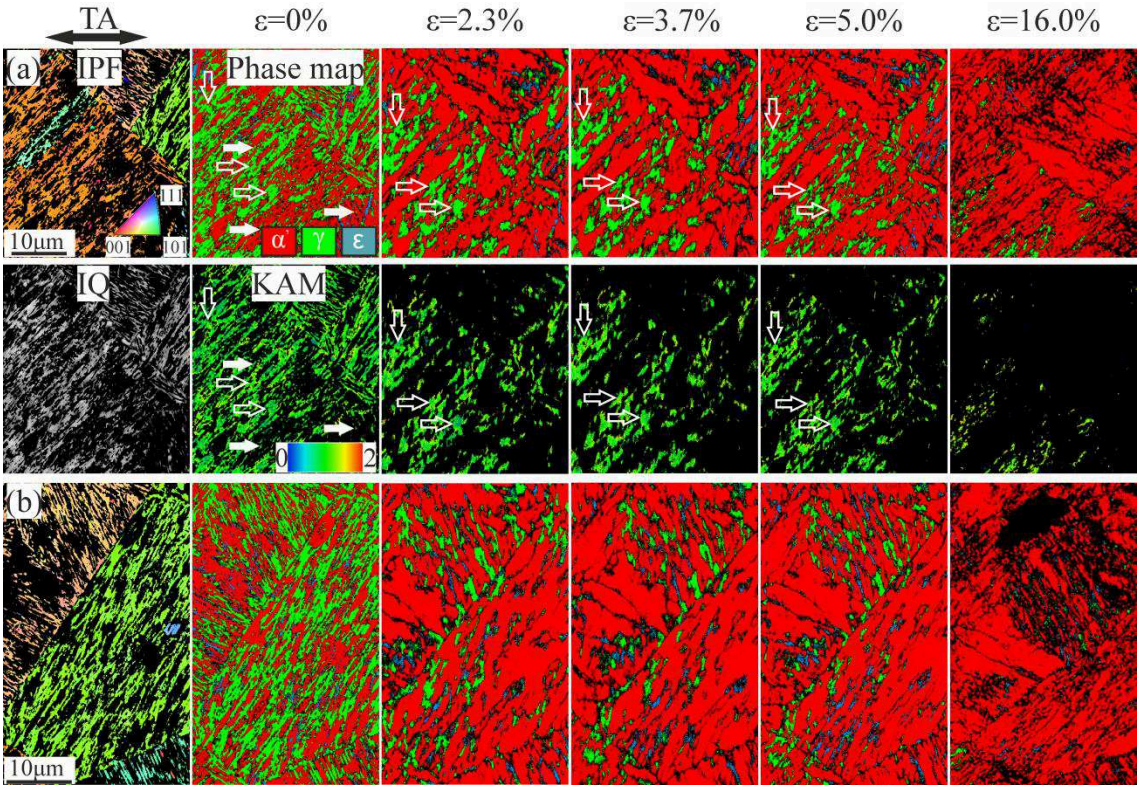

Figure 7.5: High magnification *in-situ* images of the deformation sequence of two outlined areas in Figure 7.4a. EBSD phase maps and inverse pole figure (IPF) with respect to tensile axis (TA) are provided for all areas, except for area-a the image quality map (IQ) and KAM map of γ_{RN} grains are also provided. Source: Image from [35], Courtesy of Elsevier.

As shown in Figure 7.5a, the γ_{RN} grains are formed along α' martensite lath boundaries and they consist of smaller grains (group I: 0.1-0.3 μm^2) and larger grains (group II: 0.3-4 μm^2) at undeformed state. In order to illustrate the size effects on phase stability, the γ_{RN} grains pertaining

[8] Alternative (electro-polishing based) sample preparation and the high confident index (CI) value of ε-martensite data points (CI>0.1) confirm that ε-martensite is present in the microstructure after quenching from austenite reversion treatment, and not due to improper sample preparation or to incorrectly indexed EBSD data points near phase boundaries.

to group I and group II are indicated by white solid arrows and white open arrows, respectively. When comparing to Figure 7.4, the magnified maps more clearly demonstrate that up to a nominal strain of ε=2.3%, the local strain is preferentially accommodated by the smaller γ_{RN} grains (marked by white solid arrows at ε=0%,), as indicated by their early transformation to α' martensite at low strain values. Larger γ_{RN} grains, as indicated by the white open arrows, however, remain untransformed in the microstructure. These larger γ_{RN} grains also do not seem to be significantly plastically deformed. This conclusion is obtained from the observation that no significant changes in the intrinsic KAM values of these remaining larger γ_{RN} grains are observed at this strain level. After increasing deformation to a nominal strain of ε=3.7%, the larger grains (group II: 0.3-4 μm^2) still exhibits a limited decrease in overall γ_{RN} fraction, yet a gradual increase in their intrinsic KAM values is observed. With further straining to ε=5.0%, these larger γ_{RN} grains (group II: 0.3-4 μm^2) still exhibit a negligible reduction in grain size and only partial transformation into α' martensite, but they do reveal a gradual increase in their intrinsic KAM values. When samples are further strained to ε=16.0%, only few of the larger γ_{RN} grains can still be captured by the EBSD measurements and these grains exhibit very high intrinsic KAM value.

The evolution of grain average misorientation (GAM) values of the three highlighted larger γ_{RN} grains is shown in Figure 7.6b. The GAM values are additionally adopted here to confirm the aforementioned strain accommodation process revealed by the intrinsic KAM values. GAM is the average misorientation between each neighboring pair of pixels within a grain. At the early stage of deformation, as highlighted in grey area, larger γ_{RN} grains exhibit a slight increase in the GAM value and only at higher strains, as highlighted in blue area, pronounced strain accommodation via deformation occurs (Figure 7.6b).

These results demonstrate that the majority of smaller γ_{RN} grains (group I: 0.1-0.3 μm^2) already transform into α' martensite after small strain, i.e. $\varepsilon < 2.3\%$. In contrast, the larger γ_{RN} grains (group II: 0.3-4 μm^2), are firstly plastically deformed ($\varepsilon < 2.3\%$) and only after larger deformation ($2.3\% < \varepsilon < 16\%$) gradually transform into α' martensite. Careful investigation of area-b (with different crystallographic orientations) also reveals the existence of an analogous transformation size effect for γ_{RN} grains.

While the size-dependent phase transformation behaviors of the γ_{RN} grains can already be observed from the phase maps (Figure 7.4 and Figure 7.5), the transformation size effect is further quantified and exhibited in Figure 7.6c. Here, the fraction of untransformed γ_{RN} grains within individual grain size group, namely group I (0.1-0.3 μm^2) and group II (0.3-4 μm^2), are plotted with respect to the applied strain level. On one hand, each grain size group shows a gradual transformation behavior over the whole deformation process. On the other hand, the smaller grain size group (group I) exhibits faster transformation rate than the large grain size group (group II)[9]. This is consistent with the observed phase evolution behaviors in Figure 7.4 and Figure 7.5, where larger γ_{RN} grains show higher resistance against phase transformation.

[9] Note that the partial transformation of the γ_{RN} with larger grain size leads to the grain size reduction and therefore results in the overestimation of the count of γ_{RN} with smaller grains. In other words, the size effect is even more pronounced than shown here.

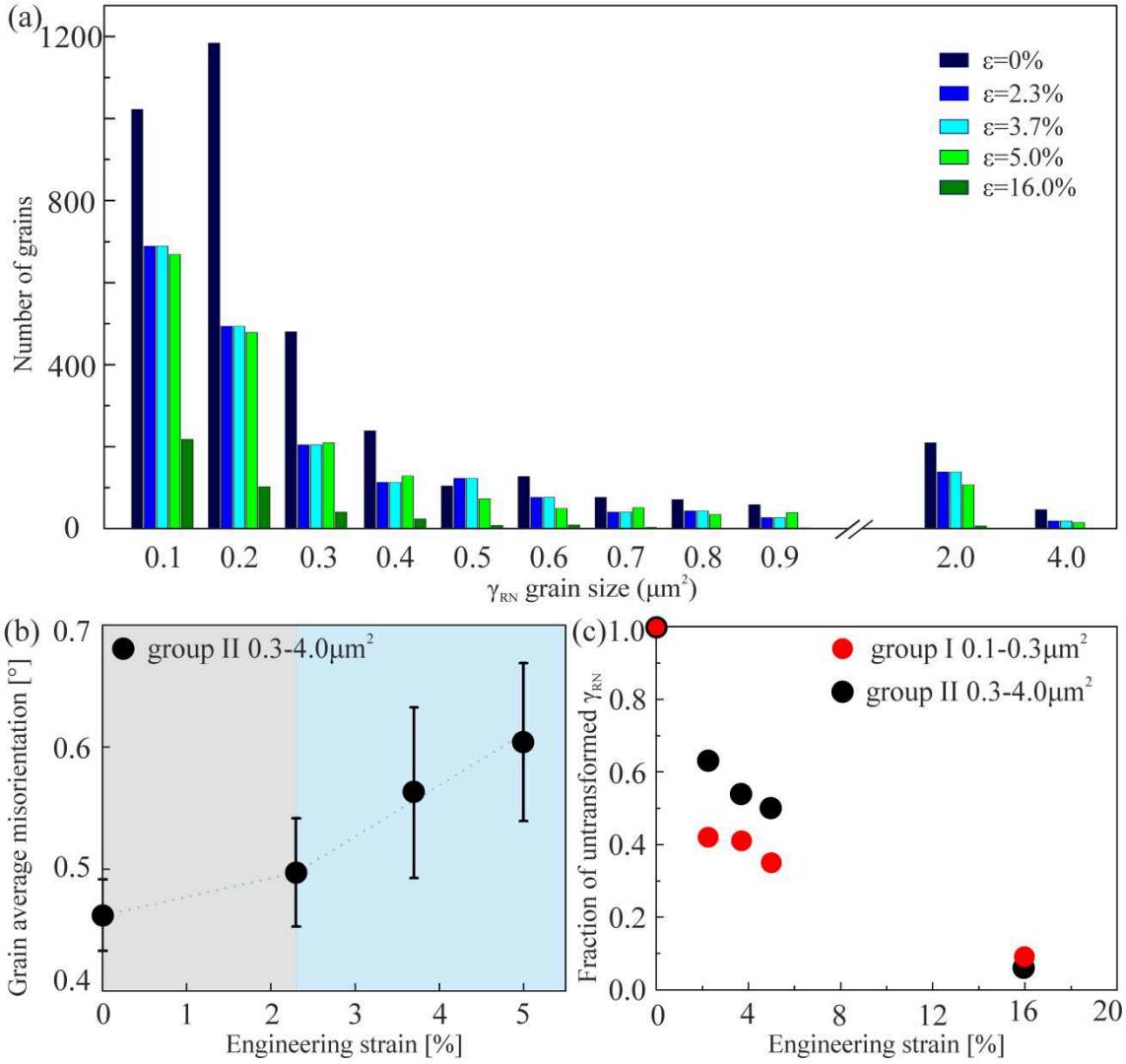

Figure 7.6: (a) Evolution of the number of γ_{RN} grains within different grain size groups during deformation. (b) Deformation behavior of larger (group II) γ_{RN} grains revealed by grain average misorientation (GAM) evolution in the three grains indicated by white open arrows in Figure 7.5a. Smaller (group I) γ_{RN} grains are too small to form in-grain deformation substructures, thus no GAM is shown for them. (c) Quantitative analysis of fraction of untransformed γ_{RN} during *in-situ* tension for smaller (group I) and larger (group II) γ_{RN} grains. Source: Image from [35], Courtesy of Elsevier.

In order to unravel the deformation mechanisms and understand the phase transformation behavior of γ_{RN} grains in 600 °C 8 h treated sample, samples at undeformed state and deformed to different strain levels, i.e. with 2% and 7% global strain, are investigated by TEM analysis

(Figure 7.7). Here, STEM and TEM images together with corresponding TEM diffraction patterns are presented.

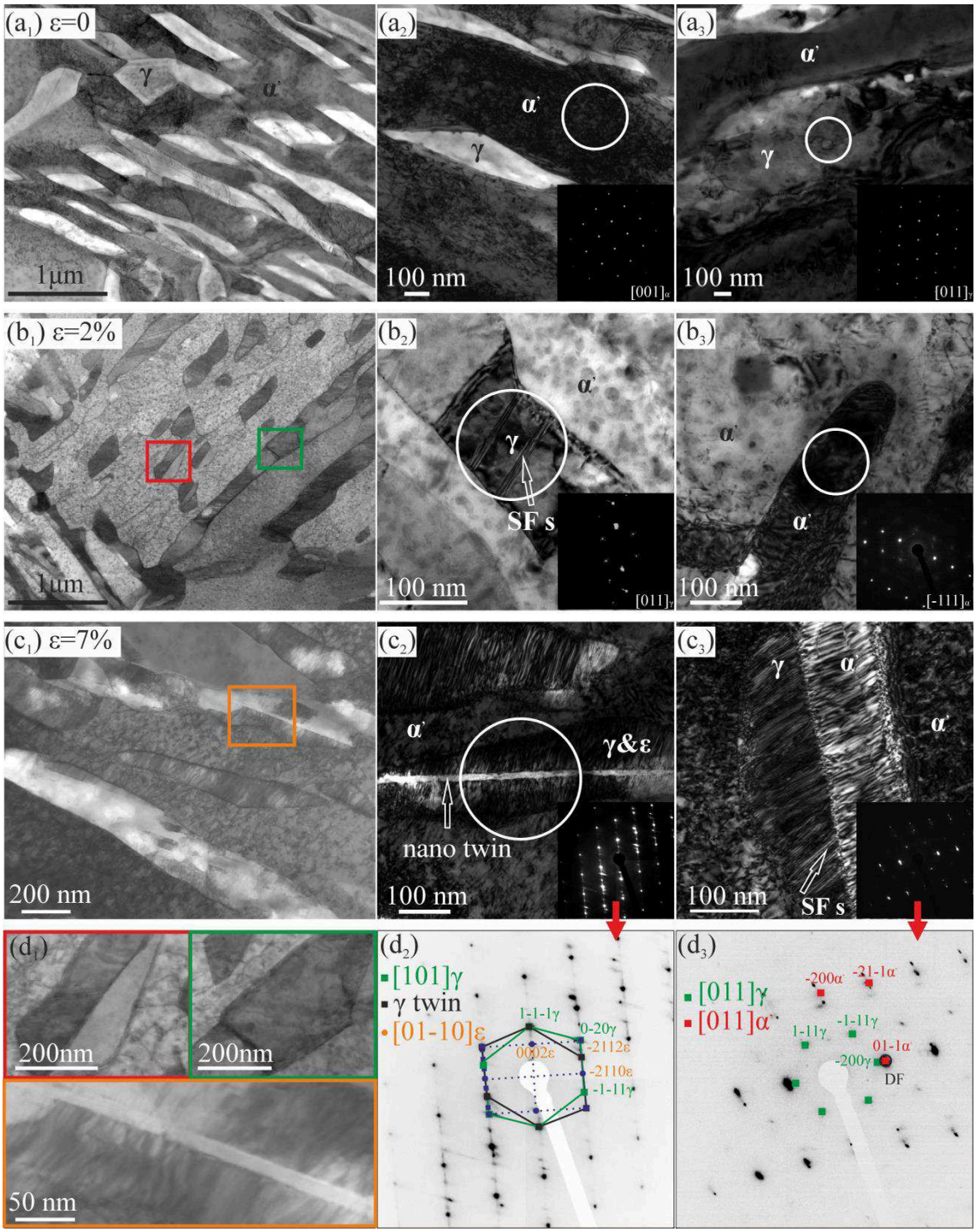

Figure 7.7: TEM observation of deformation mechanisms and phase transformation behaviors in 600 °C 8 h annealed TRIP-maraging steel: (a) microstructure in the undeformed state; (b) microstructure after 2% deformation; and (c) microstructure after 7% deformation; (d_1) magnified images from b_1 and c_1; (d_2, d_3) reconstructed diffraction patterns from c_2 and c_3, respectively. White circle represents the aperture applied for corresponding diffraction. Source: Image from [35], Courtesy of Elsevier.

At undeformed state, the microstructure consists of α' martensite phase (with nano-particles) and γ_{RN} grains (without particles), as shown in Figure 7.7a. As revealed by bright field TEM images (Figure 7.7a_2), α' martensite assumes bcc lattice structure (due to negligible carbon content) and contains a considerable high amount of dislocations after 600 °C 8 h annealing. γ_{RN} grains, in contrast, do not inherit the dislocation structures from α' martensite and exhibit only minor amount of stacking faults (SFs) (Figure 7.7a).

After globally straining to ε=2%, smaller γ_{RN} grains, e.g., the γ_{RN} grain in Figure 7.7b_2, are observed to be deformed by motion of dissociated dislocations and formation of SFs. Since γ_{RN} grains are free of precipitates, they can be easily distinguished from the α' martensite matrix. In most of these examined areas at this strain level, smaller γ_{RN} grains, e.g., the γ_{RN} grain in Figure 7.7b_3, are observed to have already transformed into α' martensite. These observations, where smaller γ_{RN} grains have readily undergone phase transformation upon deformation, are consistent with the previously presented EBSD results (Figure 7.4, Figure 7.5, Figure 7.6). In contrast, the larger γ_{RN} grains have developed a significant number of sub-boundaries, as highlighted by the green and red rectangular in Figure 7.7b_1 and also magnified in Figure 7.7d_1. These internal interfaces divide the larger crystals into different counterparts, which exhibit different contrast due to their mutual misorientation. This indicates that up to ~2% strain, larger γ_{RN} grains are deformed by development of internal boundaries and the formation of SFs inside individual counterparts.

During globally straining to ε=7%, the deformation structures within γ_{RN} grains further evolve. As shown in Figure 7.7c_1, smaller γ_{RN} grains exhibit uniform contrast due to the cumulative transformation to α' martensite. Larger γ_{RN} grains, in contrast, are further divided into groups of sub-grains which are mutually misoriented and exhibit non-uniform in-grain contrast, as shown in

Figure 7.7d_1 (magnified image from Figure 7.7c_1), Figure 7.7c_2 and Figure 7.7c_3. To understand the intrinsic nature of the deformation-induced internal boundaries and the reasoning of the observed contrast between sub-grains, selected area diffraction (SAD) analysis were conducted for regions shown in Figure 7.7c_2 and Figure 7.7c_3. The corresponding diffraction patterns are recreated and indexed in Figure 7.7d_2 and Figure 7.7d_3, respectively.

The γ_{RN} grain shown in Figure 7.7c_2 exhibits a complex diffraction pattern, consisting of γ_{RN} spots with streaks, γ_{RN} deformation twin spots as well as ε-martensite spots (Figure 7.7d_2). Therefore, this observation strongly suggests that the straight boundary with bright contrast in γ_{RN} grain in Figure 7.7c_2 is a nano-twin. The dark field image of another γ_{RN} grain, which is again split into sub-grains by nano-twin, is shown in Figure 7.7c_3. After applying dark field diffraction of spot belonging to α' martensite, the right portion of this γ_{RN} grain exhibits bright contrast, indicating that the right side sub-grain has undergone phase transformation. The deformation-induced martensite inherits the SFs structure in deformed γ_{RN} sub-grain upon transformation. The left part of this γ_{RN} grain, in contrast, still remains as an untransformed γ_{RN} grain and is deformed by forming a high density of SFs (Figure 7.7d_3).

These observations thus suggest the following strain accommodation process for the larger γ_{RN} grains. First, mechanical nano-twins are initiated and the developed twin boundaries split the γ_{RN} grains into distinct sub-grains. Next, all counterparts are deformed to slightly different local strain levels by formation of SFs, and only after sufficient internal strain accumulations, does individual counterpart transform into α' martensite. Thus partial transformation of the entire γ_{RN} grain takes place in a stepwise manner. In other words, the overall deformation induced transformation in larger γ_{RN} grains is delayed by the preceding deformation induced twinning.

The presences of these nano-twins which seem to be the origin of the unexpected transformation size effects cannot be observed by *in-situ* HR-EBSD measurements due to its limited resolution. Thus in order to track the formation of the mechanical nano-twins during *in-situ* deformation, an alternative higher resolution method is applied. To be more specific, the development of internal boundaries within γ_{RN} grains are captured using SE and ECCI images during *in-situ* 3-point bending [174]–[176], as shown in Figure 7.8a and Figure 7.8b.

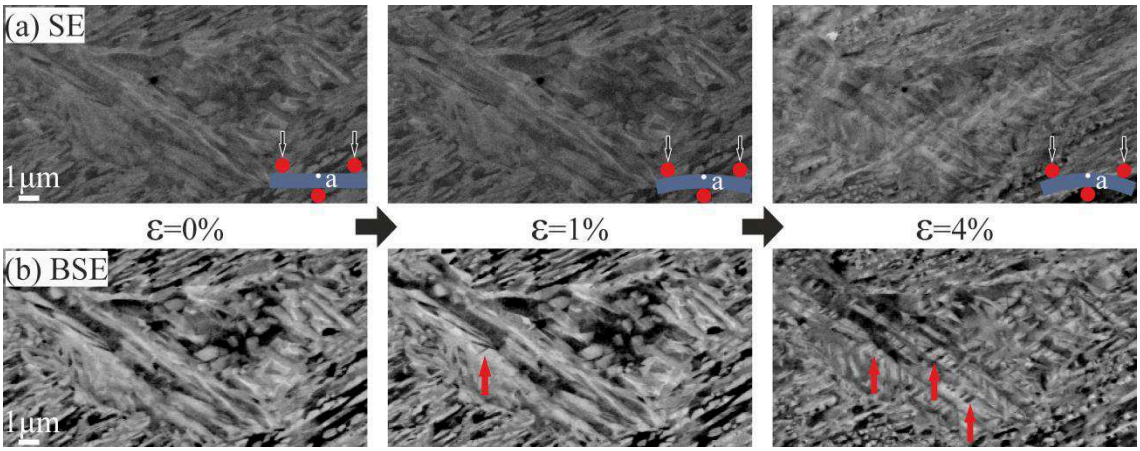

Figure 7.8: Investigation of the tension side of a sample during *in-situ* 3-point bending experiments by (a) secondary electron imaging, demonstrating the evolving surface morphology; and (b) electron channeling contrast imaging (ECCI), demonstrating the appearance of twin boundaries, as indicated by red arrows. Source: Image from [35], Courtesy of Elsevier.

As known from the EBSD measurements in Figure 7.2, the 600 °C 8 h annealed sample exhibits a complex microstructure even at undeformed state. With straining, the change in channeling conditions due to crystal rotations and shadowing due to surface roughening lead to difficulty in microstructure mapping (Figure 7.8a, Figure 7.8b). Despite of these difficulties, the gradual evolution of straight boundary segments, which appear with different channeling contrasts from neighboring grains, are clearly observed in the larger γ_{RN} grains with straining. This phenomenon is shown in the sequence of Figure 7.8b$_1$ (0% strain), Figure 7.8b$_2$ (1% strain) and Figure 7.8b$_3$ (4%

strain) as highlighted by the red arrows. Furthermore, the morphology of these boundaries is similar to those observed in Figure 7.7b_1 and Figure 7.7c_1. Hence, the observed nano-twinning mechanism found by TEM analysis is further confirmed by the *in-situ* 3-point bending experiments.

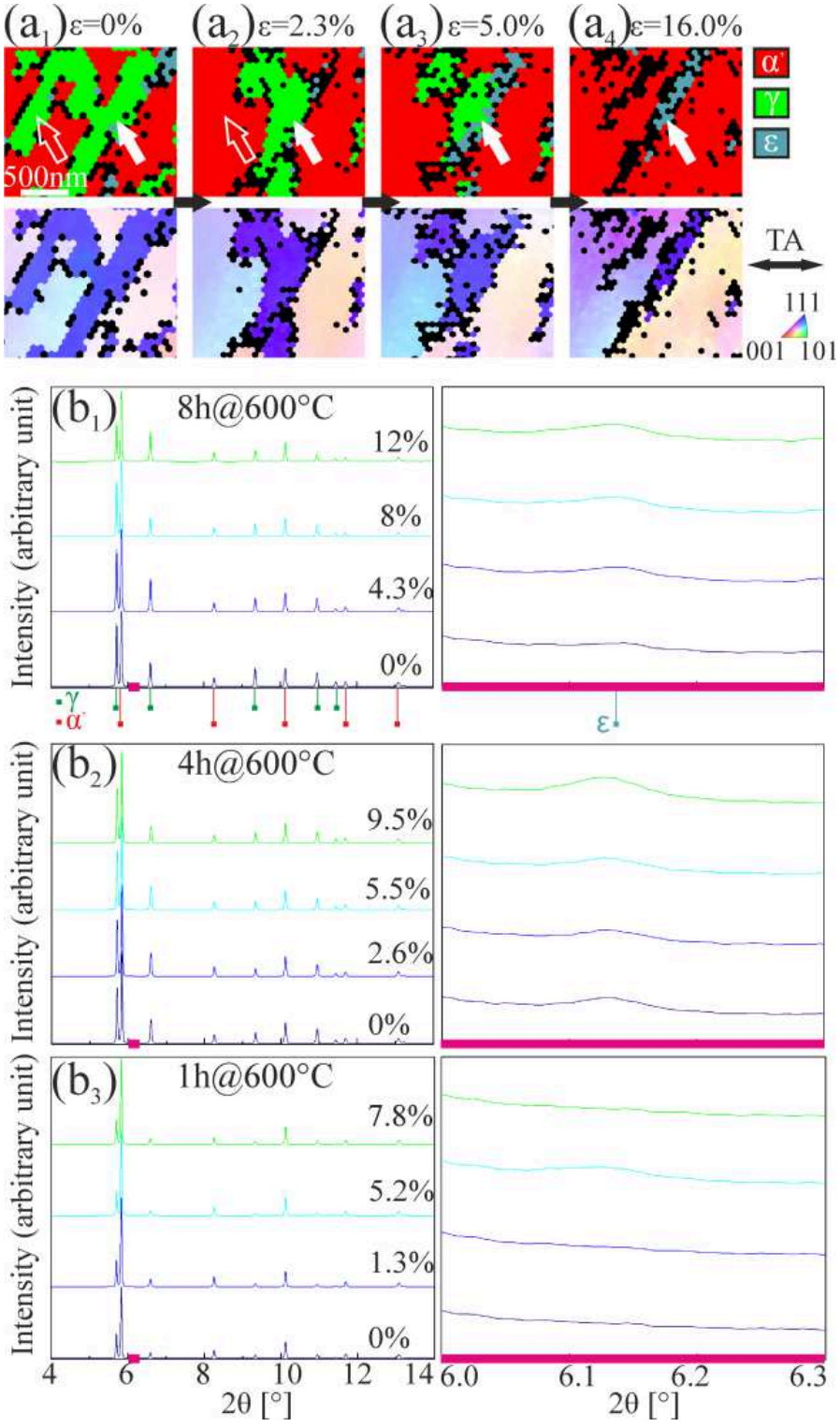

Figure 7.9: ε-martensite formation analyzed by (a) EBSD phase map and IPF map with respect to the tensile axis (TA) in the 600°C 8h sample, and (b) synchrotron X-ray diffraction measurements of the 600°C 8h/4h/1h samples with different strain values. ε-martensite diffraction peaks are not indexed together with γ_{RN} phase and α' martensite phase in the left part of Figure 7.9b due to their relatively low intensities. Instead, one 2θ

angular regime (highlighted in pink) corresponding to ε-martensite is magnified and shown on the right part of Figure 7.9b. Source: Image from [35], Courtesy of Elsevier.

Besides γ_{RN} and α' martensite phase, a small amount of ε-martensite, i.e. ~3 vol. %, is also present in the microstructure at undeformed state (Figure 7.5). Upon straining, 6.2% of γ_{RN} grains are transformed to α' martensite phase in a direct manner. Only few γ_{RN} grains (~1vol. %) transform first to ε-martensite phase. Only 0.7% of these γ_{RN} grains are further transformed to α' martensite phase with straining. This indicates that the mechanically-induced ε-martensite assumes a high resistance against further transformation. These phenomena are captured by *in-situ* EBSD measurements, as demonstrated by a representative region cropped from Figure 7.4 and shown in Figure 7.9a. Here, two γ_{RN} grains are indicated by white open arrow and white solid arrow, respectively. The former is observed to transform readily into α' martensite phase after straining to 2.3%. The majority of the γ_{RN} grains are observed to transform in this manner during deformation. The latter, in contrast, transforms first to ε-martensite phase at a strain of 5.0%. This grain prevails as ε-martensite up to 16.0% strain and does not transform into α' martensite phase with further deformation.

The SXRD measurements also confirm the observed high mechanical stability of ε-martensite. To demonstrate these phenomena, peak profiles of samples aged for 8 h, 4 h and 1 h at 600 °C measured from locations with known strain levels from DIC measurements are shown from Figure 7.9b_1 to Figure 7.9b_3, respectively. For each case, the peak profile of a 2θ angular regime containing a ε-martensite peak (highlighted in pink) is magnified and shown on the right hand side. It is observed that during deformation of all three samples, the ε-martensite intensities vary only within the experimental scatter.

7.3 Discussion

The aim of this chapter is to systematically investigate size effects on mechanically-induced phase transformations. For this purpose, a model microstructure with γ_{RN} grain size distribution is designed with support from DICTRA calculations. It is essential in the current approach that all the γ_{RN} grains assume the same chemical composition, hence, the same thermodynamic stability. Thus, the observed effects on mechanical stability are resulted from grain size and neighborhood effects but independent of chemical composition. The discussion of the observed unexpected size-dependence of the transformation behaviors is carried out following the sketch shown in Figure 7.10.

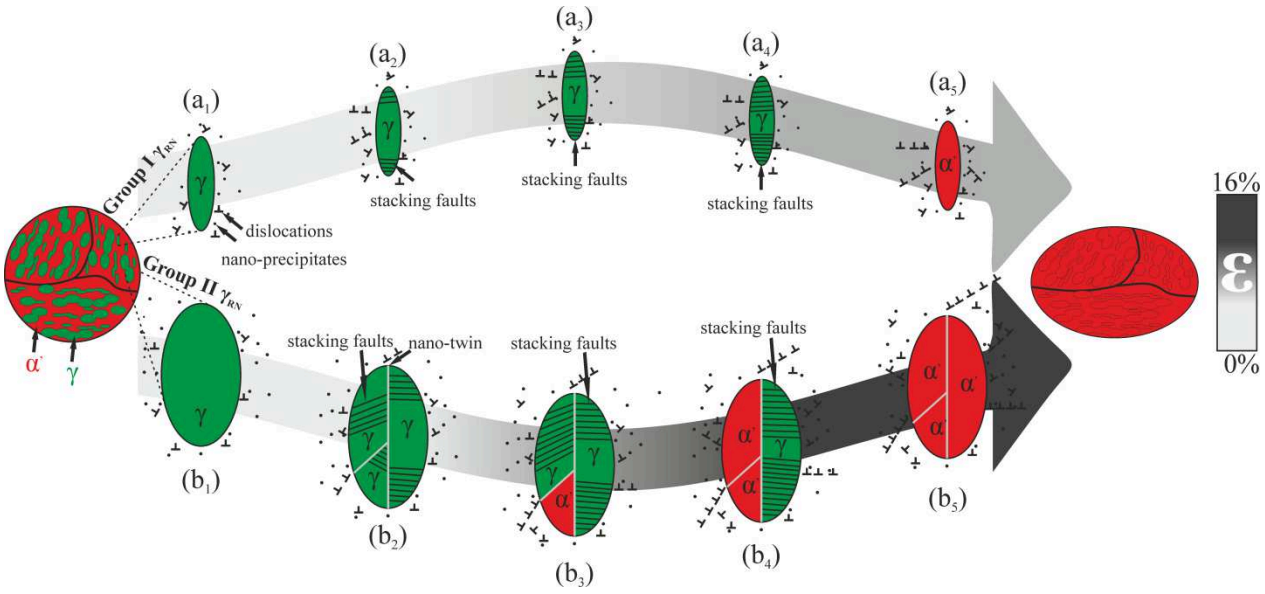

Figure 7.10: Schematic sketch of the size-dependent deformation and transformation behaviors in (a) group I (0.1-0.3 µm^2) small γ_{RN} grains; (b) group II (0.3-4 µm^2) larger γ_{RN} grains. All γ_{RN} grains are initially surrounded by α' martensite matrix containing dislocations (T symbols) and nano-precipitates (dot symbols). The deformation induced boundaries shown in Figure 7.10b$_2$ are mechanical twins; α' martensite is nucleated at SFs; SFs are also inherited into the final α' martensite during the athermal phase transformation (not shown here for better visual clarity). Source: Image from [35], Courtesy of Elsevier.

Prior to deformation, all γ_{RN} grains exhibit a low SFs density and show a uniform in-grain orientation spread (Figure 7.2d, Figure 7.7a_1). Thus, γ_{RN} grains do not inherit the dislocation structure from α' martensite phase upon the reverse transformation. When considering this phenomenon in conjunction with the accompanying partitioning of elements between α' martensite and γ_{RN} phases (Figure 7.2), the reversion process occurred during 600 °C isothermal holding is most likely controlled by a reconstructive phase transformation process. Before transformation takes place, all γ_{RN} grains are firstly plastically deformed. The deformation is observed to occur via accumulation of partial dislocations and formation of regular arrays of SFs (Figure 7.7b_2). Further deformation proceeds via massive multiplication of SFs (Figure 7.7c_2). Jaswon [177] originally proposes that the faults produced by dissociation of fcc Shockley partial dislocations represent a bcc-related structure in fcc. Later Olson and Cohen [178] propose that from this faulted structure in deformed fcc lattice, atoms can be further shifted into bcc positions through a second shear mechanism. Thus, the SFs configurations in deformed γ_{RN} grains, particularly when they intersect with each other, may potentially act as α' martensite nuclei (Figure 7.7c_3). The athermal character of this mechanism is indicted by the fact that upon phase transformation of the deformed γ_{RN} grains, the newly formed α' martensite inherits the SFs structure (Figure 7.7c_3).

While this sequence describes the global transformation process observed in 600 °C 8 h reversion treated sample, a pronounced size effect applies: for the smaller γ_{RN} grains (group I: 0.1-0.3 μm^2), the aforementioned process takes place after small amount of deformation, e.g. ~2% strain (Figure 7.10a_1-a_5); for the larger γ_{RN} grains (group II: 0.3-4 μm^2), the in-grain deformation proceeds in a more complex manner (Figure 7.10b_1-b_5). The formation of SFs in larger γ_{RN} grains is typically accompanied by mechanical twinning process. Moreover, higher strains are

compulsory for the onset of the α' martensite transformation in larger γ_{RN} grains. These points are discussed in more detail in the following.

The build-up of the in-grain deformation substructures, i.e. partial dislocations and nano-twins, in larger γ_{RN} grains (group II) is indirectly indicated by (i) the strongly increasing GAM values from *in-situ* EBSD measurements (Figure 7.6b); directly shown by (ii) the TEM analysis (Figure 7.7c); and (iii) the BSE imaging from the *in-situ* 3-point bending experiments (Figure 7.8). Identical indications of such in-grain deformation substructures in the smaller γ_{RN} grains (group I), however, are not observed.

Therefore, the transformation size effect is essentially attributed to the differences in the build-up of in-grain deformation substructures in larger and smaller grains, i.e. a TWIP-type deformation behavior is mainly prevailing in the larger γ_{RN} grains (group II: 0.3-4 μm^2) and less activated in smaller γ_{RN} grains (group I: 0.1-0.3 μm^2).

This associated mechanical twinning size effect, such as described here, is consistent with earlier reports [179], [180]. The model of Mahajan and Chin [181] explains that nucleation of deformation twins proceeds when fault pairs stemming from two split dislocations react producing three Shockley partials on adjacent planes. For each stacking fault, the two associated partial dislocations are separated due to the local repulsive force of such a configuration in relaxed state. In the case of in-grain dislocation pile-ups, the partial spacing for one of the dislocations can be reduced down to several nm, e.g. supported by the stress concentrations at the tips of the pile-ups, such that it can glide on the adjacent slip plane. If a third fault pair now reaches one side of such a double stacking fault embryo, the two partials that form the interface of the double-layer fault can combine and move to the next adjacent layer and slip away. Thus, the final step creates a 3-layer stacking fault arrangement. The Shockley partials on one side of

the fault form an interface whose Burgers vectors sums to zero, immobilizing the interface under the applied stress. Therefore the Shockley partials on the opposite side of the stacking fault are free to move away from the interface. The subsequent growth of such newly formed twins proceeds by the co-operative motion of the associated partial dislocations on successive {111} planes [178].

The critical twinning stress in the model of Mahajan and Chin as described above is determined by the force required to bring the internal partial dislocations of the two stacking faults to a spacing below several nm.

As this critical step for mechanical twinning must be assisted by the stress concentrations at dislocation pile-ups, a higher nominal twinning stress is needed for smaller γ_{RN} grains. The underlying reason is that due to the long mean free path in larger γ_{RN} grains, large dislocation pile-ups can be easily developed during straining. In contrary, in small γ_{RN} grains, respectively dense pile-ups of dislocations can only be formed under higher mechanical loads. Thus, it is difficult to achieve the critical twin nucleation stress in smaller γ_{RN} grains, e.g. only under higher nominal stresses. This marks a size effect in terms of facilitated twin nucleation at small loads in large γ_{RN} grains and at higher loads in small γ_{RN} grains. This effect explains the fact that mechanical twins are less frequently observed in the smaller γ_{RN} grains (group I: 0.1-0.3 μm^2).

As measured by *in-situ* EBSD, the larger γ_{RN} grains (group II: 0.3-4 μm^2) exhibit gradual increase in GAM values, which indirectly imply the gradual build-up of complex and dense in-grain deformation substructures therein (Figure 7.6b). In addition, the majority of these γ_{RN} grains exhibit partial transformation behaviors, e.g. large γ_{RN} grains transform into α' martensite in a stepwise manner (Figure 7.5). Furthermore, it was directly observed by TEM analysis that mechanical nano-twins are formed in larger grains and divide them into sub-grains (Figure 7.7c_1).

Each sub-grain is deformed individually by multiplication of SFs (Figure 7.7c_2). After sufficient strain accumulation, each compartment transforms into α' martensite eventually (Figure 7.7c_3). In other words, these grains transform into α' martensite in a step by step manner and thus exhibit higher overall mechanical stability. Similar consecutive effect of developed in-grain deformation substructures on the phase transformation behavior is already indicated in previous works [182], [183]. Leslie et al. [182] reported that the boundaries developed inside the austenite can increase its stability against further phase transformation via hindering the growth of the martensite plates. Masumura et al. [184] recently demonstrated that the variations in the developed deformation microstructure resulted in different deformation induced martensitic transformation behaviors. Nakada et al.[183] also reported that due to the generation of an anisotropic strain field associated with deformation twinning, the occurrence of twinning may influence the selected variants for deformation-induced martensite. In the 600 °C 8 h reversion-treated sample, the Mn content in γ_{RN} is around 16% (mass %) (Figure 7.1), and both TWIP and TRIP mechanisms serve as active deformation mechanisms. High Mn steels with similar Mn content are also reported to exhibit existence of both TWIP and TRIP effects during deformation, but dominated by TRIP effect [185]. Combining all these, it is proposed that the current chemical composition of γ_{RN} grains gives rise to a lower border where mechanical twinning could also be activated, e.g. specific SFE value related deformation mechanism. Mainly in those larger γ_{RN} grains, mechanical twinning is favored. This further leads to the build-up of a complex and dense deformation sub-structures. These mechanical twins additionally modify the strain field anisotropy of γ_{RN} sub-grains and thus restrict possible martensite variants selections for deformation-induced phase transformation, leading to a delayed overall phase transformation process and higher overall phase stability in larger γ_{RN} grains.

Another transformation size effect is present for ε-martensite. Previous reports often described ε-martensite as an intermediate phase between the γ and α' martensite phase transformation [186], [187]. In their material systems, the appearance of α' martensite was often located at intersections of ε-martensite plates. However, in the current work, no intersections of ε-martensite are observed due to the small grain size. The high mechanical stability of individual ε-martensite zones is confirmed by the *in-situ* EBSD measurements (Figure 7.5, Figure 7.8a) and also further by the SXRD data (Figure 7.8b). Hence, it is observed that in the current TRIP-maraging steel small grains (<4.0 μm^2) with ε-martensite are stable against further transformation into α' martensite.

Considering these points, it is proposed that a size-dependent competition between transformation and twinning behaviors in the γ_{RN} grains exist in the current TRIP-maraging steel. Due to associated size effect in the TWIP behavior, twinning is mainly activated in larger γ_{RN} grains (group II) and less favored in smaller γ_{RN} grains (group I). In the larger γ_{RN} grains, the mechanical nano-twins and arrays of partial dislocations jointly lead to the progressive development of pronounced in-grain deformation substructures. Higher strains are necessary for initiating martensitic transformation. After stepwise transformation of all sub-grains, the complete transformation of these grains into α' martensite is finished. For smaller γ_{RN} grains, no indication of such a process is observed. Smaller γ_{RN} grains are deformed as a unit by multiplication of SFs. Then phase transformation takes place readily after small amount of deformation. Therefore, a coupled size effect in terms of both TWIP and TRIP effects in γ_{RN} grains is present in the current 600 °C 8 h reversion-treated alloy. This leads to the unexpected 'smaller is less stable' phenomenon which is consistently explained as a transformation size effect. As underlined in the introduction of Chapter 7, the present size effect will also be influenced by other microstructural factors, e.g. chemical composition, crystallographic

orientation, defect structure and neighboring phases, etc.. Therefore, under the influence of these factors, different size effects can be expected in other TRIP-assisted nanostructured steels.

Chapter 8 Further microstructure and mechanical property optimizations via cold rolling of as-quenched martensite

8.1 Introduction

As systematically studied in Chapter 4 and Chapter 7, the enhanced mechanical properties therein are linked to the dynamic nature of the strain partitioning between the martensite and austenite phases, which itself arises due to a size dependent competition between mechanically-induced martensitic transformation and mechanical twinning mechanisms in austenite [35]. In this chapter, a practical approach is proposed to make use of this size dependence and to achieve further enhanced mechanical property combinations.

The employed strategy is as follows: to achieve a wider austenite grain size distribution, it is required to introduce a distribution of nucleation sites for austenite in the martensite microstructure, e.g. sites with different nucleation energy barriers. The nucleation energy barrier associated with the reversion of martensite to austenite consists of three energy components [15], [188]–[191], namely the change in chemical free energy, interfacial energy or defect energy. The first energy component, i.e. the change in free energy, arises from the difference in chemical compositions and atomic arrangements between austenite nucleus and martensite [190]. The second energy component, i.e. the change in interfacial energy, is determined by the net interfacial energy differences between the original martensite/martensite boundary, the newly formed austenite/martensite interface and the austenite/austenite interface (if an internal boundary exists in the nucleus) [15]. The final energy component, i.e. the change in defect energy, is the gain in elastic energy since the highly elastically strained martensite is replaced by the austenite nucleus with high packing density [15]. In the current reversion treated lath martensitic steels, it is shown that (i) the reversion of martensite to austenite is a diffusion-controlled process and the

reverted austenite grains exhibit minor defects; and (ii) the reverted austenite and martensite exhibit a K-S (Kurdjumov-Sachs) orientation relationship at least along one side of the boundaries. Thus the decisive parameter in introducing differences in nucleation energy lies in controlling the character of martensite boundaries, e.g. nucleation along high angle martensite boundary would lead to high gain in both interfacial energy and defect energy. This is already observed in Chapter 4. During the short time annealing of as-quenched martensite at 600 °C, reverted austenite grains are mainly formed along prior austenite grain boundaries, martensite packet/block boundaries, e.g. with high misorientations. With longer annealing time, reverted austenite grains are also formed along martensite lath boundaries, e.g. with low misorientations. Thus, modifying distribution of martensite boundaries would efficiently lead to diverse nucleation sequences for reverted austenite.

It is well-known that cold deformation could introduce a spatial distribution of boundaries with a range of misorientations in the microstructure, e.g. shear bands, lamellar boundaries with geometrically necessary dislocations, and cell boundaries with statistically distributed dislocations, etc. [192]–[195]. Therefore, in this chapter, the aim is to modify the distribution of boundaries in lath martensite by cold rolling, and thus adjust the nucleation barrier for austenite and therefrom develop an optimized microstructure with a dispersed grain size of reverted austenite. At relevant points in the results and discussion, the microstructure and mechanical response of the original nanolaminate martensite-reverted austenite steel (Chapter 4) will be referred to and compared.

In the following, first the influences of cold rolling on the martensite microstructure and the subsequential austenite reversion process are presented. Then the mechanical properties of the reversion-treated cold-rolled martensite are examined and the microstructure evolutions during

deformation are demonstrated. In the end the relationships between the microstructure and mechanical properties in reversion-treated cold-rolled martensite are discussed and conclusions are drawn.

8.2 Results

8.2.1 Microstructure evolutions during processing

The as-quenched microstructure and the cold-rolled microstructure are characterized by light optical micrograph and EBSD phase map with overlay of image quality map in Figure 8.1. At as-quenched state, the microstructure consists of α' martensite phase (phase in red) (Figure 8.1a_2) and boundaries in the microstructure include prior austenite grain boundaries, martensite packet/block/lath boundaries (Figure 8.1a_1). After cold rolling, the deformed microstructure is characterized by α'martensite phase with numerous amounts of deformation bands (Figure 8.1b_1-b_2).

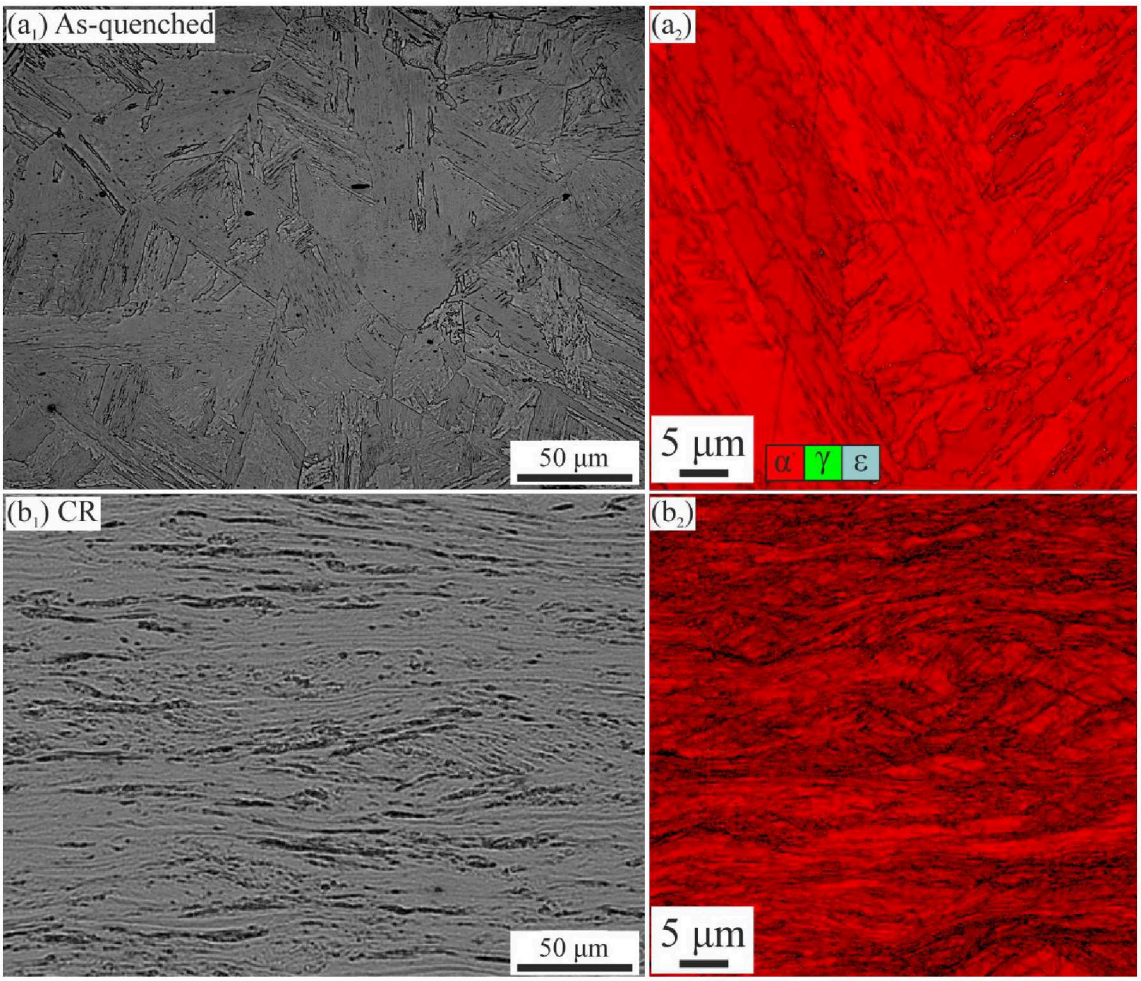

Figure 8.1: Microstructure of (a) as-quenched martensite; (b) cold-rolled martensite, as characterized by (1) light optical micrograph; (2) EBSD Phase map with overlay of image quality map.

The influence of cold rolling on distribution of boundaries in the microstructure is demonstrated in Figure 8.2. The distributions of boundaries in as-quenched martensite and cold-rolled martensite are plotted in Figure 8.2a_1 and Figure 8.2b_1, respectively, where boundaries with 2°-15° misorientations, e.g. low angle boundaries, are in blue, and boundaries with 15°-180° misorientations, e.g. high angle boundaries, are in white. Compared to the as-quenched α' martensite (Figure 8.2a_1), cold-rolled martensite contains not only a higher density, but also a wider spatial distribution of high angle and low angle martensite boundaries (Figure 8.2b_1). The difference in density and spatial distribution of martensite boundaries can be clearly seen by

comparing the two magnified images shown in Figure 8.2a_2 and Figure 8.2b_2, and the plotted martensite boundary distribution in Figure 8.2c.

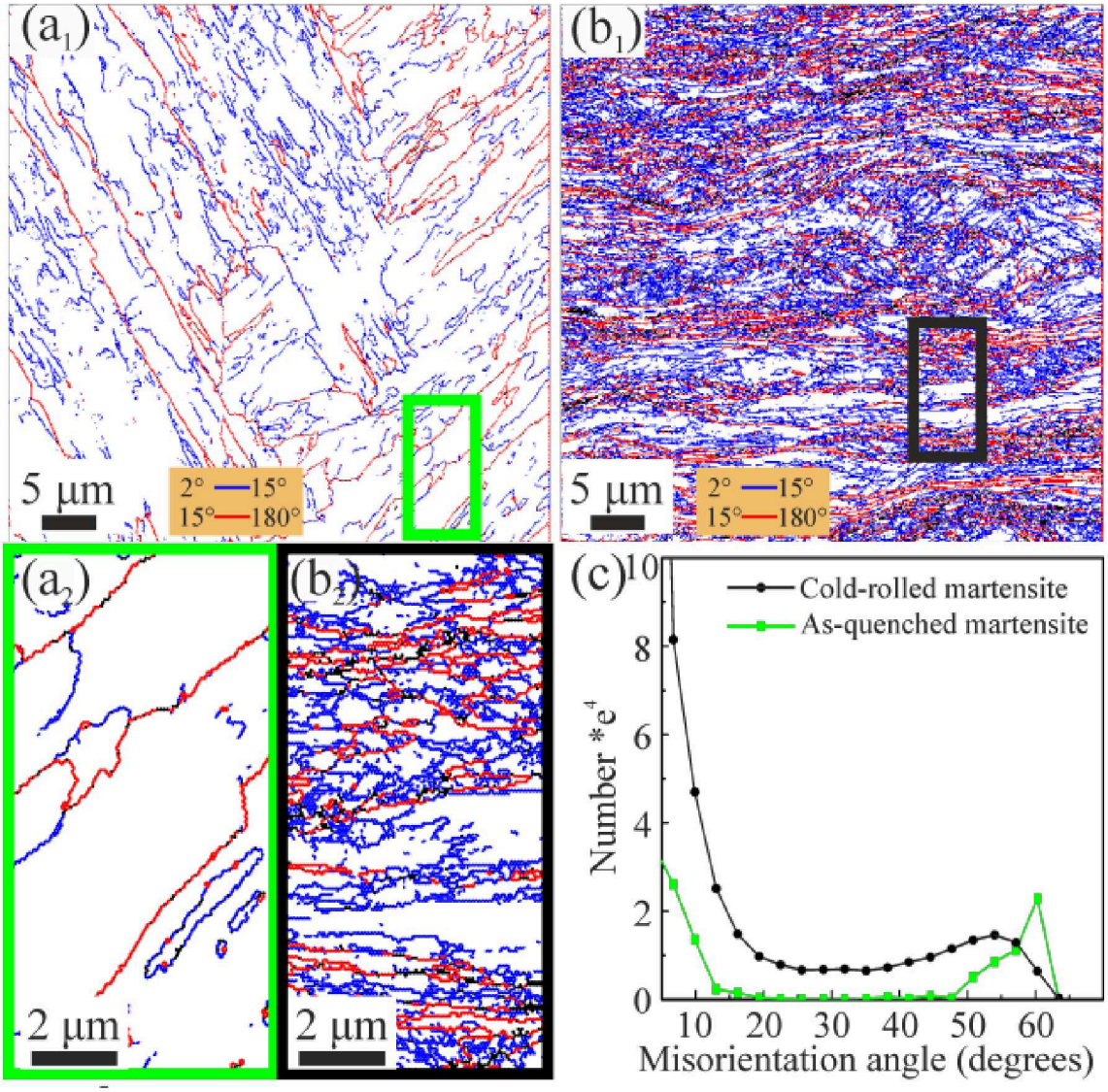

Figure 8.2: Distribution of boundaries in (a_1, a_2) as-quenched martensite; (b_1, b_2) cold-rolled martensite, as characterized by EBSD measurements. (c) Quantified distribution of boundaries in martensite.

Based on the starting state of the microstructure (as-quenched: AQ, cold-rolled: CR), the annealing time at 600 °C and the microstructural constitutes (martensite: M, austenite: A), in the following of Chapter 8, samples are named as listed in Table 8.1.

Table 8.1 Sample abbreviations based on the starting state of the microstructure (as-quenched: AQ, cold-rolled: CR), the annealing time at 600 °C and the microstructural constitutes (martensite: M, austenite: A).

Annealing time @ 600 °C	Microstructure prior to annealing	
	As-quenched martensite	Cold-rolled martensite
0 min	$M_{(AQ)}$	$M_{(CR)}$
10 min		$M\text{-}A_{(CR+10min)}$
30 min		$M\text{-}A_{(CR+30min)}$
1 h	$M\text{-}A_{(AQ+1h)}$	$M\text{-}A_{(CR+1h)}$
4 h	$M\text{-}A_{(AQ+4h)}$	
8 h	$M\text{-}A_{(AQ+8h)}$	

The influence of the density and distribution of martensite boundaries on the subsequential γ reversion process at 600 °C is demonstrated in Figure 8.3. Here, EBSD phase map for $M\text{-}A_{(AQ+1h)}$, $M\text{-}A_{(AQ+4h)}$ and $M\text{-}A_{(AQ+8h)}$ (Figure 8.3a_1-a_3), phase map (Figure 8.3b_1-b_3) and γ grain size map (Figure 8.3c_1-c_3) for $M\text{-}A_{(CR+10min)}$, $M\text{-}A_{(CR+30min)}$ and $M\text{-}A_{(CR+1h)}$ are presented. In γ grain size map, each grain is color coded (from blue to red, rainbow code) by its grain size, e.g. γ grains in red are larger than those in blue.

For the as-quenched martensite, γ reversion takes place first along martensite packet and block boundaries (Figure 8.3a_1), then also long martensite lath boundaries (Figure 8.3a_2) and nano-films of γ eventually grow thicker after 8 h annealing (Figure 8.3a_3).

Due to the higher density and spatial distribution of martensite boundaries in cold-rolled martensite, a different γ reversion process is observed. After 10 min annealing, reverted γ grains are formed in the microstructure (Figure 8.3b_1). Comparing with the distribution of martensite boundaries at cold-rolled state (Figure 8.2b_1, b_2), it is clear that reverted γ grains are preferentially formed along high angle martensite boundaries, e.g. shear bands, in $M\text{-}A_{(CR+10min)}$. The preferred nucleation behavior of γ grains along high angle boundaries is consistent with that of as-quenched martensite (Figure 8.3a_1). During further annealing to 30 min, these γ grains along high angle boundaries continue to grow while more γ grains are observed to nucleate along

boundaries with relatively lower angle misorientations (Figure 8.2b_1, Figure 8.3b_2). Due to the difference in nucleation sequences and thus time available for grain growth, γ grains along high angle boundaries assume larger grain size than that along low angle boundaries M-$A_{(CR+30min)}$ (Figure 8.3c_1-c_2). This process proceeds with further annealing. Eventually after 1 h, majority of martensite boundaries are decorated by reverted γ grains (Figure 8.3c_3). Comparing with M-$A_{(CR+10min)}$ (Figure 8.3c_1) and M-$A_{(CR+30min)}$ (Figure 8.3c_2), reverted γ grains assume an overall larger grain size in M-$A_{(CR+1h)}$.

Thus, for both as-quenched martensite and cold-rolled martensite, high angle boundaries promote earlier nucleation of γ grains over low angle boundaries. Moreover, the high density and spatial distribution of high and low angle boundaries in cold-rolled α' martensite leads to a size distribution of γ grains after 1 h annealing at 600 °C.

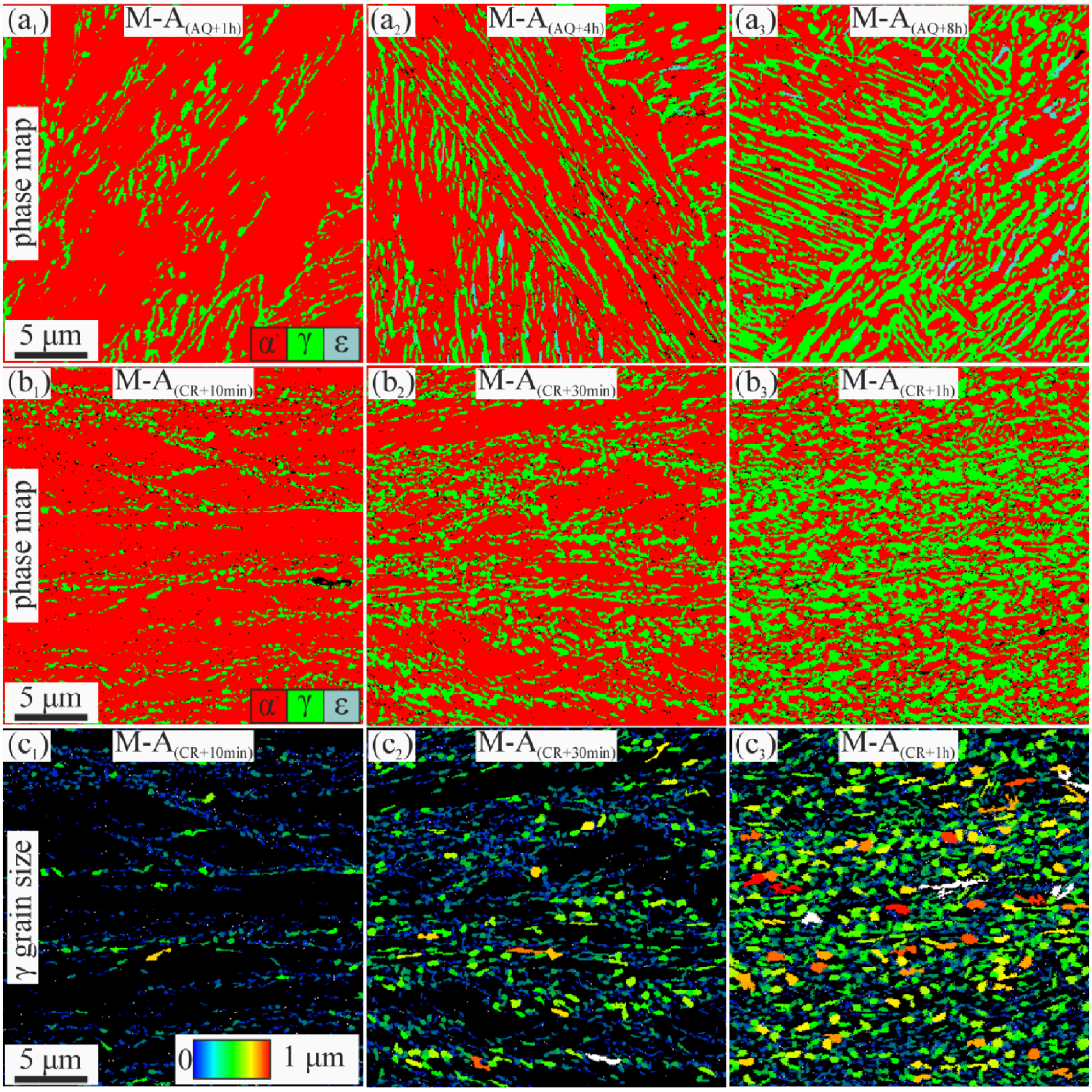

Figure 8.3: (a) Phase map for (1) M-A$_{(AQ+1h)}$; (2) M-A$_{(AQ+4h)}$; (3) M-A$_{(AQ+8h)}$. (b) Phase map and (c) γ grain size map for (1) M-A$_{(CR+10min)}$; (2) M-A$_{(CR+30min)}$; (3) M-A$_{(CR+1h)}$, as characterized by EBSD measurements. M-A$_{(AQ+1h)}$: 600 °C 1 h annealed as-quenched α' martensite; M-A$_{(AQ+4h)}$: 600 °C 4 h annealed as-quenched α' martensite; M-A$_{(AQ+8h)}$: 600 °C 8 h annealed as-quenched α' martensite; M-A$_{(CR+10min)}$: 600 °C 10 min annealed cold-rolled α' martensite; M-A$_{(CR+30min)}$: 600 °C 30 min annealed cold-rolled α' martensite; M-A$_{(CR+1h)}$: 600 °C 1 h annealed cold-rolled α' martensite.

The influence of pre-straining of martensite on the γ reversion kinetics is shown in Figure 8.4a. It can be seen that M$_{(CR)}$ exhibits significantly higher γ reversion kinetics than M$_{(AQ)}$, i.e. higher γ fraction is observed for the former after the same annealing period at 600 °C. The size distribution of γ grains in sample M-A$_{(CR+1h)}$ is also quantified and plotted together with the width

distribution of γ nano-films in sample M-$A_{(AQ+8h)}$ in Figure 8.4b. In sample M-$A_{(AQ+8h)}$, majority of the γ grains have widths smaller than 0.3 μm (green curve in Figure 8.4b). In contrast, sample M-$A_{(CR+1h)}$ exhibits a broader γ grain size distribution (black curve in Figure 8.4b). Thus, as aimed, a broader size distribution of γ grains is successfully developed from cold-rolled martensite.

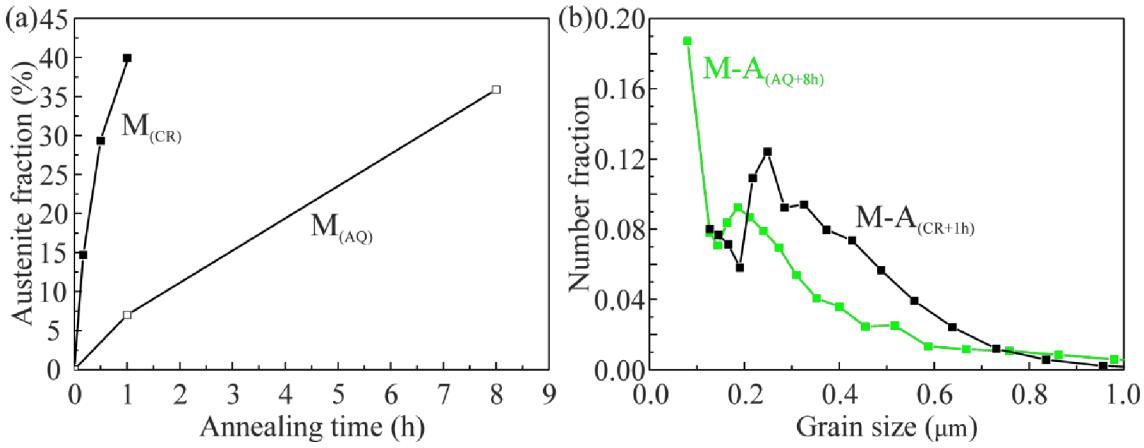

Figure 8.4: (a) Evolution of reverted γ fraction during 600 °C annealing of $M_{(CR)}$ and $M_{(AQ)}$. (b) Size distribution of reverted γ grains for M-$A_{(AQ+8h)}$ and M-$A_{(CR+1h)}$. $M_{(AQ)}$: as-quenched martensite; $M_{(CR)}$: cold-rolled martensite; M-$A_{(AQ+8h)}$: 600 °C 8 h annealed as-quenched α' martensite; M-$A_{(CR+1h)}$: 600 °C 1 h annealed cold-rolled α' martensite.

8.2.2 Mechanical response

To assess whether the successfully realized microstructure design strategy positively enhances the mechanical properties as planned, the mechanical properties of sample M-$A_{(CR+1h)}$ are compared with sample M-$A_{(AQ+8h)}$ in Figure 8.5. Sample M-$A_{(CR+1h)}$ exhibits a yield stress $\sigma_{0.2}$ of 870 MPa, ultimate tensile stress of 1110 MPa, and uniform elongation of 17.1%, corresponding to 31% increase in $\sigma_{0.2}$, 23% increase in ultimate tensile stress and maintained uniform elongation comparing with sample M-$A_{(AQ+8h)}$ (Figure 8.5a). The DIC-based strain measurements also reveal that M-$A_{(AQ+8h)}$ and M-$A_{(CR+1h)}$ exhibit comparable post-necking deformation capability, i.e. with

similar amount of accumulated strain between stage of strain localization and last stage prior to failure.

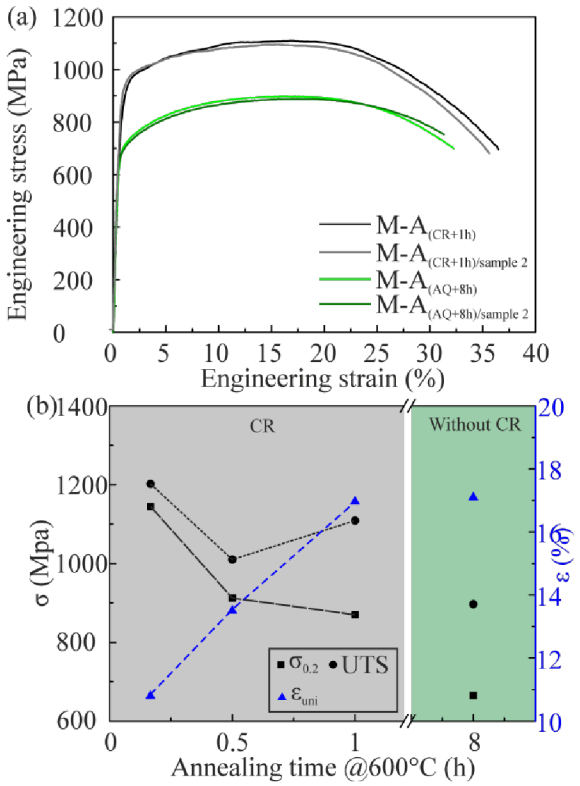

Figure 8.5: (a) Engineering stress strain curve for M-A$_{(AQ+8h)}$ and M-A$_{(CR+1h)}$; (b) Mechanical property summary of sample M-A$_{(AQ+8h)}$, sample M-A$_{(CR+10min)}$, sample M-A$_{(CR+30min)}$ and sample M-A$_{(CR+1h)}$. M-A$_{(AQ+8h)}$: 600 °C 8 h annealed as-quenched α' martensite; M-A$_{(CR+10min)}$: 600 °C 10 min annealed cold-rolled α' martensite; M-A$_{(CR+30min)}$: 600 °C 30 min annealed cold-rolled α' martensite; M-A$_{(CR+1h)}$: 600 °C 1 h annealed cold-rolled α' martensite.

The mechanical properties of sample M-A$_{(CR+10min)}$, M-A$_{(CR+30min)}$, M-A$_{(CR+1h)}$ and M-A$_{(AQ+8h)}$ are summarized in Figure 8.5b. It is clear that after 1 h annealing of cold-rolled martensite, sample M-A$_{(CR+1h)}$ exhibits improved mechanical properties compared to the 8 h annealed as-quenched martensite (sample M-A$_{(AQ+8h)}$). Thus, the proposed strategy is proven to be effective.

The strain hardening behaviors for M-A$_{(AQ+8h)}$ and M-A$_{(CR+1h)}$ are shown in Figure 8.6a. It is clear that M-A$_{(CR+1h)}$ (black curve in Figure 8.6a) exhibits an enhanced strain hardening behavior

during later stage of deformation, i.e. above ε=0.07. Based on the strain hardening behavior in Figure 8.6a, the deformation process of sample M-$A_{(CR+1h)}$ is divided into three stages, namely stage i-early uniform (ε<0.07), stage ii-late uniform (0.07<ε<0.14), and stage iii-post-necking deformation stages (ε>0.14). To indicate the deformation and phase transformation behaviors of γ grains within regimes from Figure 8.6a, two datasets are plotted in Figure 8.6b: (i) the kernel average misorientation (KAM) in γ (red data points); and (ii) the γ fraction (blue data points). KAM is the average misorientation of all neighboring points with respect to a given kernel (here 2nd neighbor, all points in kernel) [196]. To exclude the influence from neighboring grains or boundaries, misorientations higher than 5° are excluded from the calculations. Here KAM is used as an index for assessing accumulated plasticity in deformed γ grains.

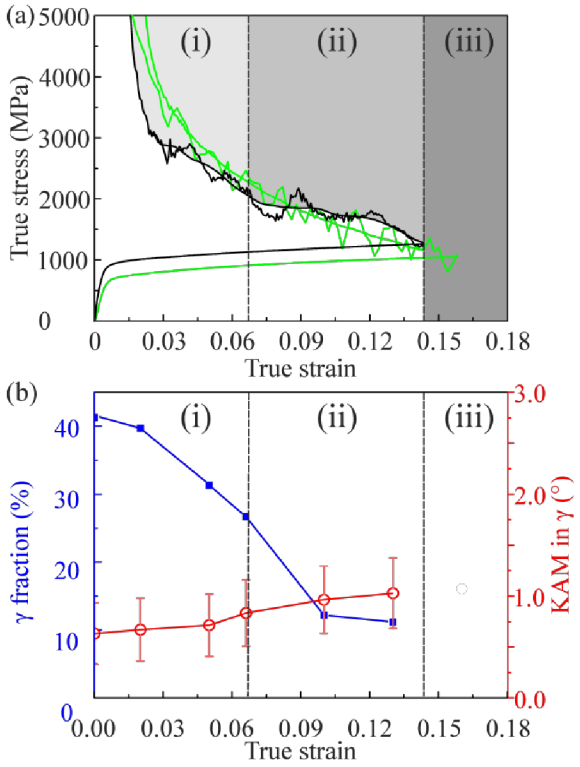

Figure 8.6: (a) True stress strain curve and strain hardening curve for M-$A_{(AQ+8h)}$ and M-$A_{(CR+1h)}$; (b) evolution of γ fraction (blue data points) and kernel average misorientation (KAM) in γ (red data points) during deformation of M-$A_{(CR+1h)}$, as measured by EBSD. M-$A_{(AQ+8h)}$: 600 °C 8 h annealed as-quenched α' martensite; M-$A_{(CR+1h)}$: 600 °C 1 h annealed cold-rolled α' martensite.

8.2.3 Deformation micro-mechanisms

To understand the deformation micro-mechanisms associated with the new strategy, the microstructure evolutions during deformation of M-$A_{(CR+1h)}$ are investigated next in detail.

The internal structures of α' martensite and reverted γ in M-$A_{(AQ+8h)}$ were systematically characterized in detail by EBSD, TEM, ECCI and synchrotron X-Ray diffraction (SXRD) analysis (Chapter 4, Chapter 7). In M-$A_{(AQ+8h)}$, α' martensite is characterized by dislocations and nano-precipitates, while reverted γ grains are precipitate-free and contain minor amounts of stacking faults (SFs) prior to deformation. Based on the similarity of sub-structural features and deformation mechanisms in M-$A_{(CR+1h)}$, the characterization of M-$A_{(CR+1h)}$ is carried out mainly by ECCI, supported by EBSD based KAM and deformation texture analysis [10]. The latter two are especially useful indicators since deformation in γ (i) proceeds via multiplication of defect density and thus increased lattice curvature due to deformation would be reflected as an increase in KAM value; and (ii) is accommodated by motion of partial dislocations, i.e. with 1/6<11-2>{111} slip systems, leading to a gradual build-up of {111}//TA (tensile axis) texture.

The analysis start from the undeformed state, where the microstructure of sample M-$A_{(CR+1h)}$ consists of α' martensite (phase in red) and reverted γ grains (phase in green), as shown by EBSD phase map in Figure 8.7a_1. Reverted γ grains in M-$A_{(CR+1h)}$, as highlighted by yellow outlines in Figure 8.7a_2 and a_3, contains minor amount of stacking faults (SFs) and does not inherit stored

[10] Due to the same annealing temperature applied to obtain M-$A_{(AQ+8h)}$ and M-$A_{(CR+1h)}$, i.e. 600 °C, it is expected that reverted γ grains in both samples assume the same chemical composition (Chapter 7), e.g. similar stacking fault energy (SFE) [184], [186]. And thus deformation of γ is expected to take place via activation of similar mechanisms, e.g. by formation of SFs, mechanical twinning and deformation-induced phase transformation.

dislocations from cold-rolled martensite. α' martensite matrix is characterized by precipitates and dislocations (Figure 8.7a_3).

During stage i-early uniform deformation regime ($\varepsilon<0.07$), the strain hardening rate decreases after yielding (Figure 8.6a). ~15% γ grains transform into α' martensite and remaining γ grains exhibit slight increase in KAM value up to $\varepsilon=0.05$ (Figure 8.6b). Reverted γ grains, as highlighted by yellow outlines, are deformed by motion of partial dislocations and formation of SFs (Figure 8.7b_2-b_3). SFs within some γ grains are observed to be aligned along different orientations and thus divide γ grains into distinct counterparts.

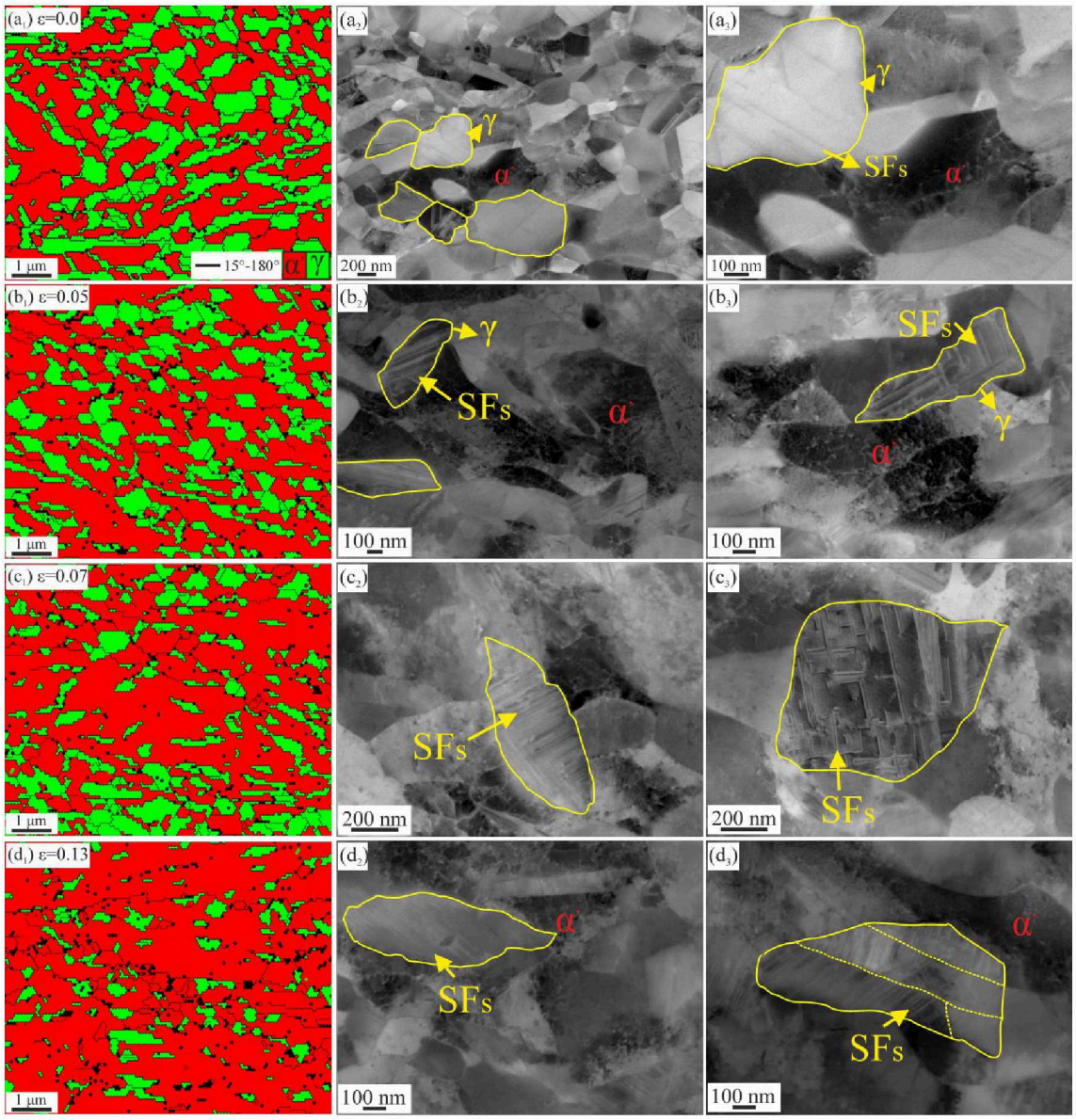

Figure 8.7: Microstructure evolution during deformation of sample M-A$_{(CR+1h)}$ at (a) ε=0; (b) ε=0.05; (c) ε=0.07; (d) ε=0.13, as characterized by (1) EBSD phase map; (2, 3) ECCI. M-A$_{(CR+1h)}$: 600 °C 1 h annealed cold-rolled α' martensite.

Stage ii-late uniform deformation regime is characterized by the appearance of a strain hardening plateau from ε=0.07 to ε=0.12, and then a decrease in strain hardening rate up to ε=0.14 (Figure 8.6a). During stage ii, ~14.5% γ transforms into α' martensite and a continuous increase in KAM value in remaining γ grains is observed (Figure 8.6b). Thus accompanying the significant activation of phase transformation, remaining γ grains also exhibit pronounced plasticity. In fact,

at the onset of the strain hardening plateau, i.e. ε=0.07 (Figure 8.7c_2-c_3), γ grains are observed to contain denser SFs arrangements than at ε=0.05 (Figure 8.7b_2-b_3). This is also in accordance with the built-up of {111}//TA texture component in remaining γ grains after straining to ε=0.07 (Figure 8.8a_1-a_3). The {111}//TA texture in γ is maintained with further straining (Figure 8.8a_4). Meanwhile martensite always maintains the {110}//TA rolling texture during tensile deformation (Figure 8.8b_1-b_4). Within γ grains, a size-dependent deformation behavior in terms of in-grain structure is observed (Figure 8.7c_2, c_3). On one hand, small γ grains tend to be deformed as a unit (Figure 8.7c_2) while larger γ grains are generally subdivided into segments with several sets of SFs structure (Figure 8.7c_3). On the other hand, smaller γ grains exhibit an overall denser arrangement of SFs than larger γ grains, e.g. comparing Figure 8.7c_3 with Figure 8.7c_2. This size-dependent deformation behavior evolves with further straining. At ε=0.13, most small γ grains, in which no SFs can be resolved anymore, transformed into α' martensite (Figure 8.7d_2). On the other hand, large γ grain is observed to be densely covered by SFs in each segment (Figure 8.7d_3). Moreover, the in-grain contrast within one large γ grain indicates that each part has undergone deformation or also phase transformation individually (Figure 8.7d_3). The partial transformation behavior of large γ grains in M-$A_{(CR+1h)}$, i.e. the observation that the large γ grain is first split into sub-grains and then each sub-grain transform individually, is in consistence with the observations in M-$A_{(AQ+8h)}$ (Chapter 7).

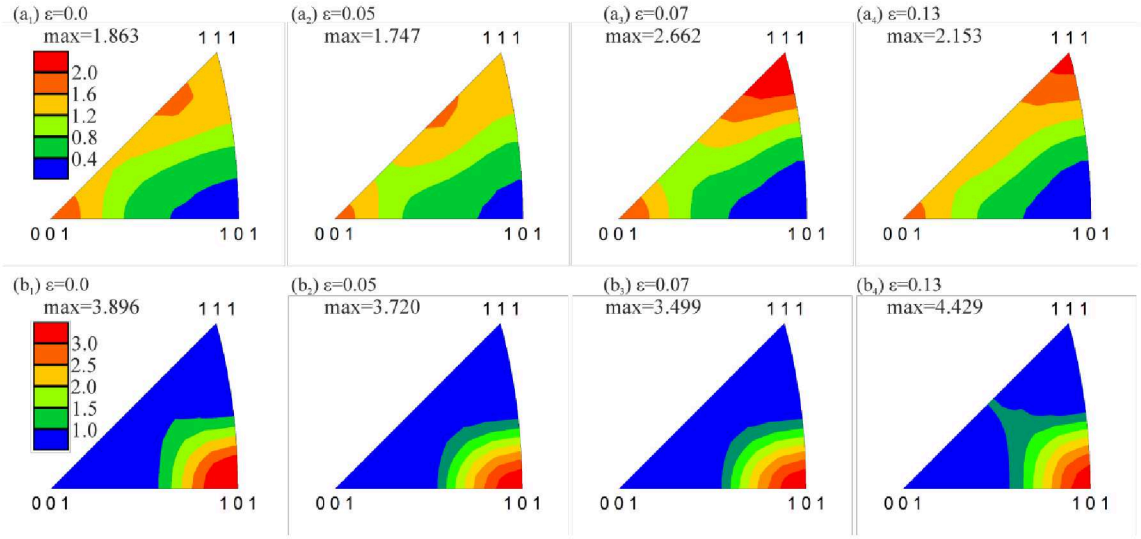

Figure 8.8: Evolution of IPF texture with respect to tensile axis for (a) γ; and (b) martensite at (1) ε=0; (2) ε=0.05; (3) ε=0.07; (4) ε=0.13, during deformation of M-A$_{(CR+1h)}$. M-A$_{(CR+1h)}$: 600 °C 1 h annealed cold-rolled α' martensite.

8.3 Discussion

Without cold-rolling, the initial microstructure prior to reversion is as-quenched martensite, which consists of martensite packets, blocks and laths (Figure 8.1a$_1$-a$_2$) (Chapter 4). These characteristic martensite boundaries do not exist in the microstructure anymore after cold rolling (~70% thickness reduction). In contrast, cold-rolled martensite contains numerous deformation boundaries in the microstructure, since cold rolling is accommodated in the microstructure by multiplication and rearrangement of dislocations into different sub-structures (Figure 8.1b$_1$-b$_2$) [192]. Comparing to the as-quenched martensite, which mainly contains boundaries with either high angle misorientation (above 45°) or low angle misorientation (below 15°), cold-rolled martensite contains a continuous distribution of all boundaries in terms of their misorientation angle (Figure 8.2).

The difference in distribution of martensite boundaries subsequently lead to a different reversion processes in as-quenched martensite and cold-rolled martensite (Figure 8.3). Comparing with low angle boundaries, reverted γ grains are preferentially formed along high angle boundaries during

annealing at 600 °C, indicating shorter incubation time for γ along high angle martensite boundaries (Figure 8.3a_1-a_3, Figure 8.3b_1-b_3). As reported by Raabe et al., the reversion of martensite to γ takes place via two steps: (i) elemental segregation into martensite boundaries and (ii) transformation of these decorated boundaries into γ phase via nucleation and growth processes [15]. The tendency of elemental segregation towards a boundary is highly dependent on the boundary character, e.g. boundaries with high angle misorientations exhibit higher boundary enrichment factor than boundaries with lower angle misorientations [47], [197]. Even in the case of equally decorated boundaries, e.g. boundaries assume identical chemical composition, the difference in boundary character would also subsequently lead to different γ nucleation barrier therein, e.g. boundaries with higher angle misorientations (higher martensite/martensite interfacial energy) tend to decrease the γ nucleation barrier. Thus boundaries with higher angle misorientations promote both higher tendency of elemental segregation and lower γ nucleation barrier. Due to the existence of only high angle martensite boundaries (above 45°) and low angle martensite boundaries (below 15°), relatively longer annealing time at 600 °C is required to form nano-films of interlath γ along majority of lath martensite boundaries, e.g. 8 h (Figure 8.3a_3). In contrast, due to the continuous distribution of boundaries in cold-rolled martensite, a continuous nucleation and growth process is obtained, as indicated by the evolution of γ grain size distribution in cold-rolled martensite (Figure 8.3c_1-c_3) and quantitatively shown for sample M-$A_{(AQ+8h)}$ and M-$A_{(CR+1h)}$ (Figure 8.4b). Eventually, a dispersed size distribution of γ grains is obtained in sample M-$A_{(CR+1h)}$ (Figure 8.3c_3, Figure 8.4b).

The growth of γ nucleus is accompanied by elemental partitioning from martensite, and thus is controlled by the diffusion rate of corresponding elements across the microstructure, e.g. via stored dislocations in martensite (Chapter 4). Cold rolling (~70% thickness reduction)

significantly results in high stored dislocation density [195], [198], [199] and a faster growth rate of reverted γ in cold-rolled martensite than as-quenched martensite, e.g. comparing the γ grain size in sample M-$A_{(CR+1h)}$ (Figure 8.3b_3) with M-$A_{(AQ+1h)}$ (Figure 8.3a_1). Due to the existence of high density martensite boundaries and high stored dislocation density, the combined high γ nucleation rate and growth kinetics in cold-rolled martensite lead to an accelerated reversion kinetics than as-quenched martensite (Figure 8.4a).

To achieve the goal of enhancing overall mechanical properties via the current strategy, it is also essential to control the structure of martensite. In this context, possible recrystallization of martensite during annealing due to the stored high strain energy in cold-rolled martensite is undesired. Recrystallization in deformed microstructure is carried out by formation of new strain-free grains and their growth to consume other deformed or recovered microstructure [200]. Thus, occurrence of recrystallization in cold-rolled martensite during annealing would lead to uncompensated loss of strength in martensite. In relevant works on cold-rolled medium Mn steels, the occurrence of recrystallization in martensite leads to the formation of 'soft' ferrite during the reversion treatment [201]–[203]. During tensile testing, the yielding of 'soft' and almost dislocation-free ferrite leads to a discontinuous yielding behavior and appearance of Lüders band on the tensile specimen surface [201]–[203]. In the current cold-rolled martensite, recrystallization of martensite does not take place during the 600 °C annealing (Figure 8.7a_1-a_2). The suppression of recrystallization during 600 °C isothermal annealing of the current cold-rolled martensite can be attributed to two reasons. On one hand, as a result of the small elastic misfit between the intermetallic particles and martensite, a high homogeneous nucleation rate exists for these particles, and these precipitates in turn restrict the motion and interaction of dislocations in the martensite [46]. On the other hand, the nucleation of reverted γ along boundaries hinder the motion of boundaries, and the growth of strain-free γ grains lower the stored strain energy in the

deformed structure, thus consuming prerequisites for recrystallization [204]. As a result, recrystallization of martensite is suppressed and considerable amount of dislocations are preserved in the martensite after 600 °C isothermal annealing.

Compared to M-$A_{(AQ+8h)}$, M-$A_{(CR+1h)}$ exhibits a higher yield stress $\sigma_{0.2}$, ultimate tensile stress UTS and maintained uniform elongation (Figure 8.5a-c). The yielding of martensite-reverted γ microstructure occurs via yielding of 'soft' phase γ, which is influenced by γ fraction, the deformation behavior and stability, etc. [205]. Sample M-$A_{(AQ+8h)}$ and sample M-$A_{(CR+1h)}$ contain similar amount of γ, e.g. 37% for the former and 42% for the latter. For both cases, it is observed that γ is deformed by formation of SFs prior to deformation induced phase transformation (Figure 8.7) (Chapter 4, Chapter 7). As reported by Sugimoto et al., the stability of austenite is also influenced by the hydrostatic pressure from the surrounding second phase, e.g. a lower hydrostatic pressure would be exerted on retained austenite from ferrite than from bainite [153]. Thus, higher hydrostatic pressure on γ is expected in sample M-$A_{(CR+1h)}$ than in sample M-$A_{(AQ+8h)}$, due to (i) the highly elastic strained lattice of cold-rolled martensite; and (ii) higher stored dislocation density after shorter time isothermal annealing. Therefore, due to the substantial 'shielding' effect from the surrounding martensite, higher external stress is required in sample M-$A_{(CR+1h)}$ to initiate deformation of γ grains, i.e. yield stress is higher in sample M-$A_{(CR+1h)}$.

The reasoning for enhanced ultimate tensile stress UTS, uniform elongation and strain hardening behaviors in sample M-$A_{(CR+1h)}$ are interlinked with each and are resulted from the interplay between the deformation and phase transformation processes in the microstructure. In the following, these processes will be analyzed in detail.

The strain hardening behavior of M-$A_{(CR+1h)}$ is determined by the individual hardening behavior of martensite and γ, and the strain partitioning behavior therein. The hardening of martensite arises from multiplication of dislocations and their interaction with precipitates, etc. The hardening of reverted γ mainly consists of two parts, namely strain hardening due to formation of SFs, and phase transformation into martensite. In sample M-$A_{(AQ+8h)}$, it is observed that martensite enter plasticity regime during late stage of uniform deformation, e.g. ε>0.05. Here due to the fact that martensite in M-$A_{(CR+1h)}$ assumes much higher strength, it is expected that the contribution of martensite to strain hardening during early uniform deformation regime (stage i) is not significant [202], [206], [207].

At undeformed state, the microstructure of M-$A_{(CR+1h)}$ consists of α' martensite and reverted γ (~42% volume fraction) (Figure 8.7a_1). Preceding transformation into α' martensite, γ grains are deformed by motion of partial dislocations and formation of SFs (Figure 8.7b_1-b_2).

During stage i, ~15% γ transforms into α' martensite (Figure 8.5d) and remaining γ grains are only slightly deformed (Figure 8.7b_2-b_3), e.g. limited strengthening effect from accumulated SFs within remaining γ grains is present. The significant transformation of γ alone cannot cease the continuous decrease in strain hardening rate after yielding during stage i (Figure 8.6a).

During stage ii, in addition to the significant amount of phase transformation, remaining γ grains are also profoundly deformed, thus being able to terminate the decrease in strain hardening rate and leads to the formation of a strain hardening plateau (Figure 8.6a-b). The appearance of the strain hardening plateau is attributed to the dynamic strain partitioning process which arises from two factors (i) orientation relationship between martensite and γ; (ii) size effect of γ. On one hand, as a result of plastic deformation, a {111}//TA texture is gradually built-up, e.g. from ε=0, to ε=0.05, and to ε=0.07 (Figure 8.8a_1-a_3). Since martensite exhibits a {110}//TA rolling texture

(Figure 8.8b_1-b_4), a gradual built-up of {111}//TA texture in γ implies a progressive alignment of slip systems between martensite and γ, and thus an easier transfer of slip/plasticity from γ to martensite, e.g. improved deformation compatibility across phase boundary with deformation [162], [208]. Thus, from ε=0.07 onwards, the contribution of martensite plasticity to the overall strain hardening becomes significant. On the other hand, a size-dependent deformation and transformation behavior exists within γ grains. While small γ grains tend to be deformed as a unit, large grains are preferentially divided into sub-grains and each sub-grain is deformed in an independent manner. At the same strain level, small grains contain denser SFs than larger grains. Since SFs in deformed γ grains act as nucleation sites for α' martensite, deformed γ grains with sufficient accumulation of SFs would transform to α' martensite with further straining (Chapter 7) [177], [178]. As a result, small γ grains transform into martensite after relatively small amount of deformation and larger γ grains undergo partial phase transformation in a stepwise manner (Figure 8.7b_2-b_3, c_2-c_3). The size effect on mechanical stability of γ is consistent with that in M-$A_{(AQ+8h)}$ (Chapter 7). In M-$A_{(AQ+8h)}$, due to the Hall-Petch effect, twinning is preferentially initiated in larger grains (0.3-4 μm^2), i.e. with lower twinning stress. As a result of the competition between size-dependent TWIP and TRIP effect, larger γ grains (0.3-4 μm^2) exhibit higher overall mechanical stability than smaller γ grains (0.1-0.3 μm^2). The formation of nano-twin boundaries in γ is also captured in M-$A_{(CR+1h)}$, e.g. as indicated by dashed lines in Figure 8.7d_3. Thus, it is expected that γ grains would exhibit higher overall mechanical stability in M-$A_{(AQ+8h)}$, e.g. γ grains with a dispersed and larger overall grain size. Due to the formation of nano-twin boundaries and the resulted partial transformation behavior of large grains, the majority of remaining γ grains are actually pertaining to 'initial' large γ grains at ε=0.07 (Figure 8.7c_1) and ε=0.13 (Figure 8.7d_1). Thus, the enhanced dynamic strain partitioning behavior due to the orientation relationship and size effect gives rise to an enhanced strain hardening capacity (Figure

8.4b, Figure 8.6a), and hence increased ultimate tensile stress and maintained uniform elongation in sample M-$A_{(CR+1h)}$. In addition, a high damage resistance is also preserved in sample M-$A_{(CR+1h)}$, e.g. comparable post-necking elongation as in sample M-$A_{(AQ+8h)}$. The high damage resistance is due to the high density of phase interfaces, i.e. deformation-induced martensite/tempered martensite interface, which act as high energy path for void nucleation, growth and coalescence processes (Chapter 4).

Chapter 9 Conclusions and Outlook

In this work, nanolaminate TRIP-TWIP martensitic matrix steels are designed and characterized. The main conclusions are as follows:

- The proposed alloy design concept of developing nanolaminate martensite-reverted austenite microstructure is effective in designing ductile martensitic steels, as shown here with the Fe-9Mn-3Ni-1.4Al-0.01C (mass %) steel.
- Under the guidance of thermodynamic phase transformation and diffusion simulations the morphology and constitution of the nanolaminate microstructure can be well-controlled.
- Compared to the as-quenched state, the nanolaminate martensite-reverted austenite microstructure after 600 °C 8 h reversion treatment exhibit consistent increase in ductility and toughness (uniform elongation of 17.1 %, DBTT of -76 °C), without sacrificing strength (yield stress of 665 MPa and ultimate tensile stress of 900 MPa).
- The improvements in properties are based on enhanced strain hardening and damage resistance in these alloys, which in turn arise from the presence of various deformation mechanisms (slip, phase transformation, mechanical twinning), and a high interface density.
- Due to these deformation characteristics and the presence of austenite as potential hydrogen traps, austenite reversion is proposed as a method to provide lath martensite steels with higher resistance to hydrogen embrittlement. The strategy is effective, leading to 4-fold increase in ductility with the presence of hydrogen, however, future work is needed to further exploit the potential of this strategy.
- It is observed in these alloys that a size dependence of mechanical twinning causes an unexpected size dependence of mechanically induced phase transformation, when other controlling factors (composition, morphology, orientation) have identical influence.

- To further benefit from size effect, nucleation barrier for austenite is widened in martensite through cold-rolling. A dispersed size distribution of austenite grains is successfully developed from cold-rolled martensite and further enhance mechanical properties is achieved. Besides dispersed deformation and transformation processes associated with size distribution, promoted slip transfer between martensite and austenite due to development of texture also contribute to the improvement in strain hardening behavior.
- Benefitting from the conservation of chemical composition during martensitic transformation and the maraging effect, it is shown that with post-deformation annealing, both the microstructure and the mechanical properties are successfully retrieved in this system. Thus, a non-autonomic healing concept is proposed and validated.

The proposed concept can be considered as a generalized alloy design concept, which is applicable to other alloy systems as long as an initially ‘soft’ metastable phase is introduced into a ‘hard’ phase in a fine scale. As observed here, this would essentially lead to a dynamic strain partitioning process originated from the presence of the metastable phase. This enables the deformation capacity of hard phase to be consumed in a conservative manner, and a high damage resistance. Size effects can be beneficial in alloy design to disperse different deformation mechanisms through different deformation stages, promoting resistance to strain localization and failure. In addition, further improvements in resistance to hydrogen embrittlement lies in designing austenite grains with a wider dispersed stability.

Bibliography

[1] S. Morito, H. Yoshida, T. Maki, and X. Huang, "Effect of block size on the strength of lath martensite in low carbon steels," *Mater. Sci. Eng. A*, vol. 438–440, pp. 237–240, Nov. 2006.

[2] G. Krauss, *Hardenability Concepts with Applications to Steel*. Metallurgical Society of AIME, 1978.

[3] K. Nakashima, Y. Fujimura, T. Tsuchiyama, and S. Takaki, "Effect of Carbon on Work Hardening Behavior of 18%Ni Martensitic Steel," *Mater. Sci. Forum*, vol. 539–543, pp. 4783–4788, 2007.

[4] H. Yang and H. Bhadeshia, "Austenite grain size and the martensite-start temperature," *Scr. Mater.*, vol. 60, no. 7, pp. 493–495, Apr. 2009.

[5] P. J. Brofamn and G. S. Ansell, "On the Effect of Fine Grain size on the Ms temperature in Fe-27Ni-0.025C alloys," *Metall. Trans. A*, vol. 14A, pp. 1929–1931, 1983.

[6] M. Miller and P. Beaven, "An atom probe study of the aging of iron-nickel-carbon martensite," *Metall. Trans. A*, vol. 14A, pp. 1021–1024, 1983.

[7] S. Nagakura, Y. Hirotsu, and M. Kusunoki, "Crystallographic study of the tempering of martensitic carbon steel by electron microscopy and diffraction," *Metall. Trans. A*, vol. 14A, pp. 1025–1031, 1983.

[8] S. Nambu, M. Michiuchi, Y. Ishimoto, K. Asakura, J. Inoue, and T. Koseki, "Transition in deformation behavior of martensitic steel during large deformation under uniaxial tensile loading," *Scr. Mater.*, vol. 60, no. 4, pp. 221–224, Feb. 2009.

[9] C. Jeong, T. Oya, and J. Yanagimoto, "Analysis of fracture behavior and stress–strain distribution of martensite/austenite multilayered metallic sheet," *J. Mater. Process. Technol.*, vol. 213, no. 4, pp. 614–620, Apr. 2013.

[10] J. Inoue, S. Nambu, Y. Ishimoto, and T. Koseki, "Fracture elongation of brittle/ductile multilayered steel composites with a strong interface," *Scr. Mater.*, vol. 59, no. 10, pp. 1055–1058, Nov. 2008.

[11] F. Carreño, J. Chao, M. Pozuelo, and O. a. Ruano, "Microstructure and fracture properties of an ultrahigh carbon steel–mild steel laminated composite," *Scr. Mater.*, vol. 48, no. 8, pp. 1135–1140, Apr. 2003.

[12] J. Speer, D. K. Matlock, B. C. De Cooman, and J. G. Schroth, "Carbon partitioning into austenite after martensite transformation," *Acta Mater.*, vol. 51, no. 9, pp. 2611–2622, May 2003.

[13] J. G. Speer, D. V. Edmonds, F. C. Rizzo, and D. K. Matlock, "Partitioning of carbon from supersaturated plates of ferrite, with application to steel processing and fundamentals of the bainite transformation," *Curr. Opin. Solid State Mater. Sci.*, vol. 8, no. 3–4, pp. 219–237, Jun. 2004.

[14] S. A. Mujahid and H. K. D. H. Bhadeshia, "Partitioning of carbon from supersaturated ferrite plates," *Acta Metall. Mater.*, vol. 40, no. 2, pp. 389–396, 1992.

[15] D. Raabe, S. Sandlöbes, J. Millán, D. Ponge, H. Assadi, M. Herbig, and P.-P. Choi, "Segregation engineering enables nanoscale martensite to austenite phase transformation at

grain boundaries: A pathway to ductile martensite," *Acta Mater.*, vol. 61, no. 16, pp. 6132–6152, Sep. 2013.

[16] D. Raabe, D. Ponge, O. Dmitrieva, and B. Sander, "Designing Ultrahigh Strength Steels with Good Ductility by Combining Transformation Induced Plasticity and Martensite Aging," *Adv. Eng. Mater.*, vol. 11, no. 7, pp. 547–555, Jul. 2009.

[17] A. Kelly and M. Fine, "The strength of an alloy containing zones," *Acta Metall.*, vol. 5, no. July, pp. 365–367, 1957.

[18] E. Orowan, "Session III discussion," in *International Symposium on stresses in metals and alloys*, 1948, p. 451.

[19] S. Lee and B. C. De Cooman, "On the Selection of the Optimal Intercritical Annealing Temperature for Medium Mn TRIP Steel," *Metall. Mater. Trans. A*, vol. 44, no. 11, pp. 5018–5024, Jul. 2013.

[20] J.-M. Jang, S.-J. Kim, N. H. Kang, K.-M. Cho, and D.-W. Suh, "Effects of annealing conditions on microstructure and mechanical properties of low carbon, manganese transformation-induced plasticity steel," *Met. Mater. Int.*, vol. 15, no. 6, pp. 909–916, Dec. 2009.

[21] J. Hu, W. Cao, C. Wang, H. Dong, and J. Li, "Austenite stability and its effect on the ductility of the cold-rolled medium-Mn steel," *ISIJ Int.*, vol. 54, no. 8, pp. 1952–1957, 2014.

[22] Y. Tomota, H. Tokuda, Y. Adachi, M. Wakita, N. Minakawa, A. Moriai, and Y. Morii, "Tensile behavior of TRIP-aided multi-phase steels studied by in situ neutron diffraction," *Acta Mater.*, vol. 52, no. 20, pp. 5737–5745, Dec. 2004.

[23] P. J. Jacques, "Transformation-induced plasticity for high strength formable steels," *Curr. Opin. Solid State Mater. Sci.*, vol. 8, no. 3–4, pp. 259–265, Jun. 2004.

[24] P. J. Jacques, Q. Furnémont, F. Lani, T. Pardoen, and F. Delannay, "Multiscale mechanics of TRIP-assisted multiphase steels: I. Characterization and mechanical testing," *Acta Mater.*, vol. 55, no. 11, pp. 3681–3693, Jun. 2007.

[25] O. Muránsky, P. Šittner, J. Zrník, and E. C. Oliver, "In situ neutron diffraction investigation of the collaborative deformation–transformation mechanism in TRIP-assisted steels at room and elevated temperatures," *Acta Mater.*, vol. 56, no. 14, pp. 3367–3379, Aug. 2008.

[26] J. A. Ronevich, J. G. Speer, G. Krauss, and D. K. Matlock, "Improvement of the Hydrogen Microprint Technique on AHSS Steels," *Metallogr. Microstruct. Anal.*, vol. 1, no. 2, pp. 79–84, Jun. 2012.

[27] X. Zhu, W. Li, H. Zhao, and X. Jin, "Effects of cryogenic and tempered treatment on the hydrogen embrittlement susceptibility of TRIP-780 steels," *Int. J. Hydrogen Energy*, vol. 38, no. 25, pp. 10694–10703, Aug. 2013.

[28] M. Koyama, H. Springer, S. V. Merzlikin, K. Tsuzaki, E. Akiyama, and D. Raabe, "Hydrogen embrittlement associated with strain localization in a precipitation-hardened Fe–Mn–Al–C light weight austenitic steel," *Int. J. Hydrogen Energy*, vol. 39, no. 9, pp. 4634–4646, Mar. 2014.

[29] M. L. Martin, B. P. Somerday, R. O. Ritchie, P. Sofronis, and I. M. Robertson, "Hydrogen-

induced intergranular failure in nickel revisited," *Acta Mater.*, vol. 60, no. 6–7, pp. 2739–2745, Apr. 2012.

[30] T. Tsuchiyama, K. Tsuboi, S. Iwanaga, T. Masumura, A. Macadre, N. Nakada, and S. Takaki, "Suppression of hydrogen embrittlement by formation of a stable austenite layer in metastable austenitic stainless steel," *Scr. Mater.*, vol. 90–91, pp. 14–16, Nov. 2014.

[31] S. Frappart, X. Feaugas, J. Creus, F. Thebault, L. Delattre, and H. Marchebois, "Hydrogen solubility, diffusivity and trapping in a tempered Fe–C–Cr martensitic steel under various mechanical stress states," *Mater. Sci. Eng. A*, vol. 534, pp. 384–393, Feb. 2012.

[32] L. W. Tsay, W. C. Lee, R. K. Shiue, and J. K. Wu, "Notch tensile properties of laser-surface-annealed 17-4 PH stainless steel in hydrogen-related environments," *Corros. Sci.*, vol. 44, pp. 2101–2118, 2002.

[33] M.-M. Wang, C. C. Tasan, D. Ponge, A.-C. Dippel, and D. Raabe, "Nanolaminate transformation-induced plasticity–twinning-induced plasticity steel with dynamic strain partitioning and enhanced damage resistance," *Acta Mater.*, vol. 85, pp. 216–228, Feb. 2015.

[34] M.-M. Wang, C. Tasan, M. Koyama, D. Ponge, and D. Raabe, "Enhancing hydrogen embrittlement resistance of lath martensite by introducing nano-films of interlath austenite," *Metall. Mater. Trans. A*, pp. 0–5, 2015.

[35] M.-M. Wang, C. C. Tasan, D. Ponge, A. Kostka, and D. Raabe, "Smaller is less stable: Size effects on twinning vs. transformation of reverted austenite in TRIP-maraging steels," *Acta Mater.*, vol. 79, pp. 268–281, Oct. 2014.

[36] N. Nakada, R. Fukagawa, T. Tsuchiyama, S. Takaki, D. Ponge, and D. Raabe, "Inheritance of dislocations and crystallographic texture during martensitic reversion into austenite," *ISIJ Int.*, vol. 53, no. 7, pp. 1286–1288, 2013.

[37] N. Nakada, T. Tsuchiyama, S. Takaki, D. Ponge, and D. Raabe, "Transition from diffusive to displacive austenite reversion in low-alloy steel," *ISIJ Int.*, vol. 53, no. 12, pp. 2275–2277, 2013.

[38] P. Jacques, E. Girault, T. Catlin, N. Geerlofs, T. Kop, S. van der Zwaag, and F. Delannay, "Bainite transformation of low carbon Mn–Si TRIP-assisted multiphase steels: influence of silicon content on cementite precipitation and austenite retention," *Mater. Sci. Eng. A*, vol. 273–275, pp. 475–479, Dec. 1999.

[39] M. De Meyer, D. Vanderschueren, and B. De Cooman, "The influence of the substitution of Si by Al on the properties of cold rolled C-Mn-Si TRIP steels," *ISIJ Int.*, vol. 39, pp. 913–822, 1999.

[40] S. Traint, A. Pichler, K. Hauzenberger, P. Stiaszny, and E. Werner, "Influence of silicon, aluminium, phosphorus and copper on the phase transformations of low alloyed TRIP-steels," *Steel Res.*, vol. 73, no. 6–7, pp. 259–266, 2002.

[41] S. Zaefferer, J. Ohlert, and W. Bleck, "A study of microstructure, transformation mechanisms and correlation between microstructure and mechanical properties of a low alloyed TRIP steel," *Acta Mater.*, vol. 52, no. 9, pp. 2765–2778, May 2004.

[42] S. Lee, S.-J. Lee, and B. C. De Cooman, "Austenite stability of ultrafine-grained transformation-induced plasticity steel with Mn partitioning," *Scr. Mater.*, vol. 65, no. 3, pp. 225–228, Aug. 2011.

[43] A. Arlazarov, M. Gouné, O. Bouaziz, A. Hazotte, G. Petitgand, and P. Barges, "Evolution of microstructure and mechanical properties of medium Mn steels during double annealing," *Mater. Sci. Eng. A*, vol. 542, pp. 31–39, Apr. 2012.

[44] E. De Moor, D. K. Matlock, J. G. Speer, and M. J. Merwin, "Austenite stabilization through manganese enrichment," *Scr. Mater.*, vol. 64, no. 2, pp. 185–188, Jan. 2011.

[45] O. Dmitrieva, P. Choi, S. S. A. Gerstl, D. Ponge, and D. Raabe, "Pulsed-laser atom probe studies of a precipitation hardened maraging TRIP steel.," *Ultramicroscopy*, vol. 111, no. 6, pp. 623–7, May 2011.

[46] J. Millán, S. Sandlöbes, A. Al-Zubi, T. Hickel, P. Choi, J. Neugebauer, D. Ponge, and D. Raabe, "Designing heusler nanoprecipitates by elastic misfit stabilization in Fe–Mn maraging steels," *Acta Mater.*, vol. 76, pp. 94–105, Sep. 2014.

[47] O. Dmitrieva, D. Ponge, G. Inden, J. Millán, P. Choi, J. Sietsma, and D. Raabe, "Chemical gradients across phase boundaries between martensite and austenite in steel studied by atom probe tomography and simulation," *Acta Mater.*, vol. 59, no. 1, pp. 364–374, Jan. 2011.

[48] F. Moszner, A. S. Sologubenko, M. Schinhammer, C. Lerchbacher, A. C. Hänzi, H. Leitner, P. J. Uggowitzer, and J. F. Löffler, "Precipitation hardening of biodegradable Fe–Mn–Pd alloys," *Acta Mater.*, vol. 59, no. 3, pp. 981–991, Feb. 2011.

[49] D. Raabe, S. Sandlöbes, J. Millán, D. Ponge, H. Assadi, M. Herbig, and P.-P. Choi, "Segregation engineering enables nanoscale martensite to austenite phase transformation at grain boundaries: A pathway to ductile martensite," *Acta Mater.*, vol. 61, no. 16, pp. 6132–6152, Sep. 2013.

[50] F. Moszner, S. S. a. Gerstl, P. J. Uggowitzer, and J. F. Löffler, "Atomic-scale characterization of prior austenite grain boundaries in Fe–Mn-based maraging steel using site-specific atom probe tomography," *Acta Mater.*, vol. 73, pp. 215–226, 2014.

[51] J. Andersson, T. Helander, L. Hoeglund, P. Shi, and B. Sundman, "THERMO-CALC & DICTRA, Computational Tools For Materials Science J-O Andersson, Thomas Helander,Lars Hdghmd, Pingfang Shi, Bo Sundman," *Calphad*, vol. 26, no. 2, pp. 273–312, 2002.

[52] P. Shi, A. Engström, L. Höglund, B. Sundman, and J. Ågren, *Thermo-Calc and DICTRA Enhance Materials Design and Processing*, vol. 475–479. 2005.

[53] Q. Chen, A. Engström, L. Höglund, H. Strandlund, and B. Sundman, "Thermo-Calc Program Interface and Their Applications - Direct Insertion of Thermodynamic and Kinetic Data into Modelling of Materials Processing, Structure and Property," *Mater. Sci. Forum*, vol. 475–479, pp. 3145–3148, 2005.

[54] Z. Zhao, M. Ramesh, D. Raabe, A. M. Cuitiño, and R. Radovitzky, "Investigation of three-dimensional aspects of grain-scale plastic surface deformation of an aluminum oligocrystal," *Int. J. Plast.*, vol. 24, no. 12, pp. 2278–2297, Dec. 2008.

[55] J. Kang, Y. Ososkov, J. Embury, and D. Wilkinson, "Digital image correlation studies for microscopic strain distribution and damage in dual phase steels," *Scr. Mater.*, vol. 56, no. 11, pp. 999–1002, Jun. 2007.

[56] G. K. Tirumalasetty, M. A. van Huis, C. Kwakernaak, J. Sietsma, W. G. Sloof, and H. W. Zandbergen, "Deformation-induced austenite grain rotation and transformation in TRIP-

assisted steel," *Acta Mater.*, vol. 60, no. 3, pp. 1311–1321, Feb. 2012.

[57] S. Zaefferer and N.-N. Elhami, "Theory and application of electron channelling contrast imaging under controlled diffraction conditions," *Acta Mater.*, vol. 75, no. 154, pp. 20–50, Aug. 2014.

[58] A. P. Hammersley, S. O. Svensson, M. Hanfland, A. N. Fitch, and H. D., "Two-dimensional detector software: from real detector to idealised image or two-theta scan," *High Press. Res.*, vol. 14, pp. 235–248, 1996.

[59] L. Lutterotti, S. Matthies, and H.-R. Wenk, "MAUD: a friendly Java program for material analysis using diffraction," *Newsl. CPD*, vol. 21, pp. 14–15, 1999.

[60] D. P. Koistinen and R. E. Marburger, "A general equation prescribing the extent of the austenite-martensite transforamtion in pure iron-carbon alloys and plain carbon steels," *Acta Metall.*, vol. 7, pp. 59–60, 1959.

[61] K. W. Andrews, "Empirical foumular for the calculation of some transformation temperatures," *J. Iron Steel Inst.*, vol. 203, pp. 721–727, 1965.

[62] Y. Mine, K. Hirashita, H. Takashima, M. Matsuda, and K. Takashima, "Micro-tension behaviour of lath martensite structures of carbon steel," *Mater. Sci. Eng. A*, vol. 560, pp. 535–544, Jan. 2013.

[63] L. Velterop, R. Delhez, T. H. de Keijser, E. J. Mittemeijer, and D. Reefman, "X-ray diffraction analysis of stacking and twin faults in f.c.c. metals: a revision and allowance for texture and non-uniform fault probabilities," *J. Appl. Crystallogr.*, vol. 33, no. 2, pp. 296–306, Apr. 2000.

[64] T. Shintani and Y. Murata, "Evaluation of the dislocation density and dislocation character in cold rolled Type 304 steel determined by profile analysis of X-ray diffraction," *Acta Mater.*, vol. 59, no. 11, pp. 4314–4322, Jun. 2011.

[65] C. A. Schneider, W. S. Rasband, and K. W. Eliceiri, "NIH Image to ImageJ: 25 years of image analysis," *Nat. Methods*, vol. 9, no. 7, pp. 671–675, Jun. 2012.

[66] M. D. Abràmoff, P. J. Magalhães, and S. J. Ram, "Image Processing with ImageJ," *Biophotonics Int.*, 2004.

[67] B. Fultz and J. W. Morris, "The Mechanical Stability of Precipitated Austenite in 9Ni Steel," *Metall. Trans. A*, vol. 16A, pp. 2251–2256, 1985.

[68] J. I. Kim, H. J. A. E. Kim, and J. W. Morris, "The Role of the Constituent Phases in Determining the Low Temperature Toughness of 5 . 5Ni Cryogenic Steel," *Metall. Trans. A*, vol. 15A, pp. 2213–2219, 1984.

[69] M. Holscher, D. Raabe, and K. Luecke, "Relationship between rolling texture and shear textures in fcc and bcc metals," *Acta Metall. Mater.*, vol. 42, no. 3, pp. 879–886, 1994.

[70] D. Raabe, M. Hoelscher, M. Dubke, K.-H. Hanke, H. Pfelfer, and K. Luecke, "Texture development of strip cast ferritic stainless steel," *Steel Res.*, vol. 64, no. 7, pp. 359–363, 1993.

[71] R. F. Decker, J. T. Eash, and A. J. Goldman, "18% Nickel maraging steel," *Trans. ASM*, vol. 55, no. 1, 1962.

[72] W. Sha, A. Cerezo, and G. D. W. Smith, "Phase chemistry and precipitation reactions in maraging steels: Part IV. Discussion and conclusions," *Metall. Trans. A*, vol. 24, no. 6, pp.

1251–1256, 1993.

[73] C. Servant and N. Bouzid, “Influence of the increasing content of Mo on the precipitation phenomena occurring during tempering in the maraging alloy Fe-12Mn-9Co-5Mo,” *Acta Metall.*, vol. 36, no. 10, pp. 2771–2778, 1988.

[74] V. Vasudevan, S. Kim, and C. Wayman, “Precipitation reactions and strengthening behavior in 18 wt pct nickel maraging steels,” *Metall. Trans. A*, vol. 21, no. October, p. 2655, 1990.

[75] R. Tewari, S. Mazumder, I. S. Batra, G. K. Dey, and S. Banerjee, “Precipitation in 18 wt% Ni maraging steel of grade 350,” *Acta Mater.*, vol. 48, no. 5, pp. 1187–1200, Mar. 2000.

[76] R. F. Decker, *Source Book on Maraging Steels,*. ASM, Metals Park, OH, 1979.

[77] S. Morito, H. Tanaka, R. Konishi, T. Furuhara, and T. Maki, “The morphology and crystallography of lath martensite in Fe-C alloys,” *Acta Mater.*, vol. 51, no. 6, pp. 1789–1799, Apr. 2003.

[78] X. Z. Zhang and J. F. Knott, “Cleavage fracture in bainitic and martensitic microstructures,” *Acta Mater.*, vol. 47, no. 12, pp. 3483–3495, Sep. 1999.

[79] M. X. Zhang and P. M. Kelly, “Relationship between stress-induced martensitic transformation and impact toughness in low carbon austenitic steels,” *J. Mater. Sci.*, vol. 37, pp. 3603–3613, 2002.

[80] B. Hwang, T.-H. Lee, S.-J. Park, C.-S. Oh, and S.-J. Kim, “Correlation of austenite stability and ductile-to-brittle transition behavior of high-nitrogen 18Cr–10Mn austenitic steels,” *Mater. Sci. Eng. A*, vol. 528, no. 24, pp. 7257–7266, Sep. 2011.

[81] R. Wu, W. Li, S. Zhou, Y. Zhong, L. Wang, and X. Jin, “Effect of Retained Austenite on the Fracture Toughness of Quenching and Partitioning (Q&P)-Treated Sheet Steels,” *Metall. Mater. Trans. A*, Nov. 2013.

[82] A. Markfeld and A. Rosen, “The effect of reverted austenite on the plastic deformation of maraging steel,” *Mater. Sci. Eng.*, vol. 46, no. 2, pp. 151–157, Dec. 1980.

[83] I. Timokhina, P. Hodgson, and E. Pereloma, “Effect of microstructure on the stability of retained austenite in transformation-induced-plasticity steels,” *Metall. Mater.*, vol. 35A, pp. 2331–2341, 2004.

[84] R. Schnitzer, G. A. Zickler, E. Lach, H. Clemens, S. Zinner, T. Lippmann, and H. Leitner, “Influence of reverted austenite on static and dynamic mechanical properties of a PH 13-8 Mo maraging steel,” *Mater. Sci. Eng. A*, vol. 527, no. 7–8, pp. 2065–2070, Mar. 2010.

[85] W. Zhou, H. Guo, Z. Xie, X. Wang, and C. Shang, “High strength low-carbon alloyed steel with good ductility by combining the retained austenite and nano-sized precipitates,” *Mater. Sci. Eng. A*, vol. 587, pp. 365–371, Dec. 2013.

[86] R. D. K. Misra, P. Venkatsurya, K. M. Wu, and L. P. Karjalainen, “Ultrahigh strength martensite–austenite dual-phase steels with ultrafine structure: The response to indentation experiments,” *Mater. Sci. Eng. A*, vol. 560, pp. 693–699, Jan. 2013.

[87] X. D. Wang, Z. H. Guo, and Y. H. Rong, “Mechanism exploration of an ultrahigh strength steel by quenching–partitioning–tempering process,” *Mater. Sci. Eng. A*, vol. 529, pp. 35–40, Nov. 2011.

[88] K. Zhang, M. Zhang, Z. Guo, N. Chen, and Y. Rong, "A new effect of retained austenite on ductility enhancement in high-strength quenching–partitioning–tempering martensitic steel," *Mater. Sci. Eng. A*, vol. 528, no. 29–30, pp. 8486–8491, Nov. 2011.

[89] C. Herrera, D. Ponge, and D. Raabe, "Design of a novel Mn-based 1GPa duplex stainless TRIP steel with 60% ductility by a reduction of austenite stability," *Acta Mater.*, vol. 59, no. 11, pp. 4653–4664, Jun. 2011.

[90] M. Calcagnotto, Y. Adachi, D. Ponge, and D. Raabe, "Deformation and fracture mechanisms in fine- and ultrafine-grained ferrite/martensite dual-phase steels and the effect of aging," *Acta Mater.*, vol. 59, no. 2, pp. 658–670, Jan. 2011.

[91] X. Sun, K. S. Choi, A. Soulami, W. N. Liu, and M. A. Khaleel, "On key factors influencing ductile fractures of dual phase (DP) steels," *Mater. Sci. Eng. A*, vol. 526, no. 1–2, pp. 140–149, Nov. 2009.

[92] J. Kadkhodapour, A. Butz, and S. Ziaei Rad, "Mechanisms of void formation during tensile testing in a commercial, dual-phase steel," *Acta Mater.*, vol. 59, no. 7, pp. 2575–2588, Apr. 2011.

[93] S.-H. Choi, E.-Y. Kim, W. Woo, S. H. Han, and J. H. Kwak, "The effect of crystallographic orientation on the micromechanical deformation and failure behaviors of DP980 steel during uniaxial tension," *Int. J. Plast.*, vol. 45, pp. 85–102, Jun. 2013.

[94] C. C. Tasan, J. P. M. Hoefnagels, and M. G. D. Geers, "Microstructural banding effects clarified through micrographic digital image correlation," *Scr. Mater.*, vol. 62, no. 11, pp. 835–838, Jun. 2010.

[95] K. S. Choi, W. N. Liu, X. Sun, and M. A. Khaleel, "Influence of Martensite Mechanical Properties on Failure Mode and Ductility of Dual-Phase Steels," *Metall. Mater. Trans. A*, vol. 40, no. 4, pp. 796–809, Feb. 2009.

[96] P. J. Gibbs, B. C. De Cooman, D. W. Brown, B. Clausen, J. G. Schroth, M. J. Merwin, and D. K. Matlock, "Strain Partitioning in Ultra-Fine Grained Medium-Manganese Transformation Induced Plasticity Steel," *Mater. Sci. Eng. A*, Apr. 2014.

[97] S. Lee, S.-J. Lee, S. Santhosh Kumar, K. Lee, and B. C. D. Cooman, "Localized deformation in multiphase, ultra-fine-grained 6 Pct Mn transformation-induced plasticity steel," *Metall. Mater. Trans. A Phys. Metall. Mater. Sci.*, vol. 42, no. 12, pp. 3638–3651, 2011.

[98] F. G. Caballero and H. K. D. H. Bhadeshia, "Very strong bainite," *Curr. Opin. Solid State Mater. Sci.*, vol. 8, no. 3–4, pp. 251–257, Jun. 2004.

[99] S. S. Babu, S. Vogel, C. Garcia-Mateo, B. Clausen, L. Morales-Rivas, and F. G. Caballero, "Microstructure evolution during tensile deformation of a nanostructured bainitic steel," *Scr. Mater.*, vol. 69, no. 11–12, pp. 777–780, Dec. 2013.

[100] Y. J. Li, P. Choi, C. Borchers, S. Westerkamp, S. Goto, D. Raabe, and R. Kirchheim, "Atomic-scale mechanisms of deformation-induced cementite decomposition in pearlite," *Acta Mater.*, vol. 59, no. 10, pp. 3965–3977, Jun. 2011.

[101] Y. J. Li, P. Choi, S. Goto, C. Borchers, D. Raabe, and R. Kirchheim, "Evolution of strength and microstructure during annealing of heavily cold-drawn 6 . 3 GPa hypereutectoid pearlitic steel wire," *Acta Mater.*, vol. 60, pp. 4005–4016, 2012.

[102] J. A. Ronevich, B. C. Cooman, J. G. Speer, E. Moor, and D. K. Matlock, "Hydrogen

Effects in Prestrained Transformation Induced Plasticity Steel," *Metall. Mater. Trans. A*, vol. 43, no. 7, pp. 2293–2301, Mar. 2012.

[103] H. K. Birnbaum and P. Sofronis, "Hydrogen-enhanced localized plasticity—a mechanism for hydrogen-related fracture," *Mater. Sci. Eng. A*, vol. 176, no. 1–2, pp. 191–202, Mar. 1994.

[104]H. Vehoff and W. Rothe, "Gaseous hydrogen embrittlement in FeSi and Ni single crystals," *Acta Metall.*, vol. 31, no. 11, pp. 1781–1793, 1983.

[105] M. Nagumo, "Hydrogen related failure of steels – a new aspect," *Mater. Sci. Technol.*, vol. 20, no. 8, pp. 940–950, Aug. 2004.

[106] L. C. D. Fielding, E. J. Song, D. K. Han, H. K. D. H. Bhadeshia, and D.-W. Suh, "Hydrogen diffusion and the percolation of austenite in nanostructured bainitic steel," *Proc. R. Soc. A Math. Phys. Eng. Sci.*, vol. 470, no. 2168, pp. 1–18, May 2014.

[107] B. A. Szost, R. H. Vegter, and P. E. J. Rivera-Díaz-del-Castillo, "Hydrogen-Trapping Mechanisms in Nanostructured Steels," *Metall. Mater. Trans. A*, vol. 44, no. 10, pp. 4542–4550, May 2013.

[108] T. Michler and M. P. Balogh, "Hydrogen environment embrittlement of an ODS RAF steel – Role of irreversible hydrogen trap sites," *Int. J. Hydrogen Energy*, vol. 35, no. 18, pp. 9746–9754, Sep. 2010.

[109] W. C. Luu and J. K. Wu, "The influence of microstructure on hydrogen transport in carbon steels," *Corros. Sci.*, vol. 38, no. 2, pp. 239–245, Feb. 1996.

[110] M. Koyama, E. Akiyama, K. Tsuzaki, and D. Raabe, "Hydrogen-assisted failure in a twinning-induced plasticity steel studied under in situ hydrogen charging by electron channeling contrast imaging," *Acta Mater.*, vol. 61, no. 12, pp. 4607–4618, Jul. 2013.

[111] M. Koyama, C. C. Tasan, E. Akiyama, K. Tsuzaki, and D. Raabe, "Hydrogen-assisted decohesion and localized plasticity in dual-phase steel," *Acta Mater.*, vol. 70, pp. 174–187, May 2014.

[112] M. A. Arafin and J. A. Szpunar, "A new understanding of intergranular stress corrosion cracking resistance of pipeline steel through grain boundary character and crystallographic texture studies," *Corros. Sci.*, vol. 51, no. 1, pp. 119–128, Jan. 2009.

[113] J. W. Morris, C. Kinney, K. Pytlewski, and Y. Adachi, "Microstructure and cleavage in lath martensitic steels," *Sci. Technol. Adv. Mater.*, vol. 14, no. 1, p. 014208, Feb. 2013.

[114] B. A. Szost, R. H. Vegter, and P. E. J. Rivera-Díaz-del-Castillo, "Developing bearing steels combining hydrogen resistance and improved hardness," *Mater. Des.*, vol. 43, pp. 499–506, Jan. 2013.

[115] G. Wang, Y. Yan, J. Li, J. Huang, L. Qiao, and A. Volinsky, "Microstructure effect on hydrogen-induced cracking in TM210 maraging steel," *Mater. Sci. Eng. A*, vol. 586, pp. 142–148, Dec. 2013.

[116] S. L. I. Chan, H. L. Lee, and J. R. Yang, "Effect of Retained Austenite on the Hydrogen Content and Effective Diffusivity of Martensitic Structure," *Metall. Trans. A*, vol. 22A, pp. 2579–2586, 1991.

[117] E. Owczarek and T. Zakroczymski, "Hydrogen transport in a duplex stainless steel," *Acta Mater.*, vol. 48, no. 12, pp. 3059–3070, Jul. 2000.

[118] M. D. Hager, P. Greil, C. Leyens, S. Van der Zwaag, and U. S. Schubert, "Self-healing materials.," *Adv. Mater.*, vol. 22, no. 47, pp. 5424–30, Dec. 2010.

[119] B. Aïssa, D. Therriault, E. Haddad, and W. Jamroz, "Self-Healing Materials Systems: Overview of Major Approaches and Recent Developed Technologies," *Adv. Mater. Sci. Eng.*, vol. 2012, pp. 1–17, 2012.

[120] N. K. Guimard, K. K. Oehlenschlaeger, J. Zhou, S. Hilf, F. G. Schmidt, and C. Barner-Kowollik, "Current Trends in the Field of Self-Healing Materials," *Macromol. Chem. Phys.*, vol. 213, no. 2, pp. 131–143, Jan. 2012.

[121] M. Mitomo, T. Nishimura, and M. Tsutsumi, "Crack healing in silicon nitride and alumina ceramics," *J. Mater. Sci. Lett.*, vol. 15, no. 22, pp. 1976–1978, 1996.

[122] W. Ramm and M. Biscoping, "Autogenous healing and reinforcement corrosion of water-penetrated separation cracks in reinforced concrete," *Nucl. Eng. Des.*, vol. 179, no. 2, pp. 191–200, Feb. 1998.

[123] K. Ando, M.-C. Chu, K. Tsuji, T. Hirasawa, Y. Kobayashi, and S. Sato, "Crack healing behaviour and high-temperature strength of mullite/SiC composite ceramics," *J. Eur. Ceram. Soc.*, vol. 22, no. 8, pp. 1313–1319, Aug. 2002.

[124]N. Travitzky, H. Windsheimer, T. Fey, and P. Greil, "Preceramic Paper-Derived Ceramics," *J. Am. Ceram. Soc.*, vol. 91, no. 11, pp. 3477–3492, Nov. 2008.

[125] A. G. Evans and A. H. Heuer, "Review-transforamtion toughening in ceramics: Martensitic Transformations in Crack-Tip Stress Fields," *J. Am. Ceram. Soc.*, vol. 63, no. 5, pp. 241–248, 1980.

[126] D. Kowalski, M. Ueda, and T. Ohtsuka, "Self-healing ion-permselective conducting polymer coating," *J. Mater. Chem.*, vol. 20, no. 36, p. 7630, 2010.

[127] K. Aramaki and T. Shimura, "Corrosion prevention of passivated iron in 0.1M NaCl by coverage with an ultrathin polymer coating and healing treatment in 0.1M NaNO3," *Corros. Sci.*, vol. 52, no. 4, pp. 1464–1471, Apr. 2010.

[128] G. Q. Xu and M. J. Demkowicz, "Healing of Nanocracks by Disclinations," *Phys. Rev. Lett.*, vol. 111, no. 14, p. 145501, Oct. 2013.

[129] S. M. He, N. H. van Dijk, H. Schut, E. R. Peekstok, and S. van der Zwaag, "Thermally activated precipitation at deformation-induced defects in Fe-Cu and Fe-Cu-B-N alloys studied by positron annihilation spectroscopy," *Phys. Rev. B*, vol. 81, no. 9, p. 094103, Mar. 2010.

[130] G. M. Song, Y. T. Pei, W. G. Sloof, S. B. Li, J. T. M. De Hosson, and S. Van der Zwaag, "Oxidation-induced crack healing in Ti3AlC2 ceramics," *Scr. Mater.*, vol. 58, no. 1, pp. 13–16, Jan. 2008.

[131] S. Hautakangas, H. Schut, S. Van der Zwaag, and N. H. Van Dijk, "The role of the aging temperature on the self healing kinetics in an underaged AA2024 aluminium alloy," *Proc. first Int. Conf. self Heal. Mater.*, no. April, pp. 1–7, 2007.

[132] A. Belyakov, Y. Kimura, and K. Tsuzaki, "Recovery and recrystallization in ferritic stainless steel after large strain deformation," *Mater. Sci. Eng. A*, vol. 403, no. 1–2, pp. 249–259, Aug. 2005.

[133] I. Samajdar, B. Verlinden, P. Van Houtte, and D. Vanderschueren, "Recrystallisation

kinetics in IF-steel: A study on the sluggish recrystallisation behaviour," *Scr. Mater.*, vol. 37, no. 6, pp. 869–874, Sep. 1997.

[134] M. Oyarzábal, A. Martínez-de-Guerenu, and I. Gutiérrez, "Effect of stored energy and recovery on the overall recrystallization kinetics of a cold rolled low carbon steel," *Mater. Sci. Eng. A*, vol. 485, no. 1–2, pp. 200–209, Jun. 2008.

[135] N. Peranio, F. Roters, and D. Raabe, "Microstructure evolution during recrystallization in dual-phase steels," *Mater. Sci. Forum*, vol. 715–716, pp. 13–22, 2012.

[136] R. L. Brown, H. J. Rack, and M. Cohen, "Stress relaxation during the tempering of hardened steel," *Mater. Sci. Eng.*, vol. 21, pp. 25–34, Jan. 1975.

[137] T. Ohmura and K. Tsuzaki, "Evaluation of matrix strength of Fe-C as-quenched and quench-tempered martensite using nanoindentation techniques," *J. Phys. IV Fr.*, vol. 112, pp. 267–270, 2003.

[138] H. Leitner, M. Schober, R. Schnitzer, and S. Zinner, "Strengthening behavior of Fe–Cr–Ni–Al–(Ti) maraging steels," *Mater. Sci. Eng. A*, vol. 528, no. 15, pp. 5264–5270, Jun. 2011.

[139] M. Schober, R. Schnitzer, and H. Leitner, "Precipitation evolution in a Ti-free and Ti-containing stainless maraging steel.," *Ultramicroscopy*, vol. 109, no. 5, pp. 553–62, Apr. 2009.

[140] E. A. Wilson, "Quantification of early stages of age hardening in Fe-12Ni-6Mn maragingtype alloy," *Mater. Sci. Technol.*, vol. 14, pp. 277–282, 1998.

[141] Y. I. He, K. E. Yang, W. E. I. Sha, Z. Guo, K. A. I. Liu, and I. I. E. Procedure, "Age Hardening and Mechanical Properties of a 2400 MPa Grade Cobalt-Free Maraging Steel," *Metall. Mater. Trans. A*, vol. 37A, p. 1107, 2006.

[142] M. Moallemi, A. Najafizadeh, A. Kermanpur, and A. Rezaee, "Effect of reversion annealing on the formation of nano/ultrafine grained structure in 201 austenitic stainless steel," *Mater. Sci. Eng. A*, vol. 530, pp. 378–381, Dec. 2011.

[143] S.-J. Lee, Y.-M. Park, and Y.-K. Lee, "Reverse transformation mechanism of martensite to austenite in a metastable austenitic alloy," *Mater. Sci. Eng. A*, vol. 515, no. 1–2, pp. 32–37, Jul. 2009.

[144] R. D. K. Misra, S. Nayak, S. A. Mali, J. S. Shah, M. C. Somani, and L. P. Karjalainen, "Microstructure and Deformation Behavior of Phase-Reversion-Induced Nanograined/Ultrafine-Grained Austenitic Stainless Steel," *Metall. Mater. Trans. A*, vol. 40, no. 10, pp. 2498–2509, Aug. 2009.

[145] R. D. K. Misra, S. Nayak, P. K. C. Venkatasurya, V. Ramuni, M. C. Somani, and L. P. Karjalainen, "Nanograined/ultrafine-grained structure and tensile deformation behavior of shear phase reversion-induced 301 austenitic stainless steel," *Metall. Mater. Trans. A*, vol. 41, no. 8, pp. 2162–2174, May 2010.

[146] R. D. K. Misra, V. S. A. Challa, P. K. C. Venkatsurya, Y. F. Shen, M. C. Somani, and L. P. Karjalainen, "Interplay between grain structure, deformation mechanisms and austenite stability in phase-reversion-induced nanograined/ultrafine-grained austenitic ferrous alloy," *Acta Mater.*, vol. 84, pp. 339–348, Feb. 2015.

[147] J. Han and Y.-K. Lee, "The effects of the heating rate on the reverse transformation

mechanism and the phase stability of reverted austenite in medium Mn steels," *Acta Mater.*, vol. 67, pp. 354–361, Apr. 2014.

[148] J. Chiang, B. Lawrence, J. D. Boyd, and A. K. Pilkey, "Effect of microstructure on retained austenite stability and work hardening of TRIP steels," *Mater. Sci. Eng. A*, vol. 528, no. 13–14, pp. 4516–4521, May 2011.

[149] N. A. Raji and O. O. Oluwole, "Recrystallization Kinetics and Microstructure Evolution of Annealed Cold-Drawn Low-Carbon Steel," *J. Cryst. Process Technol.*, vol. 3, pp. 163–169, 2013.

[150] N. Peranio, Y. J. Li, F. Roters, and D. Raabe, "Microstructure and texture evolution in dual-phase steels: Competition between recovery, recrystallization, and phase transformation," *Mater. Sci. Eng. A*, vol. 527, no. 16–17, pp. 4161–4168, Jun. 2010.

[151] R. D. K. Misra, S. Nayak, S. A. Mali, J. S. Shah, M. C. Somani, and L. P. Karjalainen, "On the significance of nature of strain-induced martensite on phase-reversion-Induced nanograined/ultrafine-grained austenitic stainless steel," *Metall. Mater. Trans. A*, vol. 41, no. 1, pp. 3–12, Oct. 2009.

[152] I. Gutierrez-Urrutia and D. Raabe, "Dislocation density measurement by electron channeling contrast imaging in a scanning electron microscope," *Scr. Mater.*, vol. 66, no. 6, pp. 343–346, Mar. 2012.

[153] K. Sugimoto and M. Masahiro, "Second phase morphology on retained austenite morphollogy and tensile properties in a TRIP-aided dual-phase steel Sheet," *ISIJ Int.*, vol. 33, no. 7, pp. 775–782, 1993.

[154] X. C. Xiong, B. Chen, M. X. Huang, J. F. Wang, and L. Wang, "The effect of morphology on the stability of retained austenite in a quenched and partitioned steel," *Scr. Mater.*, vol. 68, no. 5, pp. 321–324, Mar. 2013.

[155] J. Shi, X. Sun, M. Wang, W. Hui, H. Dong, and W. Cao, "Enhanced work-hardening behavior and mechanical properties in ultrafine-grained steels with large-fractioned metastable austenite," *Scr. Mater.*, vol. 63, no. 8, pp. 815–818, Oct. 2010.

[156] B. V. N. Rao and M. S. Rashid, "Direct observations of deformation-induced retained austenite transformation in a vanadium-containing dual-phase steel," *Metallography*, vol. 16, pp. 19–37, 1983.

[157] X. D. Wang, B. X. Huang, Y. H. Rong, and L. Wang, "Microstructures and stability of retained austenite in TRIP steels," *Mater. Sci. Eng. A*, vol. 438–440, pp. 300–305, Nov. 2006.

[158] J. H. Ryu, D.-I. Kim, H. S. Kim, H. K. D. H. Bhadeshia, and D.-W. Suh, "Strain partitioning and mechanical stability of retained austenite," *Scr. Mater.*, vol. 63, no. 3, pp. 297–299, Aug. 2010.

[159] K. K. Park, S. T. Oh, S. M. Baeck, D. I. Kim, J. H. Han, H. N. Han, S. Park, C. G. Lee, S. Kim, and K. H. Oh, "In-situ deformation behavior of Retained Austenite on TRIP steel," *Mater. Sci. Forum*, vol. 408–412, pp. 571–576, 2002.

[160] H. Y. Yu, G. Y. Kai, and M. De Jian, "Transformation behavior of retained austenite under different deformation modes for low alloyed TRIP-assisted steels," *Mater. Sci. Eng. A*, vol. 441, no. 1–2, pp. 331–335, Dec. 2006.

[161] Y. Xu, S. H. Zhang, M. Cheng, and H. W. Song, "In situ X-ray diffraction study of

martensitic transformation in austenitic stainless steel during cyclic tensile loading and unloading," *Scr. Mater.*, vol. 67, no. 9, pp. 771–774, Nov. 2012.

[162] P. Wang, N. Xiao, S. Lu, D. Li, and Y. Li, "Investigation of the mechanical stability of reversed austenite in 13%Cr–4%Ni martensitic stainless steel during the uniaxial tensile test," *Mater. Sci. Eng. A*, vol. 586, pp. 292–300, Dec. 2013.

[163] E. Jimenez-Melero, N. H. van Dijk, L. Zhao, J. Sietsma, J. P. Wright, and S. Van der Zwaag, "In situ synchrotron study on the interplay between martensite formation, texture evolution and load partitioning in low-alloyed TRIP steels," *Mater. Sci. Eng. A*, vol. 528, no. 21, pp. 6407–6416, Aug. 2011.

[164] S. Turteltaub and A. S. J. Suiker, "Grain size effects in multiphase steels assisted by transformation-induced plasticity," *Int. J. Solids Struct.*, vol. 43, no. 24, pp. 7322–7336, Nov. 2006.

[165] E. Jimenez-Melero, N. H. van Dijk, L. Zhao, J. Sietsma, S. E. Offerman, J. P. Wright, and S. Van der Zwaag, "Characterization of individual retained austenite grains and their stability in low-alloyed TRIP steels," *Acta Mater.*, vol. 55, no. 20, pp. 6713–6723, Dec. 2007.

[166] Y. Matsuoka, T. Iwasaki, N. Nakada, T. Tsuchiyama, and S. Takaki, "Effect of Grain Size on Thermal and Mechanical Stability of Austenite in Metastable Austenitic Stainless Steel," *ISIJ Int.*, vol. 53, no. 7, pp. 1224–1230, 2013.

[167] A. García-Junceda, C. Capdevila, F. G. Caballero, and C. García de Andrés, "Dependence of martensite start temperature on fine austenite grain size," *Scr. Mater.*, vol. 58, no. 2, pp. 134–137, Jan. 2008.

[168] D. Duchateau and M. Guitmann, "An X-Ray microanalysis study of the partition of manganese in 6 and 9% Mn cryogenic steels and its influence on the stability of austenite dispersed in a tempered martensitic matrix," *Acta Metall.*, vol. 29, pp. 1291–1297, 1981.

[169] S.-J. Lee and K.-S. Park, "Prediction of martensite start temperature in alloy steels with different grain sizes," *Metall. Mater. Trans. A*, vol. 44, no. 8, pp. 3423–3427, May 2013.

[170] S. Zhang and K. O. Findley, "Quantitative assessment of the effects of microstructure on the stability of retained austenite in TRIP steels," *Acta Mater.*, vol. 61, no. 6, pp. 1895–1903, Apr. 2013.

[171] S. Morito, H. Tanaka, R. Konishi, T. Furuhara, and T. Maki, "The morphology and crystallography of lath martensite in Fe-C alloys," *Acta Mater.*, vol. 51, no. 6, pp. 1789–1799, Apr. 2003.

[172] S. Zaefferer, S. I. Wright, and D. Raabe, "Three-dimensional orientation microscopy in a focused ion beam–scanning electron microscope: a new dimension of microstructure characterization," *Metall. Mater. Trans. A*, vol. 39, no. 2, pp. 374–389, Jan. 2008.

[173] M. Calcagnotto, D. Ponge, E. Demir, and D. Raabe, "Orientation gradients and geometrically necessary dislocations in ultrafine grained dual-phase steels studied by 2D and 3D EBSD," *Mater. Sci. Eng. A*, vol. 527, no. 10–11, pp. 2738–2746, Apr. 2010.

[174] D. R. Steinmetz, T. Jäpel, B. Wietbrock, P. Eisenlohr, I. Gutierrez-Urrutia, A. Saeed–Akbari, T. Hickel, F. Roters, and D. Raabe, "Revealing the strain-hardening behavior of twinning-induced plasticity steels: Theory, simulations, experiments," *Acta Mater.*, vol. 61, no. 2, pp. 494–510, Jan. 2013.

[175] I. Gutierrez-Urrutia and D. Raabe, "Dislocation and twin substructure evolution during strain hardening of an Fe–22wt.% Mn–0.6wt.% C TWIP steel observed by electron channeling contrast imaging," *Acta Mater.*, vol. 59, no. 16, pp. 6449–6462, Sep. 2011.

[176] I. Gutierrez-Urrutia and D. Raabe, "Multistage strain hardening through dislocation substructure and twinning in a high strength and ductile weight-reduced Fe–Mn–Al–C steel," *Acta Mater.*, vol. 60, no. 16, pp. 5791–5802, Sep. 2012.

[177] M. A. Jaswon, "Mechanism of Phase Transformations in Metals," *Nature*, vol. 177. pp. 419–421, 1956.

[178] G. B. Olson and M. Cohen, "A general mechanism of martensitic nucleation: Part II. FCC-BCC and other martensitic transformations," *Metall. Trans. A*, vol. 7A, pp. 1905–1914, 1976.

[179] R. Ueji, N. Tsuchida, D. Terada, N. Tsuji, Y. Tanaka, A. Takemura, and K. Kunishige, "Tensile properties and twinning behavior of high manganese austenitic steel with fine-grained structure," *Scr. Mater.*, vol. 59, no. 9, pp. 963–966, Nov. 2008.

[180] I. Gutierrez-Urrutia, S. Zaefferer, and D. Raabe, "The effect of grain size and grain orientation on deformation twinning in a Fe–22wt.% Mn–0.6wt.% C TWIP steel," *Mater. Sci. Eng. A*, vol. 527, no. 15, pp. 3552–3560, Jun. 2010.

[181] S. Mahajan and G. Chin, "Formation of deformation twins in fcc crystals," *Acta Metall.*, vol. 21, p. 1353, 1973.

[182] W. C. Leslie and R. L. Miller, "The stabilization of austenite by closely spaced boundaries," *ASM Trans. Q.*, vol. 57, no. 4, pp. 972–979, 1964.

[183] N. Nakada, H. Ito, Y. Matsuoka, T. Tsuchiyama, and S. Takaki, "Deformation-induced martensitic transformation behavior in cold-rolled and cold-drawn type 316 stainless steels," *Acta Mater.*, vol. 58, no. 3, pp. 895–903, Feb. 2010.

[184] T. Masumura, N. Nakada, T. Tsuchiyama, S. Takaki, T. Koyano, and K. Adachi, "The difference in thermal and mechanical stabilities of austenite between carbon- and nitrogen-added metastable austenitic stainless steels," *Acta Mater.*, vol. 84, pp. 330–338, Feb. 2015.

[185] G. Frommeyer, U. Brüx, and P. Neumann, "Supra-ductile and high-strength manganese-TRIP/TWIP steels for high energy absorption purposes," *ISIJ Int.*, vol. 43, no. 3, pp. 438–446, 2003.

[186] T.-H. Lee, E. Shin, C.-S. Oh, H.-Y. Ha, and S.-J. Kim, "Correlation between stacking fault energy and deformation microstructure in high-interstitial-alloyed austenitic steels," *Acta Mater.*, vol. 58, no. 8, pp. 3173–3186, May 2010.

[187] K. H. Kwon, B.-C. Suh, S.-I. Baik, Y.-W. Kim, J.-K. Choi, and N. J. Kim, "Deformation behavior of duplex austenite and ε -martensite high-Mn steel," *Sci. Technol. Adv. Mater.*, vol. 14, no. 1, pp. 1–8, Feb. 2013.

[188] D. N. Hanlon, J. Sietsma, and S. Van der Zwaag, "The effect of plastic deformation of austenite on the kinetics of subsequent ferrite formation.," *ISIJ Int.*, vol. 41, no. 9, pp. 1028–1036, 2001.

[189] H. Landheer, S. E. Offerman, R. H. Petrov, and L. A. I. Kestens, "The role of crystal misorientations during solid-state nucleation of ferrite in austenite," *Acta Mater.*, vol. 57, no. 5, pp. 1486–1496, 2009.

[190] J. Sietsma, "Phase transformations in steels," in *Phase Transformations in Steels*, E. Pereloma and D. V. Edmonds, Eds. Woodhead Publishing, 2012, pp. 505–526.

[191] P. J. Clemm and J. C. Fisher, "The influence of grain boundaries on the nucleation of secondary phases," *Acta Metall.*, vol. 3, no. 1, pp. 70–73, 1955.

[192] H. Beladi, I. B. Timokhina, S. Mukherjee, and P. D. Hodgson, "Ultrafine ferrite formation through isothermal static phase transformation," *Acta Mater.*, vol. 59, no. 10, pp. 4186–4196, 2011.

[193] S. Hossein Nedjad, M. N. Ahmadabadi, and T. Furuhara, "The extent and mechanism of nanostructure formation during cold rolling and aging of lath martensite in alloy steel," *Mater. Sci. Eng. A*, vol. 485, no. 1–2, pp. 544–549, Jun. 2008.

[194] K. Ono and T. J. Koppenaal, "The effects of prior deformation and transformations on the microstructure of an iron-nickel alloy," *Metall. Trans.*, vol. 5, no. 3, pp. 739–746, 1974.

[195] R. Ueji, N. Tsuji, Y. Minamino, and Y. Koizumi, "Ultragrain refinement of plain low carbon steel by cold-rolling and annealing of martensite," *Acta Mater.*, vol. 50, no. 16, pp. 4177–4189, 2002.

[196] S. I. Wright, M. M. Nowell, and D. P. Field, "A review of strain analysis using electron backscatter diffraction," *Microsc. Microanal.*, vol. 17, pp. 316–329, 2011.

[197] D. Raabe, D. Ponge, O. Dmitrieva, and B. Sander, "Nanoprecipitate-hardened 1.5GPa steels with unexpected high ductility," *Scr. Mater.*, vol. 60, no. 12, pp. 1141–1144, Jun. 2009.

[198] X. Huang, S. Morito, N. Hansen, and T. Maki, "Ultrafine structure and high strength in cold-rolled martensite," *Metall. Mater. Trans. A Phys. Metall. Mater. Sci.*, vol. 43, no. 10, pp. 3517–3531, 2012.

[199] H. F. Lan, W. J. Liu, and X. H. Liu, "Ultrafine ferrite grains produced by tempering cold-rolled martensite in Low carbon and microalloyed Steels," *ISIJ Int.*, vol. 47, no. 11, pp. 1652–1657, 2007.

[200] F. J. Humphreys, "Recovery after deformation," in *Recrystallization and Related Annealing Phenomena*, Second Edi., F. J. Humphreys and M. Hatherly, Eds. Oxford: Elsevier, 2004, pp. 169–213.

[201] B. C. De Cooman, P. Gibbs, S. Lee, and D. K. Matlock, "Transmission electron microscopy analysis of yielding in ultrafine-grained medium Mn transformation-induced plasticity steel," *Metall. Mater. Trans. A*, vol. 44, no. 6, pp. 2563–2572, Feb. 2013.

[202] P. J. Gibbs, B. C. De Cooman, D. W. Brown, B. Clausen, J. G. Schroth, M. J. Merwin, and D. K. Matlock, "Strain partitioning in ultra-fine grained medium-manganese transformation induced plasticity steel," *Mater. Sci. Eng. A*, vol. 609, pp. 323–333, Jul. 2014.

[203] R. Sun, W. Xu, C. Wang, J. Shi, H. Dong, and W. Cao, "Work hardening behavior of ultrafine grained duplex medium-mn steels processed by ART-annealing," *Steel Res. Int.*, vol. 83, no. 4, pp. 316–321, Apr. 2012.

[204] M. Tokizane, N. Matsumura, K. Tsuzaki, T. Maki, and I. Tamura, "Recrystallization and formation of austenite in Deformed Lath Martensitic Structure of Low Carbon Steels," *Metall. Trans. A*, vol. 13A, pp. 1379–1388, 1982.

[205] M. A. Zaccone and G. Krauss, “Elastic limits and microplastic response in ultrahigh strength carbon steels,” *Metall. Trans. A*, vol. 20, no. 1, pp. 188–191, 1989.

[206] Q. Han, Y. Kang, P. D. Hodgson, and N. Stanford, “Quantitative measurement of strain partitioning and slip systems in a dual-phase steel,” *Scr. Mater.*, vol. 69, no. 1, pp. 13–16, Jul. 2013.

[207] J. Han, S.-J. Lee, J.-G. Jung, and Y.-K. Lee, “The effects of the initial martensite microstructure on the microstructure and tensile properties of intercritically annealed Fe–9Mn–0.05C steel,” *Acta Mater.*, vol. 78, pp. 369–377, Oct. 2014.

[208] J. Luster and M. A. Morris, “Compatibility of deformation in two-phase Ti-Al alloys: Dependence on microstructure and orientation relationships,” *Metall. Mater. Trans. A*, vol. 26, no. 7, pp. 1745–1756, 1995.

Acknowledgements

I want to sincerely thank Prof. Dr. Dierk Raabe for giving me the opportunity to do my PhD thesis and carry out research in the Max-Planck-Institut für Eisenforschung GmbH. He provides me with this very interesting research topic and keeps inspiring me with new ideas. I profoundly benefit from every single fruitful discussion and his rich knowledge in material science.

I also want to gratefully thank Prof. Dr. Wolfgang Bleck for agreeing with co-supervising my PhD thesis. He inspired me to pursue research in the field of material science when I was a master student. He gives me quite valuable advice and suggestions during the process of my PhD thesis.

I want to thank Dr. Cem Tasan and Dr. Dirk Ponge for their encouragement, their patience, their guidance and support. The fruitful and inspiring daily discussions are valuable treasure during the process of my PhD thesis.

I also want to express my appreciation to Dr. Aleksander Kostka for his great support in TEM experiments and valuable discussions during data analysis.

My great thanks also go to all technicians for their great support and help. I want to especially thank Mr. Michael Adamek and Mr. Herbert Faul for performing mechanical tests, Ms. Monika Nellessen, Ms. Katja Angenendt and Ms. Heidi Bögershausen for their great help with sample preparations and microstructure characterizations, Mr. Benjamin Breitbach for carrying out XRD measurements and help with data analysis, and Mr. Ralf Selbach from workshop for machining samples for all tests.

I also want to sincerely thank all colleagues from Max-Planck-Institut für Eisenforschung GmbH for creating this family-like working atmosphere and their daily help. I want to especially thank my group members in group ‘adaptive structural materials’ for their great help and fruitful discussions during group meetings.

I also want to grateful thank my friends and my family for their encouragement and support.

I also want to acknowledge the funding by the Financial support European Research Council under the EU‘s 7th Framework Programme (FP7/2007-2013)/ERC Grant agreement 290998 “SmartMet”.

Abstract

Martensite, as one of the most well-known yet least understood microstructures occurring in modern advanced steels, profoundly suffers from its inherent brittleness. The aim is to enhance the ductility and toughness of martensite base materials by designing nanolaminate microstructure consisting of alternating layers of martensite and austenite via segregation engineering. These austenite layers are expected to act as buffer zones in front of cracks, e.g. providing possible crack blunting or reflecting effects. To understand improvements in mechanical properties, it is necessary to systematically investigate the underlying deformation and damage micro-mechanisms within microstructure constituents and their interplay.

For these purposes, in this work, a Fe-9Mn-3Ni-1.4Al-0.01C (mass %) medium-Mn martensitic steel was designed. Segregation engineering with support from thermodynamic and kinetic simulations (using Thermo-Calc and Dictra software with TCFE7 and MOBFE2 databases) were used to create nanolaminate microstructure consisting of alternating martensite and reverted austenite layers. Microstructure and micro-mechanical characterizations were conducted by *in-situ*/*post-mortem* tension and bending experiments in conjunction with high-resolution scanning electron microscopy (SEM) based electron backscatter diffraction (EBSD) mapping, electron channeling contrast imaging (ECCI), secondary electron imaging (SE) and energy dispersive X-ray spectroscopy (EDX), as well as *post-mortem* transmission electron microscopy (TEM), X-ray diffraction analysis (XRD) and synchrotron X-ray diffraction (SXRD) analysis.

The results reveal that with the guidance of Thermo-Calc and Dictra calculations, segregation engineering successfully decorates all lath martensite boundaries with nano-films of reverted austenite, thus being able to create the nanolaminate microstructure. Enhanced strain hardening capacity and damage resistance are achieved in the nanolaminate martensite-reverted austenite microstructure, which are attributed to (i) dynamical strain partitioning between martensite and reverted austenite governed by a highly dynamical interplay of dislocation slip, deformation-induced phase transformation (causing the TRIP effect) and mechanical twinning (i.e. causing the twinning-induced plasticity effect) and (ii) the nanolaminate microstructure morphology, leading to enhanced ductility. Meanwhile, within the reverted austenite phase, an unexpected ‘smaller is less stable’ effect is observed. This unexpected transformation size effect is due to the size-dependent competition between mechanical twinning and deformation-induced phase transformation.

In addition, a promising strategy is also proposed to utilize austenite reversion for designing martensitic steel with high resistance against hydrogen embrittlement.

Zusammenfassung

Als sehr bekannter aber am wenigsten verstandenes Gefügebestandteil vieler moderner Hochleistungsstähle leidet Martensit an seiner inhärenten Sprödigkeit. Das Ziel dieser Arbeit ist die Steigerung der Duktilität und Zähigkeit von martensitischen Materialien durch Erzeugung einer nanolaminierten Mikrostruktur aus abwechselnden Schichten aus Martensit und Austenit unter Ausnutzung von Seigerungseffekten. Es wird erwartet, dass diese Austenitschichten Risse auffangen können, indem sie z.b. Rissspitzen abstumpfen oder Risse ablenken. Um Verbesserungen der mechanisch/technologischen Eigenschaften verstehen zu können, ist es notwendig, die für Verformung und Schädigung relevanten Mikromechanismen in den verschiedenen Gefügebestandteilen und deren Wechselwirkungen systematisch zu untersuchen.

Für diese Aufgabe wurde in dieser Arbeit ein Fe-9Mn-3Ni-1.4Al-0.01C (Massen %) martensitischer Mittelmanganstahl konzipiert. Durch Unterstützung durch thermodynamische und kinetische Simulationen (Programme Thermo-Calc und Dictra mit TCFE7 und MOBFE2 Databases) wurden Seigerungen ausgenutzt, um ein nanolaminiertes Gefüge bestehend aus abwechselnden Schichten aus Martensit und Reversionsaustenit zu kreieren. Die mikrostrukturelle und mikromechanische Charakterisierung wurde durchgeführt mittels *in-situ/post-mortem* Zug- und Biegeversuchen in Verbindung mit hochauflösender auf Rasterelektronenmikroskopie basierender Elektronrückstreubeugung (EBSD), electron channeling contrast imaging (ECCI), Sekundärelektronenabbildung (SE) und energiedispersive Röntgenspektroskopie (EDX) als auch *post-mortem* Transmissionselektronemikroskopie (TEM), Röntgendiffraktionsanalyse (XRD) und Synchroton-Röntgendiffraktionsanalyse (SXRD).

Unter Zuhilfenahme von Thermo-Calc und Dictra Berechnungen zeigen die Ergebnisse, dass über Seigerungseffekte schließlich alle Grenzflächen zwischen den Martensitlatten mit nanoskopischen Schichten aus Reversionsaustenit belegt werden können und somit die Erzeugung einer nanolaminierten Mikrostruktur ermöglicht wird. Durch diese nanolaminierte Mikrostruktur aus Martensit und Reversionsaustenit wird bei plastischer Verformung die Verfestigungsrate und der Widerstand gegen Schädigung gesteigert. Dies wird zurückgeführt auf (i) eine dynamische Dehnungsumverteilung zwischen Martensit und Reversionsaustenit, bedingt durch die ausgeprägten dynamischen Wechselwirkungen zwischen Versetzungsgleitung, verformungsinduzierte Phasenumwandlung, die zu einem TRIP Effekt führt und mechanische Zwillingsbildung und (ii) auf die nanolaminierte Gefügemorphologie. Dies führt zu einer verbesserten Duktilität. Unterdessen wurde im Reversionsaustenit ein unerwarteter ‘kleiner ist weniger stabil’ Effekt beobachtet. Dieser unerwartete Umwandlungsgrößeneffekt tritt aufgrund der größenabhängigen Konkurrenz zwischen mechanischer Zwillingsbildung und verformungsinduzierter Phasenumwandlung auf.

Zusätzlich wird eine aussichtsreiche Strategie vorgeschlagen, um die Austenitreversion auszunutzen für das Design von martensitischen Stählen mit verbesserter Beständigkeit gegenüber Wasserstoffversprödung.